OSCILLATIONS OF THE INTERTROPICAL CONVERGENCE ZONE AND THE GENESIS OF EASTERLY WAVES

A Thesis
Presented to
The Academic Faculty

by

Violeta E. Toma

In Partial Fulfillment
of the Requirements for the Degree
Doctor of Philosophy in the
School of Earth and Atmospheric Sciences

Georgia Institute of Technology
August 2008

OSCILLATIONS OF THE INTERTROPICAL CONVERGENCE ZONE AND THE GENESIS OF EASTERLY WAVES

Approved by:

Dr. Peter J. Webster, Advisor
School of Earth and Atmospheric Sciences
Georgia Institute of Technology

Dr. Yi Deng
School of Earth and Atmospheric Sciences
Georgia Institute of Technology

Dr. Robert X. Black
School of Earth and Atmospheric Sciences
Georgia Institute of Technology

Dr. John A. Knox
Faculty of Engineering
University of Georgia

Dr. Judith A. Curry
School of Earth and Atmospheric Sciences
Georgia Institute of Technology

Date Approved: 06/26/2008

To my husband, Ion, my love and my best friend

ACKNOWLEDGEMENTS

I would like to express my appreciation to my advisor Dr. Peter J. Webster for his support and understanding throughout the years. I am grateful to him for his guidance in showing me the path to becoming a better scientist. I would also like to thank my thesis committee members for all their help and suggestions on my research. My group members (past and present) have made the final product of my research richer, with their ideas and comments. Special thanks to Dr. Hai-Ru Chang for sharing his expertise in handling atmospheric numerical models.

Thanks to my friends Arsineh, Juliana and Kelly for putting a smile on my face, when the trip was uphill.

I thank my family for their unconditional love, care and inspiration. I am enormously grateful to my husband, Ion, without whose love, encouragement and patience, I would not have been able to start nor finish this journey. I would like to thank him for believing in me, even when I doubted myself. And finally, thanks to my son David, for bringing brightness and laughter to my life.

TABLE OF CONTENTS

LIST OF TABLES

LIST OF FIGURES

SUMMARY

We examine the eastern Pacific Ocean Intertropical Convergence Zone (ITCZ) both in its mean state and transient phases using a combined diagnostic, theoretical and numerical modeling approach. The eastern Pacific mean ITCZ possesses maximum convection in the vicinity of 8º N-10º N and exists in a strong cross-equatorial pressure gradient (CEPG) regime. Also, the latitude of maximum convection is found to be well equatorward of the maximum SST or the minimum mean sea-level pressure (MSLP). Further to the west near the date-line, where the CEPG is less, the convection is weaker and more aligned with the location of maximum sea-surface temperature (SST). It is argued that in regions of significant CEPG the system is inertially unstable. Using simple arguments based on absolute vorticity, we develop an expression for the mean latitude of the ITCZ in terms of the CEPG.

We note that the ITCZ is perpetually in a transient state with strong variability occurring on 4-8 day time scales. Transients, about half the amplitude of the mean ITCZ, propagate northwards from the near-equatorial southern hemisphere eventually increasing the convection in the vicinity of the mean ITCZ convection. It is argued that the mean ITCZ is continually inertially unstable with incursions of anticylonic vorticity advected across the equator resulting in the creation of a divergence-convergence doublet. The low-level convergence generates convection and vortex tube stretching which generates cyclonic vorticity counteracting the northward advection of anticylonic vorticity. During a cycle, the heating in the mid-troposphere near 10ºN oscillated between 6 and 12 K/day at the inertial frequency of the latitude of the mean convection. The shallow meridional

circulation, noted in the mean field in other studies, appears to be a result of the transient nature of the ITCZ.

It is hypothesized that westward propagating equatorial waves result from the inertial oscillation of the ITCZ. To test that the waves are formed *in situ* in the eastern Pacific and not remnants of waves propagating from the Atlantic or promoted by the Central and South American orography, several numerical experiments are undertaken using a high-resolution regional model spanning the western Atlantic Ocean and the eastern Pacific. In the control case, the model is initialized at all boundaries with full high-frequency observations. In two additional experiments, these transients are filtered out, and a third experiment is run with the topography over a large part of Central and South America removed. In all experiments, westward propagating waves are formed in the region of high CEPG suggesting that the hypothesis of *in situ* development may be correct.

CHAPTER I

INTRODUCTION

Traditionally, the tropical general circulation is thought to consist of a thermally directed circulation that transports heat away from the equator to higher latitudes locally through convection and latent heat release and then by advection. In the vicinity of the equator, warm tropical air rises and flows toward the poles until it reaches the subtropics where it descends and returns towards the equator in the surface layers as the trade winds. This dominant large scale circulation pattern that covers nearly half of the surface area of the globe is known as Hadley Circulation. The rising branch of the Hadley circulation is characterized by intense rainfall, while the descending branch is responsible for the very dry subtropical oceans and continental areas. These regional manifestations of the Hadley Circulation affect the lives and economies of more than half of the world's population.

The rising branch of the Hadley circulation has become known as the Intertropical Convergence Zone (ITCZ) (Sansom 1965). In a fundamental sense, the climatological ITCZ may be thought of as a band of deep convection and intense rainfall at the confluence region of the northeast and southeast trade wind regimes of the northern and southern hemisphere. Understanding the ITCZ will help researchers improve tropical cyclogenesis forecasts and drought and flood predictions for the regions affected by tropical weather.

In the following sections of this chapter, the general characteristics of the ITCZ are discussed. Previous relevant studies are reviewed to present a complete picture of existing theories on ITCZ mechanism together with their limitations.

1.1 General features

The ITCZ follows a distinct annual cycle located in the summer hemisphere in most tropical locations except for the eastern Pacific and Atlantic oceans where the ITCZ remains in the northern hemisphere except during El Niño periods. Figure 1.1 shows the annual cycle of rainfall in the ITCZ. Monthly average precipitation distributions were calculated using Global Precipitation Climatology Project (GPCP) monthly data (Adler et al. 2003) for the 1981-2000 time period along six different longitudinal sectors. The location of the ITCZ varies with season, reaching furthest south in the boreal winter (DJF) and furthest north in the boreal summer (JJA). The migration over land regions follows the solar cycle, whereas over the ocean regions it lags the solar heating by 1-2 months. In addition, the rainfall pattern displays strong longitudinal variability. The eastern Pacific (except during El Niño periods) and Atlantic ITCZ appear as regions of narrow intense rainfall, located to the north of the equator for most of the year even though the annual-mean solar radiation at the top of the atmosphere is symmetric with respect to the equator and possesses a maximum in the southern hemisphere at the austral solstice. Over the African continent, the precipitation region spans a wider latitude belt and it is closer to the equator compared to the Atlantic and east Pacific convective region, following a distinct annual cycle. Over the central Pacific, the ITCZ shows a unique pattern with precipitation maxima located on both sides of the equator. The southerly maximum is related to the equatorial end of the South Pacific Convergence Zone (e.g., Trenberth 1976, Vincent 1994). The ITCZ in the Indian Ocean region also possesses strong seasonality. During the summer monsoon season there is a peak just south of the equator and a higher peak further north. These two peaks are related to precipitation

during different phases of intraseasonal variability of the monsoon (e.g., Lawrence and Webster 2001, Hoyos and Webster 2007).

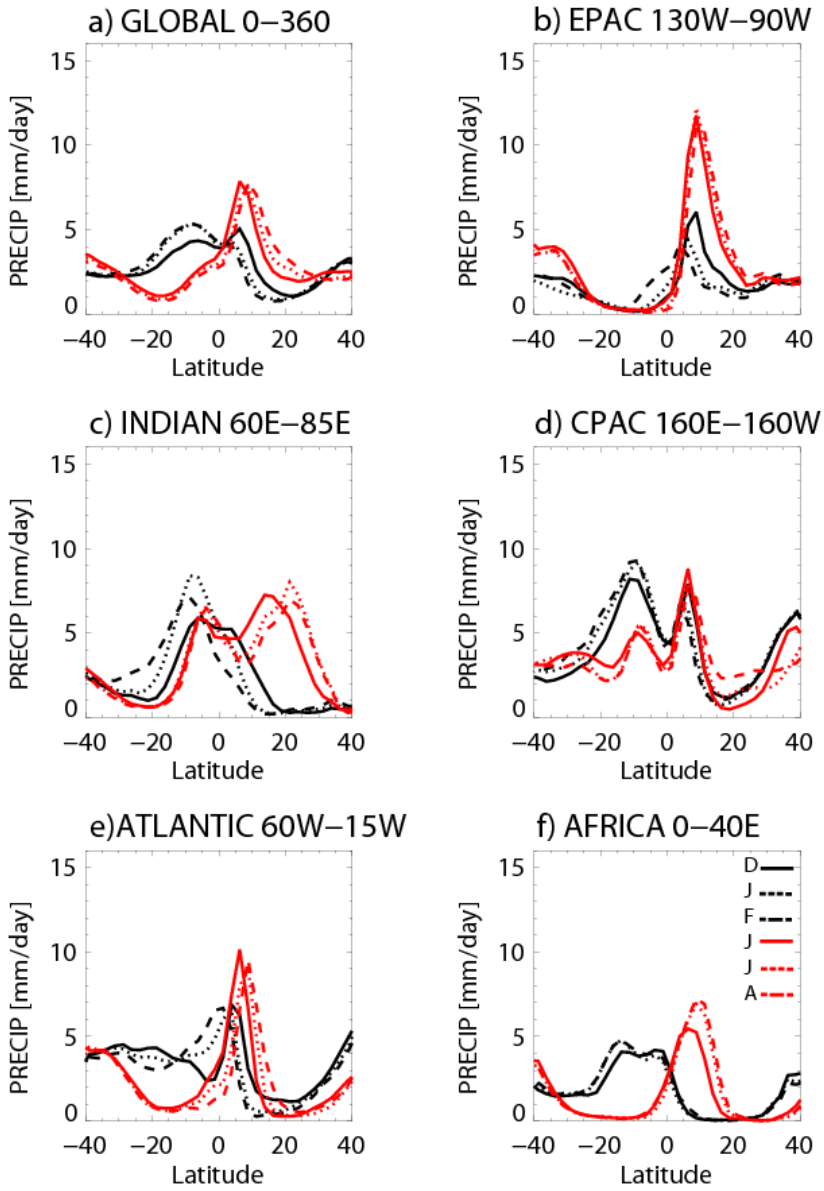

Figure 1.1: Long-term monthly-averaged precipitation rate (units: mm day^{-1}) for three summer months; June, July and August and three winter months; December, January and February) (see legend). Data is zonally averaged for 6 different sectors: (a) global 0-360°, (b) eastern Pacific 130°-90°W, (c) Indian 60°E-85°E, (d) Central Pacific 160°E-160°W, Atlantic 60°W-15°W, Africa 0-40°E. GPCP monthly data for the 1981-2000 time period were used.

The observed off-equatorial precipitation pattern in the eastern tropical Pacific and Atlantic (Figure 1.1b, e) cannot be explained on the basis of simple considerations of sun-earth geometry. A major aim of this study is to determine what processes determine the northward position of ITCZ precipitation.

The ITCZ is an important component of the energy balance of the Earth's climate (e.g., Trenberth and Caron 2001). The global energy balance between incoming solar radiation and outgoing long wave radiation shows a net heating at the equator and a net cooling at higher latitudes. The excess heat absorbed at the tropics is transported to higher altitudes through convection and latent heat release. Transients within the ITCZ play an important part in this vertical transport. Riehl and Malkus (1958, 1979) identify the role of the tropical depression as an important source of vertical heat transport in the tropics. They introduced the concept of the "hot tower mechanism" of undiluted cumulonimbus in the ITCZ. This mechanism was invoked to carry energy from the surface layer through the mid troposphere energy minima into the upper troposphere, where it would be exported laterally to higher latitudes. However there is no observational evidence of "undiluted updraft cores" and the updraft velocities are smaller than those consistent with adiabatic lifting (Zipser 2003). Thus, it would seem that there may have to be other mechanisms of vertical transport rather than the hot tower hypothesis.

From year-to-year, small deviations in the climatological location of the ITCZ produce surpluses or deficits of precipitation in regions such as the West African Sahel (Grist and Nicholson 2001), northeastern Brazil (Biasutti et al. 2003) and other regions throughout the tropics. In all ocean basins, the position and intensity of the ITCZ is

related to the strength and location of the trade wind regime. The trades, in turn, drive poleward oceanic fluxes of heat through Ekman drift, especially in the winter hemisphere where the trade winds are stronger. In the Pacific Ocean, the characteristics of the trade winds are known to be associated with modes of interannual variability and are integral components of the coupled ocean-atmosphere El Nino-Southern Oscillation (ENSO) cycle (Bjerknes 1969). Several studies have found changes in tropospheric moisture and the strength of Hadley circulation in connection to ENSO events (Soden and Fu 1995, Bates et al. 1996, Oort and Yienger 1996). Tropical SST anomalies are connected with remote atmospheric features such as the subtropical jet, the subtropical high over the central Pacific and the Aleutian low (e.g., Arkin 1982, Rasmusson and Carpenter 1982, Pan and Oort 1983)

Thus understanding what determines the structure and position of the ITCZ is essential for understanding the earth climate on the global scale.

1.2 East Pacific ITCZ

Figure 1.1 showed that the ITCZ display great variation along the equator. An exceptional region is the eastern equatorial Pacific Ocean where the ITCZ remains in the northern hemisphere throughout the entire year and is not collocated with the highest SST or the lowest MSLP (e.g., Tomas and Webster 1997; henceforth referred to as TW). Moreover, the eastern Pacific Ocean is a region of intense tropical storms activity. Another reason to focus on eastern Pacific is the large amounts of data available (e.g., Tropical Atmosphere Ocean project (TAO): McPhaden et al. 1998, Tropical Eastern Pacific Process Study (TEPPS): Yuter and Houze 2000, Yuter et al. 2000, East Pacific

Investigation of Climate Processes in the Coupled Ocean-Atmosphere System (EPIC) experiment: Raymond et al. 2004).

1.2.1 General features of East Pacific ITCZ

Figure 1.2a shows the mean distribution of deep convective cloudiness in the tropical Pacific Ocean for June, July and August (JJA). The year chosen for an initial view of the Pacific was 1996, which is fairly typical of non-El Nino years. A similar analysis, but for a much longer period (20 years) will be shown in Chapter 3. Out-going long-wave radiation (OLR) was used as a proxy for deep convection. Henceforth, mean monthly areas of OLR values ≤ 240 Wm^{-2} will be assumed to be convective regions and areas with OLR values > 240 Wm^{-2} as "clear-sky" regions. The deepest convection (lowest values of OLR) is to the east of 120°W, filling a broad region from about 5°N to the Central American and Mexican coasts. The convective maximum extends westward as a narrowing band to merge with a much broader and less intense region of convection to the west of 170°E. In total, this band of convection, extending across the entire tropical Pacific Ocean, is referred to as the ITCZ. But within this broad region of convection there is large longitudinal variability.

Figures 1.2b and c show the mean distributions of SST and MSLP in the tropical Pacific domain. The SST pattern is dominated by the broad western Pacific warm pool that extends across the equator and occupying both hemispheres (e.g., Webster and Lukas 1992). A relative convection maximum (Figure 1.2a) extends roughly along 10°N towards the east and a broader maximum >28°C located north of 12-15°N and east of 120°W.

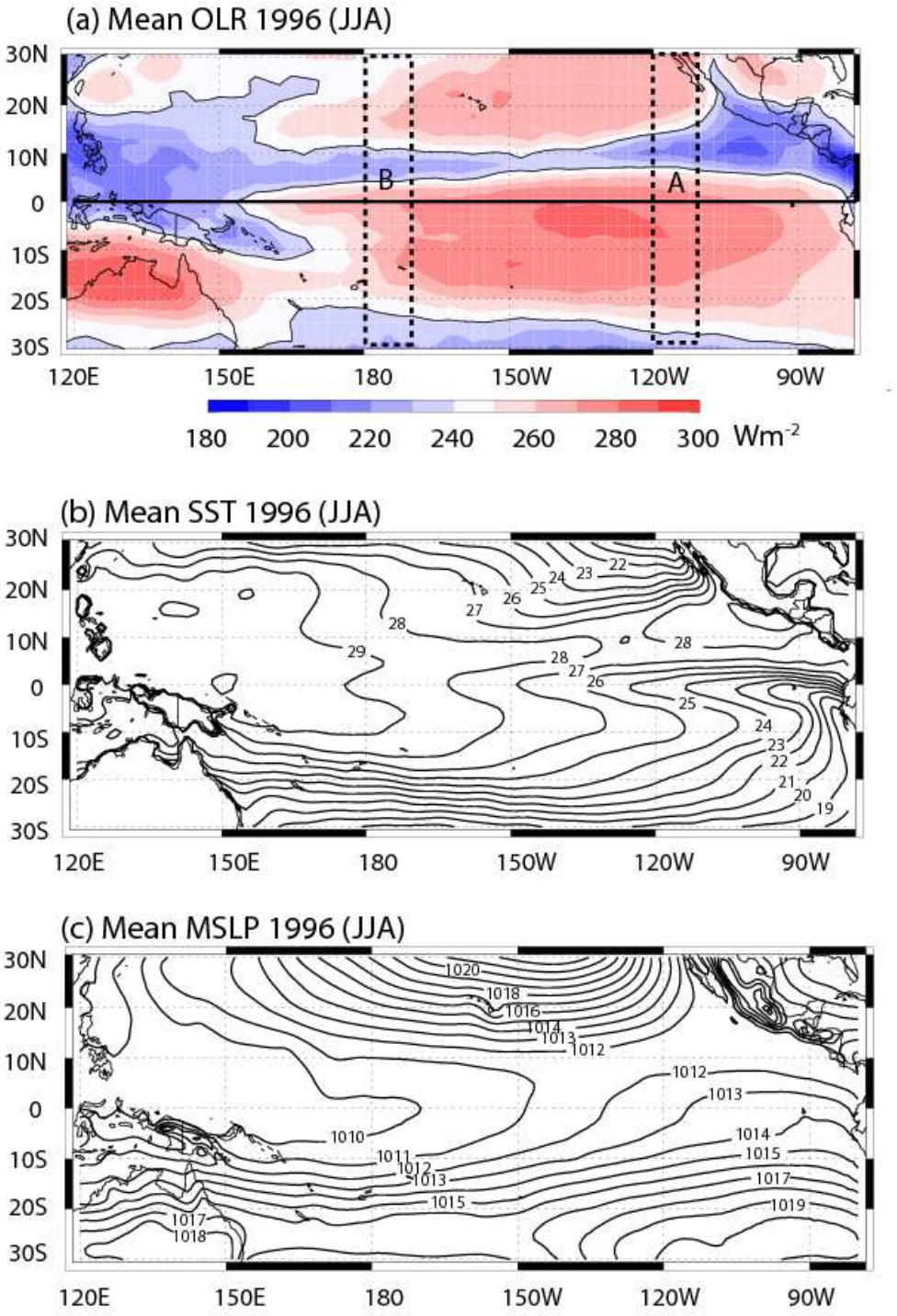

Figure 1.2: (a) Mean distribution of OLR (units Wm^{-2}) over the Pacific Ocean for the period June-August, 1996. The dashed boxes indicate two domains that will be studied in more detail subsequently. (b) Mean sea-surface temperature (SST: °C) distribution across the Pacific Ocean, (c) Mean sea-level pressure (MSLP: hPa), (d) OLR time series (units: Wm^{-2}) at [110W°; 10°N] for 1996.

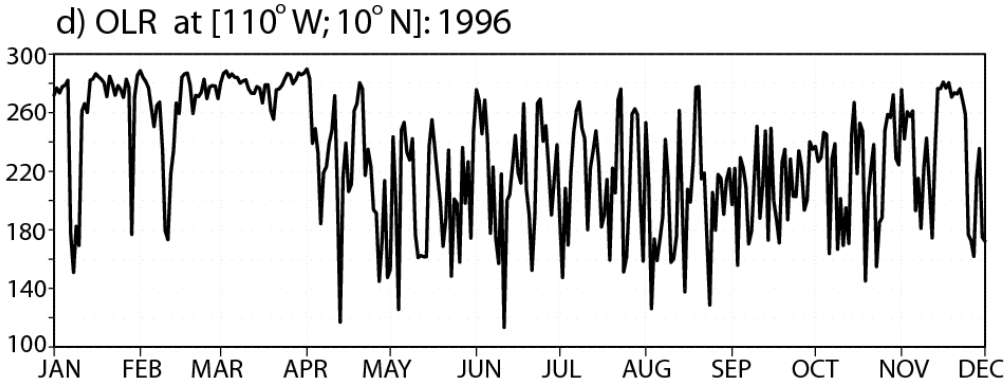

Figure 1.2: (cont)

Overall, different sectors in the equatorial Pacific Ocean are differentiated by the SST patterns, with small cross-equatorial gradient in the west and much larger gradient in the east. To a large degree, the MSLP field matches the SST distribution with high pressure overlying cool SST (e.g., southeastern Pacific Ocean) and low pressure associated with higher SSTs (e.g., the western equatorial and the tropical northeastern Pacific Ocean). Thus, the SST patterns translate into surface cross-equatorial pressure gradients.

Figure 1.2d shows the daily OLR time series at [110W°; 10°N] for 1996. In addition to its longitudinal variability (Fig. 1a), the ITCZ shows considerable temporal variability. First, there is a significant seasonal difference, with values of OLR much lower during the May - November period, compared to the December - April period. On short time scales, on the order of several days, the ITCZ oscillates between convective and relatively clear-sky periods. The majority of these oscillations are associated with the presence of easterly waves. A central question of this study is what is the relationship between the intensity and location of the mean ITCZ and the high-frequency transients? A review of the current knowledge of easterly waves will be provided later in this

chapter, followed by a detailed description of the general features of these waves in section 3.2.2.

Figure 1.2a-c suggests a number of apparent peculiarities regarding the position of the oceanic ITCZ relative to background fields of SST and MSLP. Earlier theories of the ITCZ (e.g., Rowntree 1971, Pike 1971) suggested that maximum convection is associated with maximum SST. However, this proves not necessarily to be the case. Over many regions of the tropical oceans, the ITCZ tends to be located on the equatorward side of the warmest SST and MSLP (e.g., Ramage 1974, Sadler 1975, Hastenrath and Lamb 1977a, b, Lindzen and Nigam 1987, TW). Figure 1.3 shows latitudinal distributions of SST, MSLP, OLR and (for later reference) the 850 hPa absolute vorticity ($\eta = f + \varsigma$, where f is the Coriolis force and ς is the vertical component of relative vorticity) averaged across two longitude bands for the 1981-2000 time period. The first band (the 120°-110°W section A in Figure 1.2a) cuts across the ITCZ in the eastern Pacific. The second band (section B in Figure 1.2b between 180°-170°W) bisects the broadening central Pacific ITCZ. The two sections possess different characteristics. Within the 120°-110°W section, convection (OLR minimum 9°N), on one hand, and SST (maximum 12°N) and MSLP (minimum 13°N) extrema, on the other, are not collocated. In the western section (B), there are very different relationships between the variables. For example, there are two SST maxima: one at 5°N and the other at 6°S and the MSLP minimum resides at 2°S. Maximum convection remains in the northern hemisphere, but it is considerably weaker in the western section, with a mean value of 220 Wm^{-2}, compared to 208 Wm^{-2} in the eastern Pacific.

The magnitude of the cross-equatorial pressure gradient (CEPG) is a differentiating factor between the eastern, central and western equatorial sectors of the Pacific Ocean. Table 1.1 shows the MSLP differences in the zonal bands 20°N-20°S, 10°N-10°S, 15°N-15°S and 5°N-5°S at different longitudes across the Pacific Ocean. In general, in the western-central Pacific Ocean, the MSLP difference is small. However, in the eastern Pacific Ocean the MSLP differential is larger, reaching as high as 7.0 hPa between 20°N and 20°S. For comparison, this pressure difference is a factor of two greater than the difference between the eastern and western Pacific Ocean along the equator. Specifically, the difference between 120°W and 170°E averaged between 5°N and 5°S is 2.9 hPa. In terms of pressure gradient, the CEPG between 5°N and 5°S in the eastern Pacific Ocean is about a factor of four larger than its longitudinal component. Between 20°N and 20°S the gradient difference increases to an order of magnitude. TW noted that the displacement of the zero absolute vorticity contour (η=0) from the equator is directly related to the magnitude of the CEPG. A global analysis found correlations between the latitude of the position of the zero contour and the broad scale 20°N-20°S CEPG of -0.85 and the 10°N-10°S CEPG of -0.91. The importance of these findings to the structure and maintenance of off-equatorial ITCZ convection will be discussed in Chapters 3 and 4.

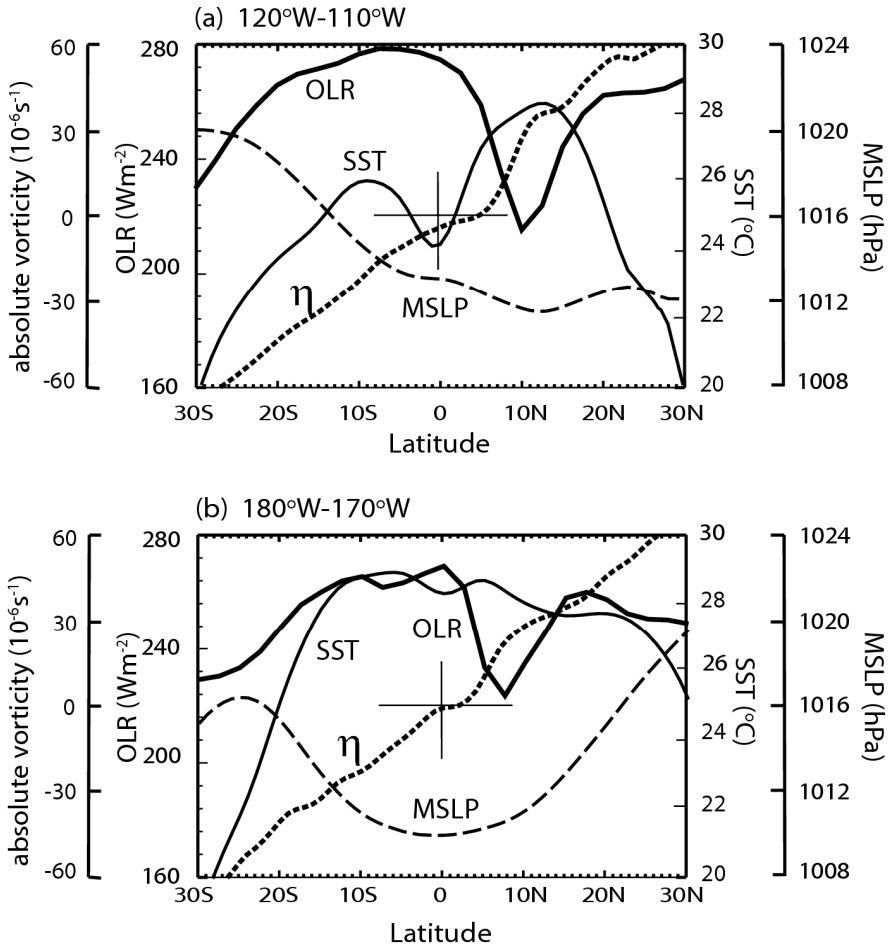

Figure 1.3: Cross-sections of OLR (Wm^{-2}), SST (°C), MSLP (hPa) and absolute vorticity at 850 hPa(10^{-6} s^{-1}) defined in the text for the two longitudinal bands (a) 120°W-110°W and (b) 180°W-170°W, depicted as sections A and B in Figure 1.2a. The cross-hairs show location of the equator and zero absolute vorticity. The data was averaged for the 1981-2000 time period.

Table 1.1: Latitudinal difference in MSLP (hPa) in the equatorial Pacific Ocean.

Band	170°E	180°E	170°W	160°W	150°W	140°W	130°W	120°W	110°W
20N-20S	-1.6	-0.5	+0.2	-0.1	+0.6	-2.0	-4.0	-5.3	-7.0
15N-15S	-1.2	-0.7	-0.9	-0.8	-0.9	-2.1	-3.7	-5.0	-5.7
10N-10S	0	0	-0.1	-0.5	-0.6	-1.3	-2.1	-3.0	-3.4
5N-5S	+0.2	+0.2	-0.1	-0.2	-0.5	-0.7	-0.9	-0.9	-1.1

1.2.2 Physical mechanisms that determine the location of the mean ITCZ

The first attempts to explain the physical nature of the tropical climate came from two scientists, Sir Edmund Halley and Sir George Hadley. They both attempted to explain the observed patterns of the trade winds. Halley (1686) hypothesized that the trade winds are part of a meridional cell driven by rising air in the tropics and subsidence at higher latitudes. A more complete explanation for the orientation of the tropical wind field was given by Hadley (1735). He realized that the Earth rotation plays an important role in providing a westward component in the surface winds and postulated that the return flow aloft would have an eastward component.

Several more recent studies have attempted to explain the mechanisms responsible for the location of the mean ITCZ. They can generally be divided in two main groups. In the first, the location and intensity of the ITCZ is closely related to the SST distribution. Manabe (1969) and Manabe et al. (1974) using numerical models showed that the ITCZ forms in regions where local SST maximum exists. Pike (1971) hypothesized that the equatorial cold tongue is responsible for the displacement of the ITCZ from the equator and for the occasionally observed double ITCZ. In fact, the results of his modeling were that convection and SST maxima were collocated. Xie and Philander (1994) and Philander et al. (1996) proposed a wind-evaporation feedback to explain the off-equatorial position of ITCZ and also as a means of the maintaining the band of high SST. However these hypotheses are not in agreement with previous studies

(e.g., Lindzen and Nigam 1987) and with the observations (i.e. Figure 1.3a), which show that convection is not always associated with maximum SST.

The second group of theories depends on atmospheric internal dynamics emphasizing zonally symmetric processes or propagating disturbances. Charney (1971) argued that the location of the ITCZ is due to a balance between Ekman pumping and moisture availability (as a result of maximum SST). However, in the case of the eastern Pacific Ocean, a comparison between Figure 1.2a and b shows that the warmest waters are not over the region with maximum precipitation. Held and Hou (1980) tried to predict the strength and width of Hadley Circulation using a zonally symmetric model with imposed heating at the equator. Although the Held-Hou model provides a reasonable estimate of poleward extension of the Hadley circulation, it gives a very poor estimate of the strength of the circulation. Lindzen and Hou (1988) extended the Held-Hou model and found that locating a heating source of the same magnitude away from the equator increases the strength of the meridional circulation. Hou and Lindzen (1992) suggested that the magnitude of the circulation increases when the heating is latitudinally concentrated in a narrow band. While the above studies incorporate basic dynamics, they do not include the effect of latent heating (only dry atmosphere being considered) and they do not explain why the heating is centered off the equator. Hack et al. (1989) found that the structure of the meridional circulation is very sensitive to the position and intensity of convection (i.e. diabatic heating). However they did not address the question of what determines the location of the heating. Mitchell and Wallace (1992) argued that ocean – atmospheric feedback mechanisms in the eastern Pacific and Atlantic Ocean influence the strength of the cold tongue, and in turn the ITCZ. Waliser and Somerville

(1994) suggested that convection occurs 4°-12° away from the equator because, at these latitudes, low-level convergence is dynamically maximized so that convergence of moist air is enhanced. They hypothesized that an imposed low-latitude mid-tropospheric heat source (e.g., moist deep convection) induces a CEPG, which is balanced by a combination of friction and geostrophy. Friction induces convergence and, because the atmosphere is conditionally unstable, convection. If the heat source is moved a small distance from the equator, the role played by friction is increased on the equatorial side of the pressure anomaly. A continued displacement of the heat source leads to decreased low-level convergence because the Coriolis force on its equatorial side increases. An optimal location for the ITCZ occurs when these two factors are optimized. Although they used a numerical model that predicted an off-equatorial location of the ITCZ as well, it is not clear if the mechanism in the theoretical model is the same as the one occurring in the numerical experiment.

TW (and later Tomas et al. 1999, hereafter THW) noted the importance of the magnitude of the CEPG in determining the location of the ITCZ. As mentioned earlier, there was a very high negative correlation between the CEPG and location of zero absolute vorticity contour. It was argued that a finite CEPG produces an incursion of either anticyclonic vorticity into the northern hemisphere or cyclonic vorticity into the southern hemisphere. Both of these situations are inertially unstable (e.g., Stevens 1983, TW). THW noted that although the mean cross-equatorial flow and the location of convection appeared to be consistent with inertial instability, the linear stability criterion was not met in regions of strong CEPG. But, as will be discussed in chapter 4, this conclusion resulted from overestimating the atmospheric stability and with more realistic

values, the linear criterion is met. TW noted another interesting feature of the off-equator ITCZ. Rather than one deep meridional circulation occupying the entire troposphere, a secondary weaker circulation restricted to the lower half of the troposphere appears in the mean fields. In a study of the eastern Pacific Ocean, Zhang et al. (2004) described this second cell in detail. We refer to this as the ZMB circulation. Considerable attention will be given to describing this cell in Chapters 3 and 4 as it proves to be indicative of transient processes within the mean ITCZ.

A recent study by Raymond et al. (2006) investigated variability in the eastern Pacific ITCZ using East Pacific Investigation of Climate Processes in the Coupled Ocean-Atmosphere System (EPIC: Raymond et al. 2004) data. They, too, note the importance of the CEPG as an important factor in determining the location of the ITCZ. Using a cross-equatorial Ekman boundary layer model, Raymond et al. (2006) assume an input of free-tropospheric momentum into the boundary layer. Within their theory, it is assumed that enhancement or suppression of convection is caused by alterations of the CEPG by external factors such as waves in the easterlies or tropical cyclones. The Raymond et al. (2006) mechanisms did not invoke dynamical instabilities and their numerical simulations show large error standard deviation over the convective region (north of 7°N). They also note the presence of westward moving disturbances but do not offer an explanation on how the formation of these transients fits in their theory. Additionally, numerous modeling studies have attempted understanding the role of parameterization of moist processes in determining the location of ITCZ (e. g., Hess et al. 1993, Numaguti 1993).

While these studies have produced diverse results, the responsible mechanisms for off-equatorial ITCZ formation are still under debate. Following TW and THW efforts to explain the off-equator location of mean convection using inertial instability arguments, we pose the hypothesis that the basic structures of the mean ITCZ are determined by the response of the atmosphere to the large scale CEPG and the resultant inertialy unstable regime associated with the cross-equatorial advection of anticyclonic vorticity. Within the confines of this hypothesis, the location of convection occurs where the poleward advection of anticyclonic vorticity is balanced by the generation of cyclonic vorticity. The hypothesis will be discussed in detail in Chapter 4.

1.2.3 East Pacific ITCZ variability

From one day to another, the representation of tropical convection is very different from the mean ITCZ depicted in the beginning of this section (i.e. Figure 1.2a). As seen in Figure 1.2d, ITCZ convection is very dynamic and changes intensely on synoptic time scales. These changes are associated with the existence of several smaller disturbances, most of which travel westward at speeds of approximately 8-10 ms^{-1} and have observed wavelengths of 2000 to 3000 km and a period of oscillation of 3-6 days. These disturbances were initially described by Riehl (1945) and Palmer (1951, 1952) and then more systematically by Yanai et al. (1968), Chang (1970) and Raymond et al. (1998) as satellite data became available The perturbations are known generally as tropical easterly waves and it has been suggested that they are an essential component of the mean ITCZ (e.g., Holton et al. 1971, Chang 1973). There is a practical motivation for understanding easterly wave formation processes since a large proportion of these waves

in the North Atlantic, North Pacific and southern Indian Ocean evolve into tropical storms that often attain hurricane or typhoon intensity. Figure 1.4 shows the genesis location of all northern hemisphere hurricanes formed during the 1970-2005 time period. The eastern Pacific Ocean is the most active tropical storms formation region on Earth (most genesis events per unit area per unit time) that attain hurricane intensity. Each year, on average, nine of these storms reach hurricane intensity. It has been suggested that nearly all of the tropical cyclones that occur in the East Pacific Ocean originate from easterly waves (e.g., Avila and Clark 1989, Raymond et al. 1998). An interesting feature of Figure 1.4 is that in both the East Pacific and Atlantic Ocean major storms appear to form north of 10°N and very few to the south of this latitude. What sets the latitudinal demarcation of tropical cyclonic activity it is still unclear. Understanding the physical mechanism responsible for generation of easterly waves and what sets the latitude of formation of these waves formation may lead towards a better understanding of tropical storm genesis.

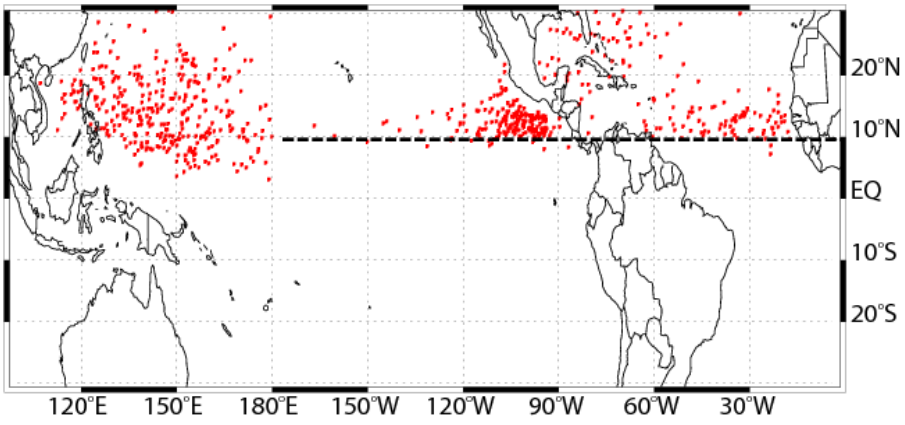

Figure 1.4: Map of genesis location of all hurricanes (category 1 to 5) formed in the Northern Hemisphere during the 1970-2005 time period (from March to November). Note the distinct latitude demarcations of formation (doted black line along 10°N) in the eastern Pacific and Atlantic oceans where strong CEPGs exist. Data obtained from www.weather.unisys.com

Over the last decades various theories have been proposed to explain the genesis of easterly waves and their role in the tropical circulation. Bates (1970) considered them as basic instabilities of the climatological ITCZ. Mak (1969) posed the hypothesis that equatorial waves were forced laterally by mid-latitude baroclinic disturbances. Holton et al. (1971) suggested that dynamic atmospheric instabilities determine the location of synoptic scale disturbances and that these disturbances are the building blocks of the ITCZ climatology. Burpee (1972) suggested that easterly waves over Africa, some of which were thought to propagate into the Pacific Ocean (Frank 1970), were the result of an unstable lower tropospheric easterly jet stream over Arica caused by temperature contrasts between the elevated Ethiopian highlands and the plains to the south. Thorncroft and Hoskins (1994) generalized the African easterly wave problem and concluded that is due to joint baroclinic-barotropic instability modified by convective heating. Schubert et al. (1991), Ferreira and Schubert (1997) and Wang and Magnusdottir (2005) suggested that westward-propagating disturbances are the result of hydrodynamical instability of the ITCZ itself and argued that that the ITCZ breakdown can increase the frequency of tropical cyclogenesis west of Central America and in the east Pacific Ocean.

Other studies argue that virtually all the eastern Pacific Ocean tropical cyclones develop in association with waves originating over the African continent that propagate across the Atlantic and Central American continent (e.g., Avila and Pasch 1992, Shapiro 1986). Some studies have linked eastern Pacific convective activity to intraseasonal oscillations (ISO) associated with the Madden-Julian oscillation (Madden and Julian 1972). It was suggested that the active phase of the ISO is more favorable that its

suppressed phase to the development of tropical storms in both the Pacific Ocean and Atlantic Ocean (e.g., Maloney and Hartmann 2000). Molinari et al. (1997) hypothesized that ISO events influence the easterly waves propagating from Africa or generated locally in the Caribbean region. Alternatively, it is suggested that the terrain that exists in Central and South America blocks the lower tropospheric easterly flow leading to a barotropically unstable jet downstream and thus to genesis of tropical disturbances (e.g., Zehnder and Gall 1991, Farfan and Zehnder 1997). However, a recent study by Serra et al. (2008) finds the formation and the character of the Pacific waves to be quite different from their Atlantic counterpart; suggesting that the majority of Pacific waves were created *in situ*.

1.3 Summary

There are a number of fundamental questions about the structure and maintenance of the ITCZ and easterly waves. What is still lacking is a general theory for easterly wave genesis or, at least, a differentiation of processes that produce waves in different regions of the tropics. Using a combination of diagnostic, theoretical and modeling studies we will attempt to provide answers to the following questions:

(i) What are the fundamental processes that determine the location of the mean ITCZ and its relationship to the large scale MSLP and SST fields?

(ii) Why does the mean ITCZ change its character across the Pacific Ocean? For example, why is the mean seasonal convection apparently deeper in the eastern Pacific Ocean (suggested by lower values of OLR) than in the central-western Pacific?

(iii) What is the role of transients in determining the position and intensity of the mean ITCZ?

(iv) What is the genesis process of these transients? Are the easterly waves produced by perturbations generated remotely (e.g., Africa or higher latitudes) or are they the result of regional instabilities? Are there regional differences in the genesis mechanisms of easterly waves? What produces the 3-6 day period and the characteristic scale of the waves?

(v) Why is there a second shallower lower-tropospheric ITCZ occurring within the deeper mean meridional circulation? Is this representative of the mean structure or a statistical ensemble of two mean states of the cross-equatorial meridional circulation?

Chapter 2 describes the observational datasets used in this study and provides an overview of the regional model used to complete the numerical simulations. Chapter 3 discusses the differences in horizontal and vertical mean ITCZ structure between the eastern and central Pacific regions, and the associated temporal variability, with focus on high frequency variability in the 4-8 day band. Chapter 4 examines the transient nature of the ITCZ with the aid of composite analysis. Dynamical balances that occur in both the mean and during oscillations of the ITCZ are discussed. We investigate whether the ITCZ transients are the manifestations of instability of the mean ITCZ. It will be argued that the genesis of the easterly waves is the result of the continual inertially unstable region under the action of a strong CEPG. Chapter 5 describes the results of a series of controlled numerical experiments designed to test alternative hypotheses that examine the origin of easterly waves in the eastern Pacific.

CHAPTER II

DATASETS, MODELS AND GENERAL METHODOLOGY

2.1 Observational datasets

The observational dataset used as a primary diagnostic in this study is the European Center for Medium-Range Weather Forecasts Reanalysis product (ERA40: Uppalla et al. 2005). It possesses a 1° by 1° horizontal resolution, 18 levels in the vertical and four times per day temporal resolution. While the ERA 40 dataset cannot be thought of as a pure observational dataset, Zhang et al. (2008) has shown that the observational-model mix reproduces observed fields quite well in the eastern Pacific.

Tropical OLR is commonly used as a proxy for precipitation as negative OLR anomalies are associated with positive anomalies of deep convection. We used a daily OLR product (Liebmann and Smith 1996) that has a 2.5-degree horizontal resolution and global coverage. The temporal coverage spans from June 1974 to the present. Daily OLR was obtained from the National Oceanic and Atmospheric Administration (NOAA) Climate Diagnostics Center (CDC), at their web site:
www.cdc.noaa.gov/cdc/data.interp_OLR.html.

The SST fields used are the weekly NOAA / National Center for Atmospheric Research (NCEP) 2D-Var optimally interpolated data described by Reynolds et al., (2002). The data set was obtained at: www.cdc.noaa.gov/cdc/data.noaa.oisst.v2.html.

The Global Precipitation Climatology Project (GPCP), version 2, monthly precipitation dataset described by Adler et al. (2003), was used for monthly mean rainfall

estimation. The monthly precipitation data set covers a 27-year period from January 1979 to the present. This product has a 2.5° spatial resolution and it is based on several measures of precipitation like the infrared and microwave retrievals. This dataset is obtainable from: precip.gsfc.nasa.gov.

Due to uncertainties concerning the quality of the atmospheric data prior to 1979 (introduction of satellite products) we limited our analysis period to the 1981-2000 time interval.

Absolute vorticity, relative vorticity, horizontal wind divergence, absolute vorticity advection and vortex tube stretching fields were numerically derived for each grid point, using the central difference method. Potential temperature, equivalent potential temperature and relative humidity at each grid point were calculated following Curry and Webster (1999).

2.2 Characterizing high frequency variability

Synoptic scale processes in the tropical rainfall band are of special interest for the present study. To isolate the anomalies of several meteorological fields in the 4-8 days range, a bandpass filter using a Lanczos smoothed symmetric non-recursive Fourier method filter (Duchon 1979; Press et al. 1989) was applied to the 1981-2000 time series. The discrete wavelet transformation method (e.g., Torrence and Compo 1998) was used to investigate the evolving temporal patterns in terms of frequency. A Morlet wavelet function was used as the mother function. The scale-averaged global wavelet power spectrum and the mean amplitudes in the 4-8 day band of OLR, meridional wind and relative vorticity were calculated using this technique.

2.3 Modeling study

The next-generation mesoscale numerical weather prediction system Weather Research and Forecasting (WRF: version 2.2, Skamarock et al. 2005) was used to test hypotheses through controlled experimentation. WRF was developed at National Center for Atmospheric Research (NCAR) and it is available at: http://www.mmm.ucar.edu/wrf/users/downloads.html and it is used for both prediction of mesoscale weather in an operation mode and for research purposes. WRF was chosen for this study because of its numerous physics options and its suitability to conduct experiments and idealized simulations across various spatial scales. A detailed description of the WRF model, parameterization schemes used and the different experimental setups is presented in the beginning of Chapter 5.

CHAPTER III

MEAN AND VARIABLE CHARACTERISTICS OF EAST PACIFIC ITCZ

The present chapter opens with an overview of the mean ITCZ during both boreal winter and summer for two distinct sections in the Pacific Ocean and continues with an examination of ENSO influence on the east Pacific ITCZ structure. A detailed investigation of the ITCZ temporal variability on interannual and synoptic timescale is presented as well.

3.1 General characteristics of the east Pacific ITCZ

From a climatological perspective, the ITCZ is a dominant feature in both the annual cycle and interannual variability of the tropics. Also, a large percentage of the short-term (daily) variability occurs within the ITCZ. However, it is important to note that the ITCZ is very different in character when viewed as a long-term mean or synoptically (several days). From day to day, ITCZ is highly dynamic and it rarely resembles its textbook schematic description as a region of steady state precipitation and mean uplift. Rather, it is usually made up of a series of distinct disturbances of orders of a few hundred kilometers, separated by regions of clear skies.

3.1.1 Characteristics of the lower tropospheric cross- equatorial flow

Despite the equatorial symmetry of the annual mean solar insolation, and even though there is a southern hemisphere insolation maximum during the boreal summer, the

band of high SST and its associated ITCZ convection possesses a northward location throughout the year in both the eastern Pacific and Atlantic Ocean. Figure 3.1 shows the spatial distribution of the long term average (1981-2000) 10 m winds speed and direction and, horizontal wind divergence at 10 m across the Pacific Ocean for boreal winter and summer. It is important to note that the low level flow in the East Pacific Ocean has a northward component during both winter and summer season although relatively stronger in the boreal summer. The thick black line superimposed on the diagram represents the zero absolute vorticity contour ($\eta=\zeta+f=0$) at 10 m. It has been argued in Chapter 1 that at low levels, in the northern hemisphere regions between the equator and $\eta=0$ line are inertially unstable. The relevance of this aspect and it the underlying mechanism will be discussed in detail in Chapter 4.3. The area of maximum low level divergence in the East Pacific, is always located equatorward of the $\eta=0$ line or intersects the $\eta=0$ line. For the central Pacific Ocean maximum low-level divergence occurs at the equator in both cases. Strong surface convergence in the eastern Pacific Ocean occurs in the northern hemisphere in both winter and summer, with maximum located at about 5°N during DJF and at about 8-10°N during JJA. Conversely, in the central Pacific Ocean, areas of low-level convergence are present on both sides of the equator. We will revisit the importance of these distinctive features in Chapter 4. Figure 3.2 shows the OLR distribution for the Pacific Ocean similar to Figure 1.2a except for the long term DJF and JJA seasonal average. In the east, the maximum convection in DJF occurs north of the equator near 10°N between 150°W-120°W, further from the American continent than during the summer.

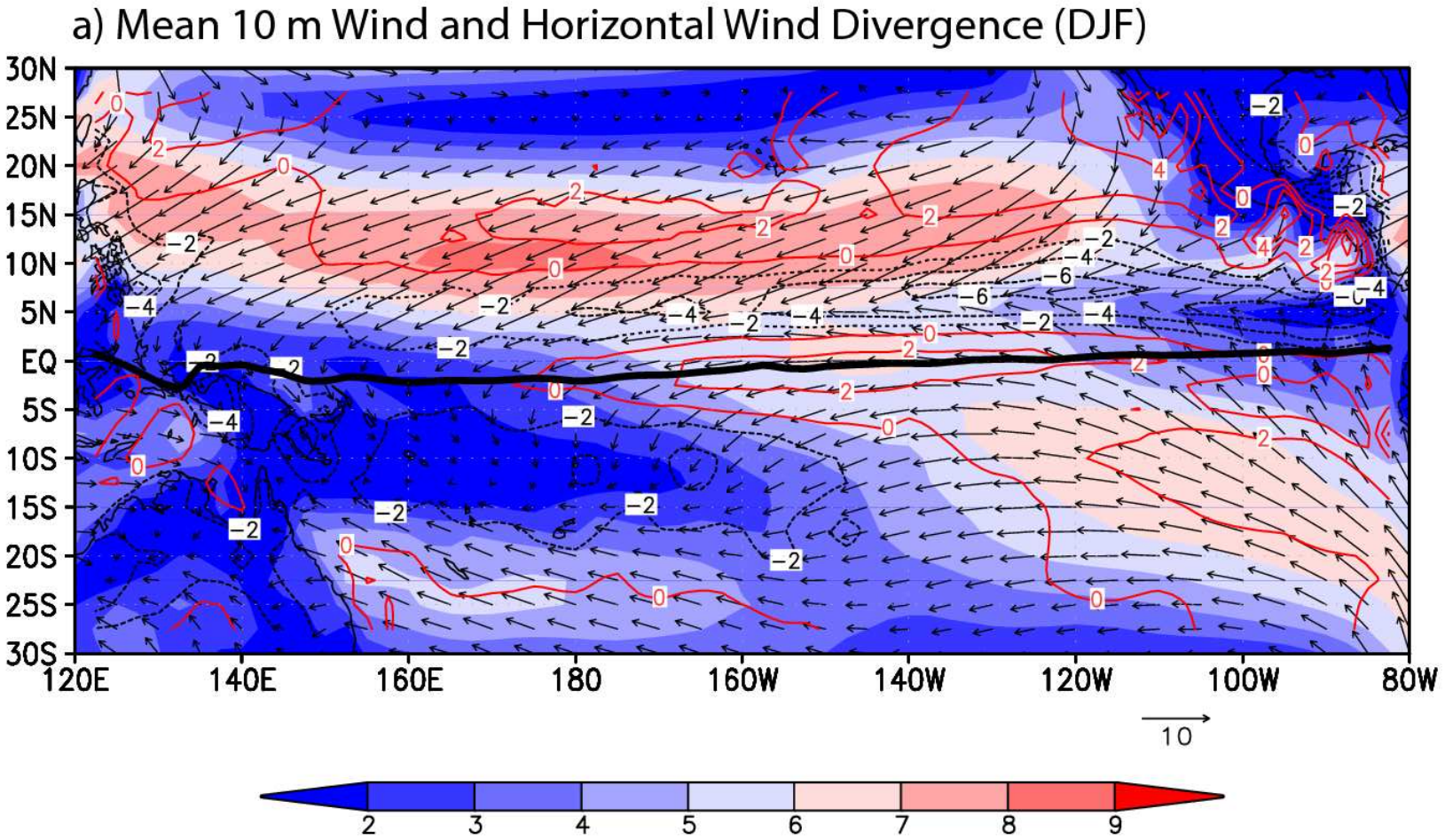

Figure 3.1: Long term mean (1981-2000) distribution of 10 m wind direction and speed (shading relative to bar below, units: ms^{-1}) and horizontal wind divergence at 10 m (contours, units: 10^{-6} s^{-1}) over the Pacific Ocean for (a) December-February and (b) June-August seasons.

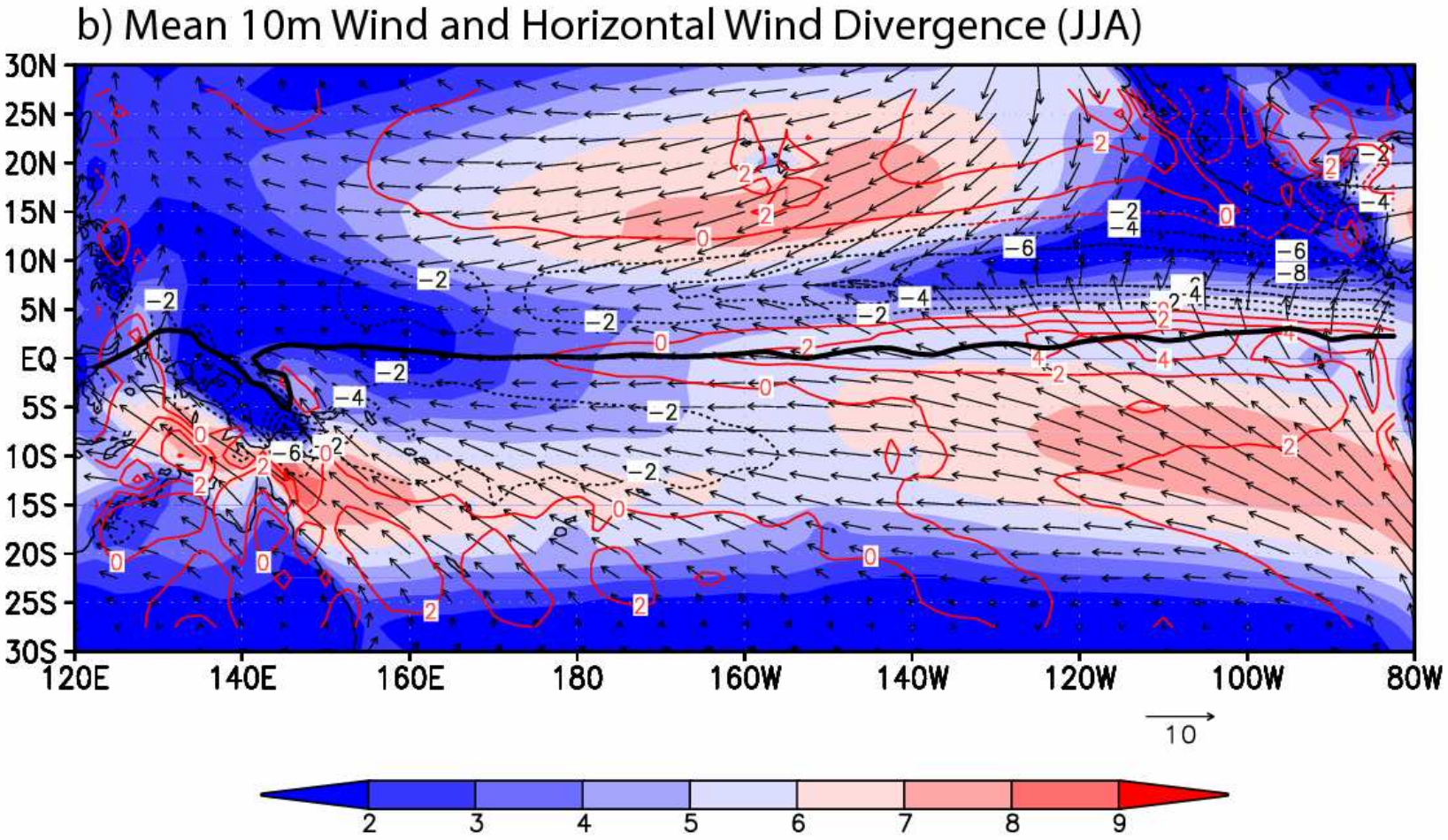

Figure 3.1: (cont.)

In JJA, in agreement with the low level convergence patterns observed in Figure 3.1 and analogous to the 1996 summer example (Figure 1.2a), the tropical convection is organized in a narrow zonally oriented band centered near 10°N. The character of the central Pacific Ocean ITCZ has very different structure compared to its eastern counterpart with convection occurring on both sides of the equator. It includes the southeastward oriented convective region SPCZ extending from the western Pacific warm pool towards French Polynesia. The same orientation occurs in both season but with a higher OLR magnitude during DJF.

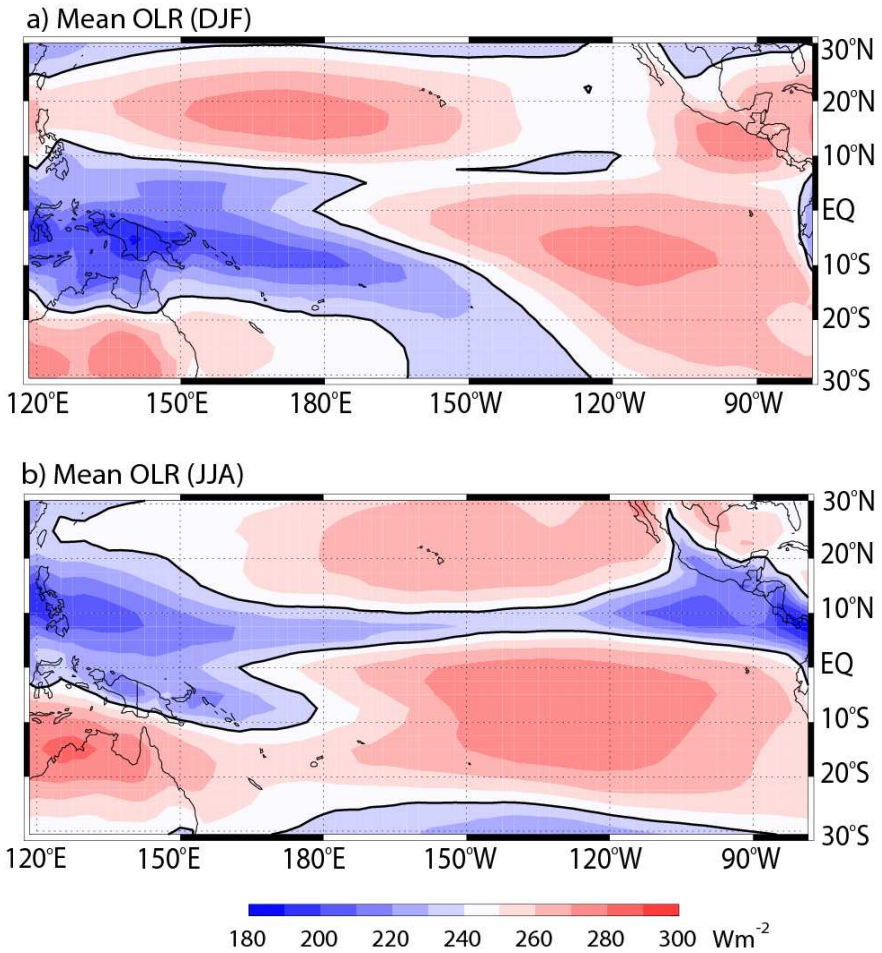

Figure 3.2: Long-term mean distribution of OLR (Wm^{-2}) over the Pacific Ocean for (a) DJF (1981-2000) and (b) JJA (1981-2000). The dark line represents the 240 Wm^{-2} contour.

3.1.2 Characteristics of the mean meridional circulation

The upper panel of Figure 3.3 shows the mean boreal summer (June-August) meridional circulation for the period 1981-2000 averaged between 180°W to 170°W (Figure 3.3a) and 120°W to 110°W (Figure 3.3b) in terms of mass streamfunction ψ. The Stokes streamfunction ψ is derived from a downward integration of the meridional mass flux (e.g., Hartmann 1994).

It is important to note that because the mass stream function is calculated for a limited longitudinal domain there is no requirement for mass conservation in the longitudinal section as there would be if the meridional circulation were calculated as a zonal mean. This same consideration attends Figures 3.4 and 3.5 as well.

For better graphic visualization, Figure 3.3 displays the central Pacific section on the left-hand side and the East Pacific section on the right-hand side. However, we will start by examining the region of main interest in this study, the east Pacific. The region in Figure 3.3b is chosen because of its typical off-equator ITCZ regimes as identified by TW and because of the recent attention given to the region in the Eastern Pacific Investigation of EPIC 2001 experiment (e.g., Raymond et al. 2004). The figure shows a broad band of rising motion located between 6°N and 12°N with descent to the south and weak ascent to the north. There is also a hint of the shallower lower tropospheric circulation with a return flow in the lower to middle troposphere. Associated with the ascending motion is a plume of moist air that extends upward from the boundary layer, through the middle troposphere to above 200 hPa. At the equator, there are southerly boundary layer winds with speeds greater than 6 ms^{-1}. The return flow aloft has speeds exceeding 8 ms^{-1}. A second, although weaker, southward maximum of 2 ms^{-1} occurs

between 700 and 600 hPa also over the equator. In both panels of Figure 3.3b, the zero absolute vorticity contour ($\eta = 0$: plotted as the bold dashed line) bisects the meridional wind maximum in the lower troposphere. Equatorward of the zero contour, the northward winds accelerate whilst, on the poleward side, there is a region of very rapid deceleration corresponding in location to the rising arm of the meridional cell. The result is a boundary layer divergence-convergence doublet centered on the $\eta = 0$ contour. These are important factors that will be discussed in Chapter 4. In the upper troposphere there is a strong region of divergence located directly above the boundary layer convergence with strong southerly winds to the south and a substantial southward displacement of the $\eta = 0$ contour into the southern hemisphere.

Figure 3.3a is the counterpart of Figure 3.3b for a location 8000 km to the west (180°W-170°W). A quantitatively different meridional circulation structure emerges. Near the equator, the magnitude of ψ has decreased by a factor of four. Instead of a strong cross-equatorial meridional circulation, the cell is confined to the northern hemisphere. Weak ascent occurs near the regions of maximum SST, as indicated by the OLR minimum in Figure 3.2b. Boundary layer convergence is also much weaker and the $\eta = 0$ contour is aligned with the equator throughout the vertical. Figure 3.4a and b illustrate the mean boreal winter (December-February) meridional circulation for the period 1981-2000 for the same two Pacific sections [180°W-170°W] and [120°W-110°W], respectively. For the eastern region (Fig. 3.4b), the magnitude of the streamfunction has decreased slightly compared to JJA meridional circulation. Also, the rising branch of the ITCZ is much closer to the equator than in the JJA case and it is centered at about 5°N.

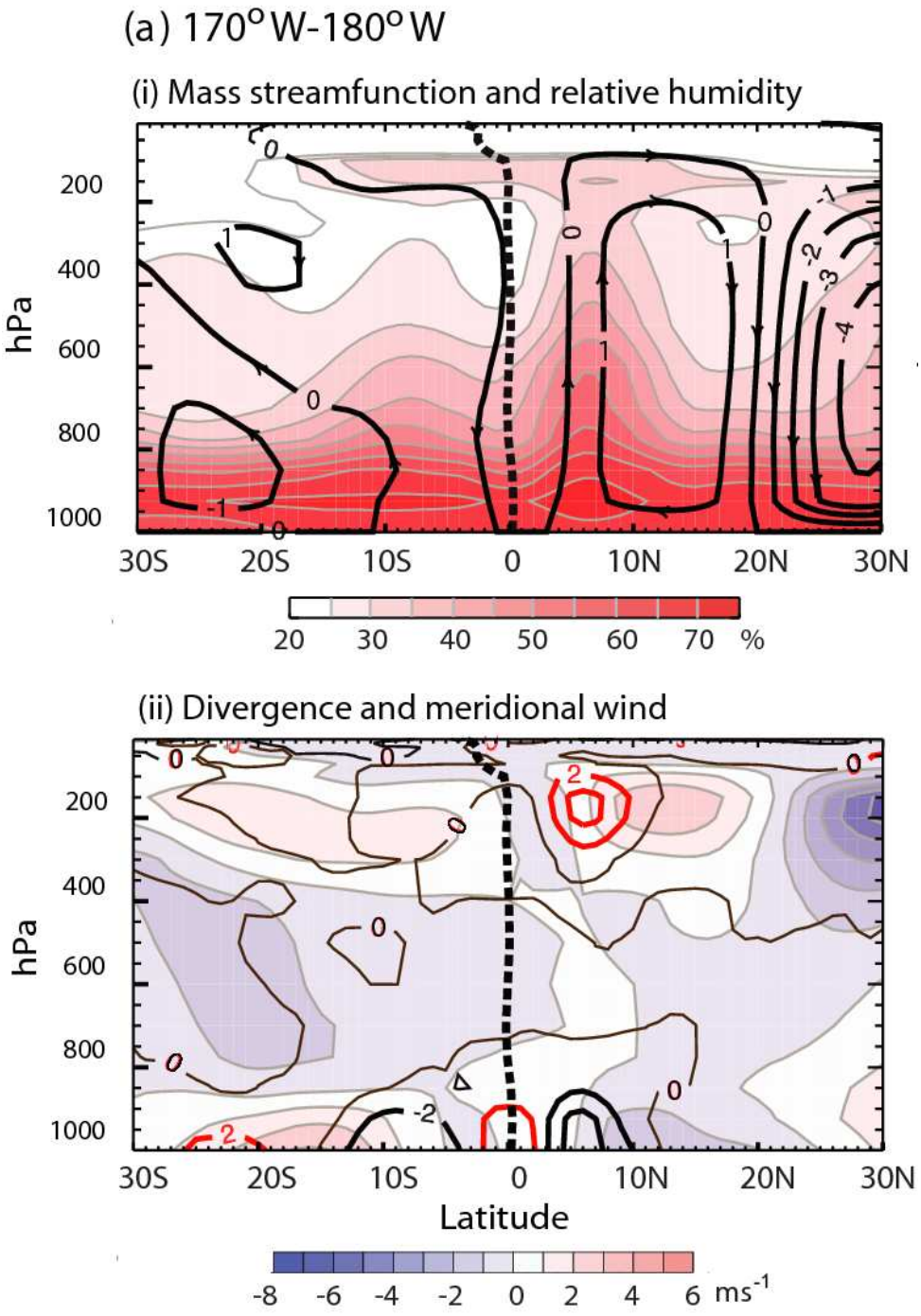

Figure 3.3 Characteristics of the mean 1981-2000 summer (June-August) meridional circulation in the Pacific Ocean averaged for (a) 180°W to 170°W and (b) 120°W-110°W. Panel (i) shows the mass streamfunction (ψ : contours with units: 10^{11} kg s^{-1}) and relative humidity (shading relative to bar below figure: %). Panel (ii) shows horizontal wind divergence (units: 10^{-6} s^{-1} with red contours – positive, black contours – negative) and meridional wind (shaded contours units: ms^{-1}, bottom scale).

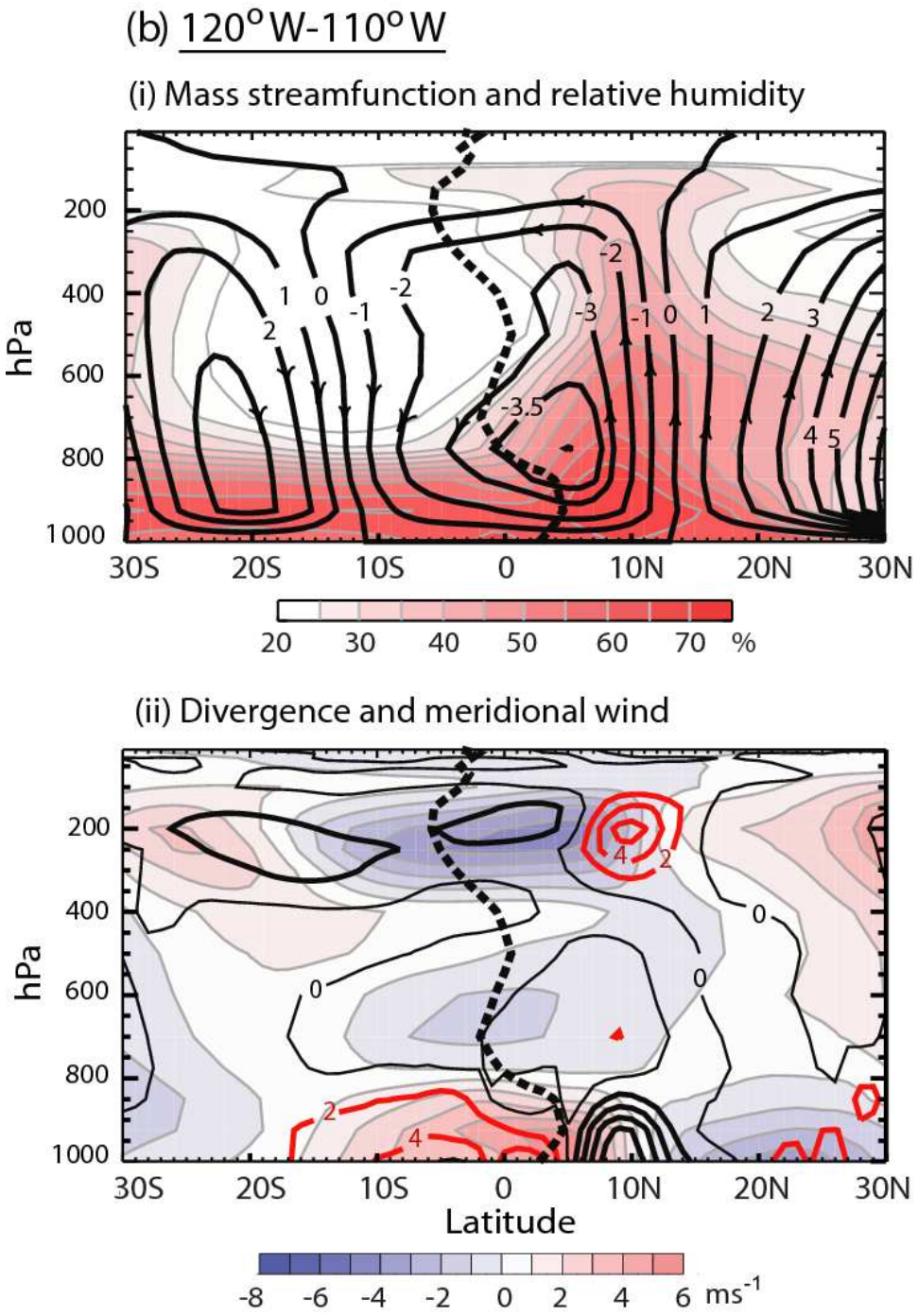

Figure 3.3: (cont)

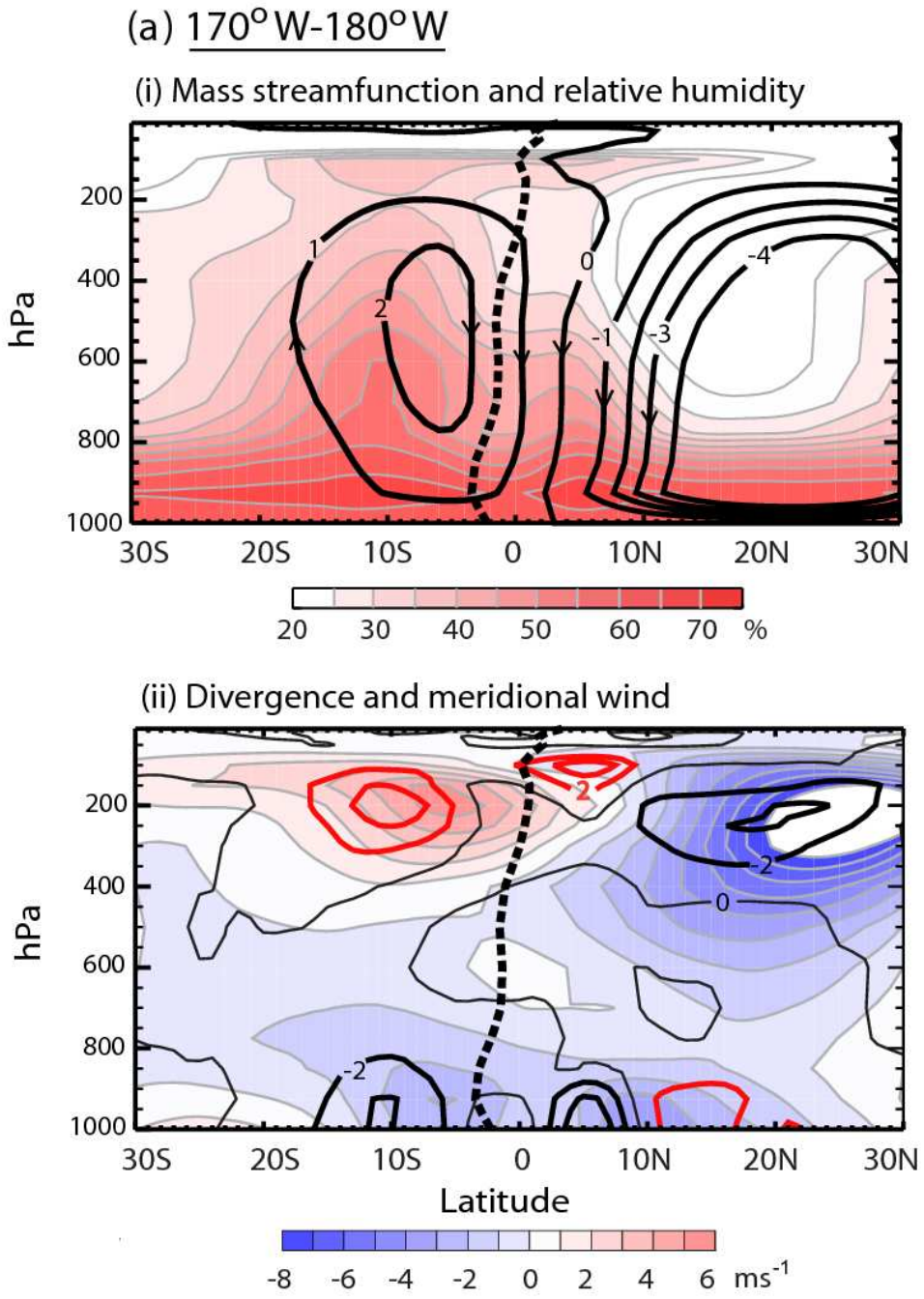

Figure 3.4: Similar to Figure 3.3 except for the winter season (December-February, 1981-2000).

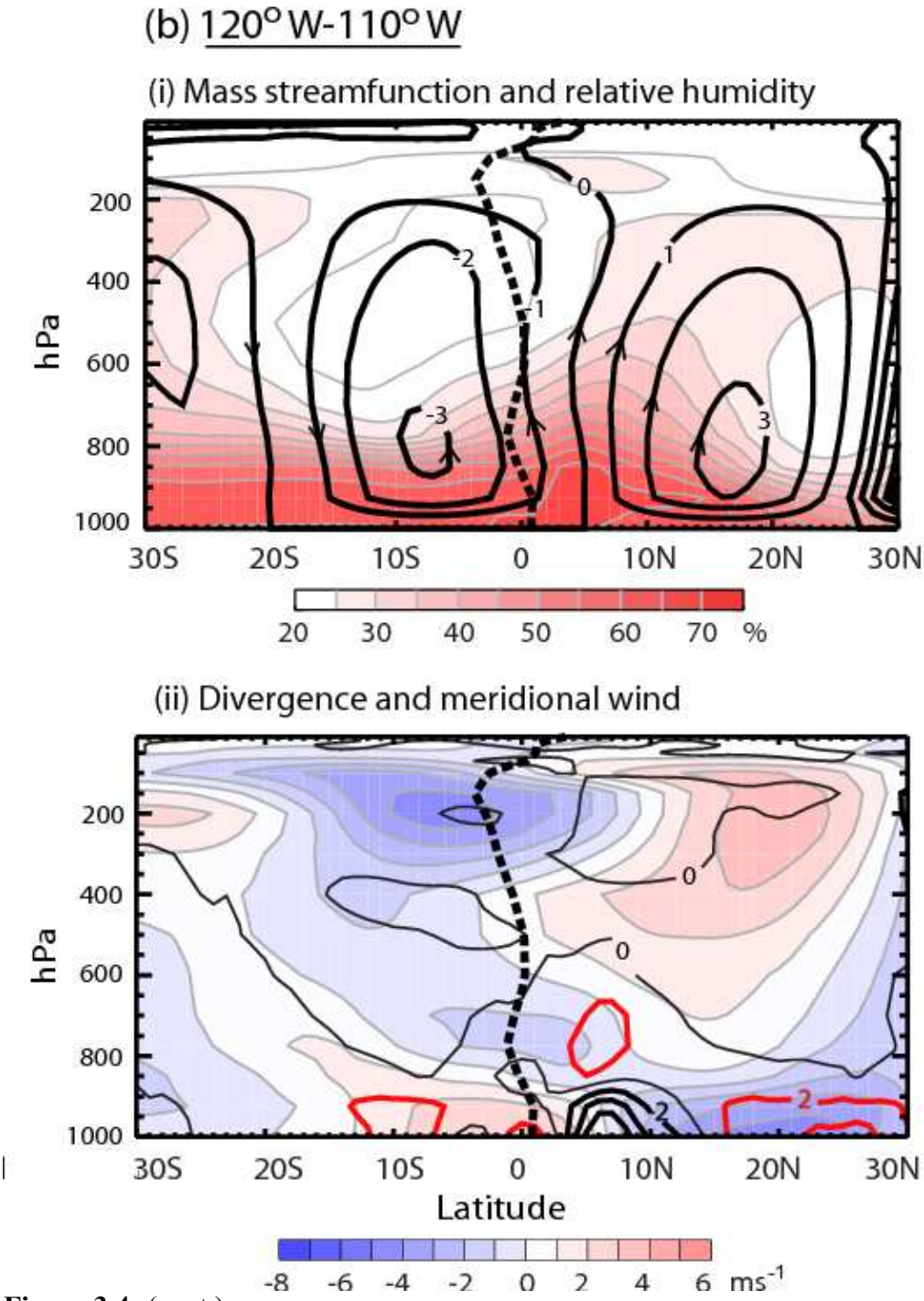

Figure 3.4: (cont.)

The middle and upper troposphere is much drier than in the summer case (Figure 3.3b). The magnitude of the low level southerly meridional wind has decreased compared to

JJA, with maximum at the equator of 4 ms^{-1}. For the central Pacific section (Figure 3.4.a), boundary layer convergence, corresponding to the areas with OLR < 240 Wm^{-2} illustrated in Figure 3.2 occurs on both sides of the equator, in the regions of maximum SST.

In summary, across the expanse of the Pacific Ocean, there is a distinct change in associations between SST, MSLP, OLR, the dynamical fields and the strength of the ITCZ. Two different regime-types appear to exist in the Pacific Ocean. The first type is where the meridional circulation is strong and inter-hemispheric and where the SST and MSLP are located poleward of the convective maximum (Figure 1.2b, c) and Figure 3.3b). The second type has a weaker circulation (Figure 3.3a) and SST and convection are more aligned. The discriminating factor between the two types is the existence of a strong CEPG in the east. The eastern most circulation exists in a potentially inertialy unstable regime whereas the western circulation appears inertially stable. This is more evident during the boreal summer season.

3.2 Characteristics of the east Pacific ITCZ variability

One other significant characteristic of the ITCZ, aside from its longitudinal variability described above, is its variability on a large range of temporal scales. The east and Central Pacific ITCZ exhibits variability on interannual to synoptic time scales.

3.2.1 Interannual variability

The influence of SST distribution associated with the El Niño and La Niña episodes on the mean meridional circulation in the East and Central Pacific Ocean have been investigated. For this purpose, four El Niño (warm) and three La Niña (cold)

episodes, based on a threshold of ±0.7°C for the JJA season of the Oceanic Niño Index (ONI) [3 month running mean of Extended Reconstructed SST (ERSST.v3, Smith et al. 2007, available at http://www.cdc.noaa.gov/cdc/data.noaa.ersst.html) anomalies in the Niño 3.4 region (5°N-5°S, 170°W-120°W)] were selected. The threshold chosen is higher than the ±0.4°C threshold used commonly to define ENSO events (e.g., Trenberth 1997). However, with the higher threshold, only years with strong ENSO variability during the JJA season are considered. The selected years and the magnitude of the JJA SST anomalies for each year are presented in Table 3.1.

Table 3.1: The El Niño and La Niña events exceeding ± 0.7 °C for the JJA season, using SST anomalies in the Niño 3.4 region.

EL NIÑO EVENTS		LA NIÑA EVENTS	
Year	JJA SST Anomalies (°C)	Year	JJA SST Anomalies (°C)
1982	+0.8	1988	-1.4
1987	+1.5	1998	-0.7
1991	+1	1999	-0.9
1997	+1.7		

The underlying SST distribution in the East Pacific Ocean is quite different during the two ENSO phases. For example, there is a 5°C temperature difference between equator and 10°N during La Niña, versus 3.5°C during El Niño (Figure 3.5). However, on a larger scale, for example between 10°S and 10°N, the SST gradient for the two ENSO phases is similar. The large scale SST distribution sets the magnitude of the CEPG, and it will be shown in the next sections that the latitudinal limit of convection is given by the magnitude of the CEPG.

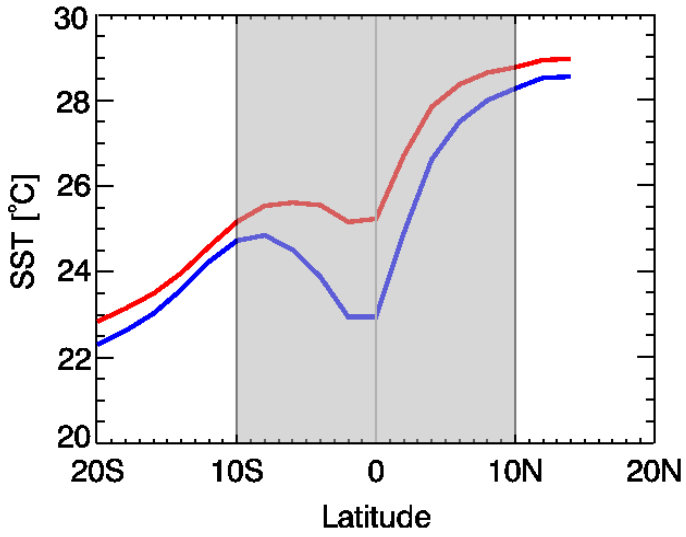

Figure 3.5: Mean SST distribution for the 120°W-90°W longitudinal band during the El Niño phase (red line) and La Niña phase (blue line).

Table 3.2: The latitudinal location of minimum OLR and maximum SST for the [120°W-90°W] for the El Niño and La Niña events identified in Table 3.1.

El Niño events			**La Niña events**		
Year	Latitude of min. OLR	Latitude of max. SST	Year	Latitude of min. OLR	Latitude of max. SST
1982	7.5°N	12°N	1988	10°N	12°N
1987	7.5°N	11°N	1998	10°N	11°N
1991	7.5°N	12°N	1999	10°N	12°N
1997	7.5°N	9°N			

Table 3.2 shows variations with latitude of the location of minimum OLR and maximum SST for the El Niño and La Niña years identified in Table 3.1. It is apparent that maximum convection and maximum SST are not collocated and generally convection occurs on the equatorward side of the maximum SST (minimum MSLP) as discussed previously. Moreover, convection occurs closer to the equator during the El Niño years than during the La Niña years.

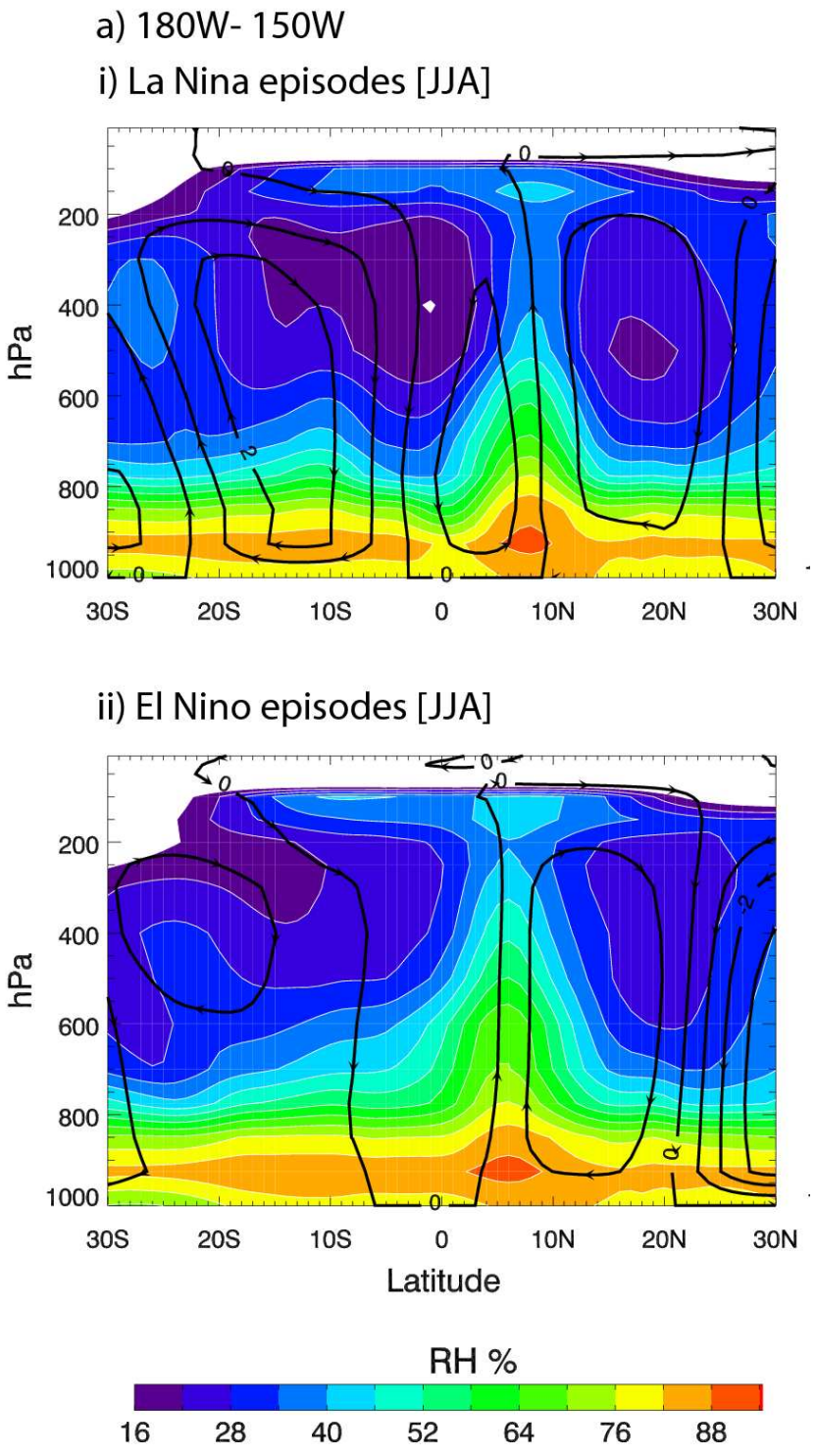

Figure 3.6: Characteristics of mass streamfunction (ψ : contours with units: 10^{11} kg s^{-1}) and relative humidity (shading relative to bar below figure: %) averaged for (a) 180°W to 150°W and (b) 120°W to 90°W longitudinal bands, during (i) la Niña phase and (ii) El Niño phase.

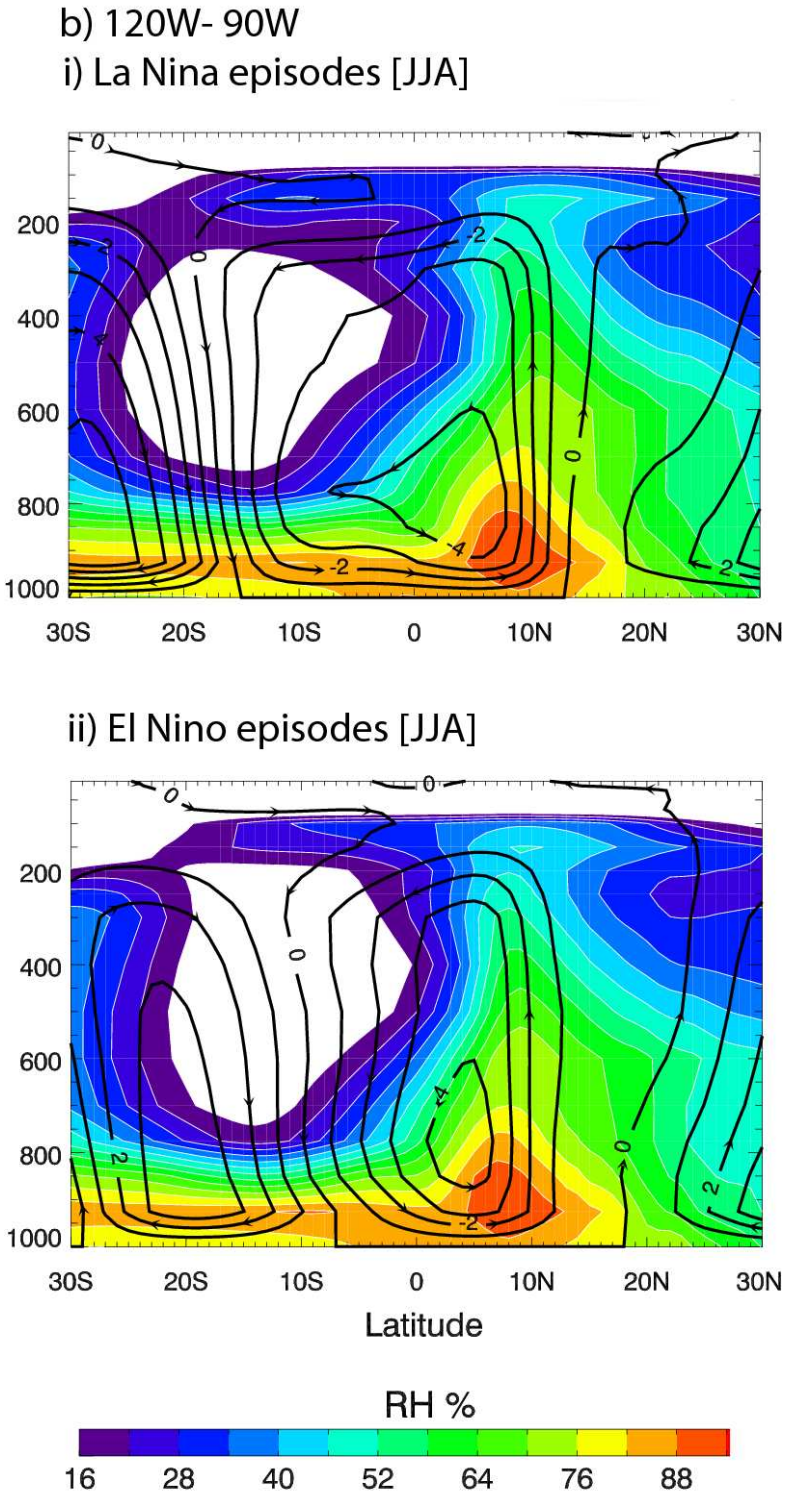

Figure 3.6: (cont.)

Figure 3.6 shows the differences between cold and warm ENSO phases in terms of mass streamfunction and relative humidity averaged for the same two longitudinal presented in subchapter 3.1.2. For the Central Pacific region (Figure 3.6a), during the La Niña phase there is indication of cross-equatorial meridional circulation developing (magnitude of the mass streamfunction $\psi \sim 10^{11}$ kg s^{-1}), with air rising at about 8°N and subsiding south of the equator. However, the cross-equatorial mass transport is not substantial, compare to the east Pacific counterpart. The El Niño conditions, for the most part are similar to the long term averaged profile presented in Figure 3.3. The east Pacific section depicted in Figure 3.6b shows some differences in the latitudinal extent of the MMC from La Niña to El Niño stage. For example, the MMC during La Niña phase extends from 7-12°N (the rising branch) to about 15°S (the descending branch), while during the El Niño phase is limited between 7-12°N and 7°S. However, the character of the mean meridional circulation remains the same in both cases.

Figure 3.7 shows the mean meridional wind and horizontal wind divergence profiles for the 180°W -150°W and 120°W-90°W longitudinal bands, for both La Niña and El Niño conditions. Generally the mean meridional circulation patterns are similar to the ones observed for the long term mean JJA fields (Figure 3.3) although there are some differences that should be mentioned. For example, the magnitude of mid-tropospheric northerly meridional wind in the 120°W-90°W section is larger for the La Niña case than for the El Niño case, suggesting a stronger shallow mean meridional circulation. In addition, at upper levels, the northerly meridional wind expands further south during the La Niña phase.

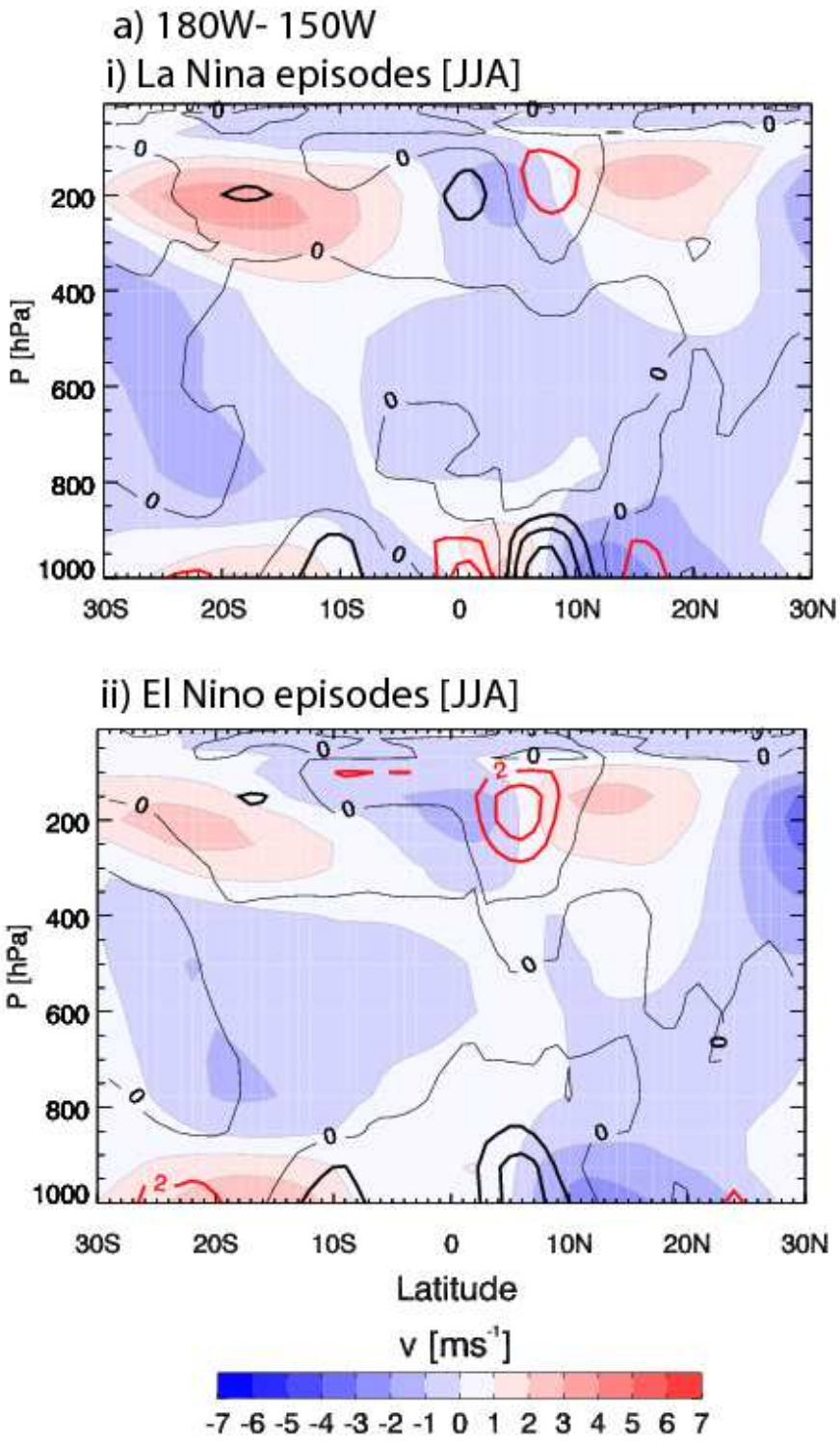

Figure 3.7: Similar to Figure 3.6, except for the meridional wind *v* (shaded contours, units: ms^{-1}) and horizontal wind divergence (units: 10^{-6} s^{-1} with red contours – positive, black contours – negative).

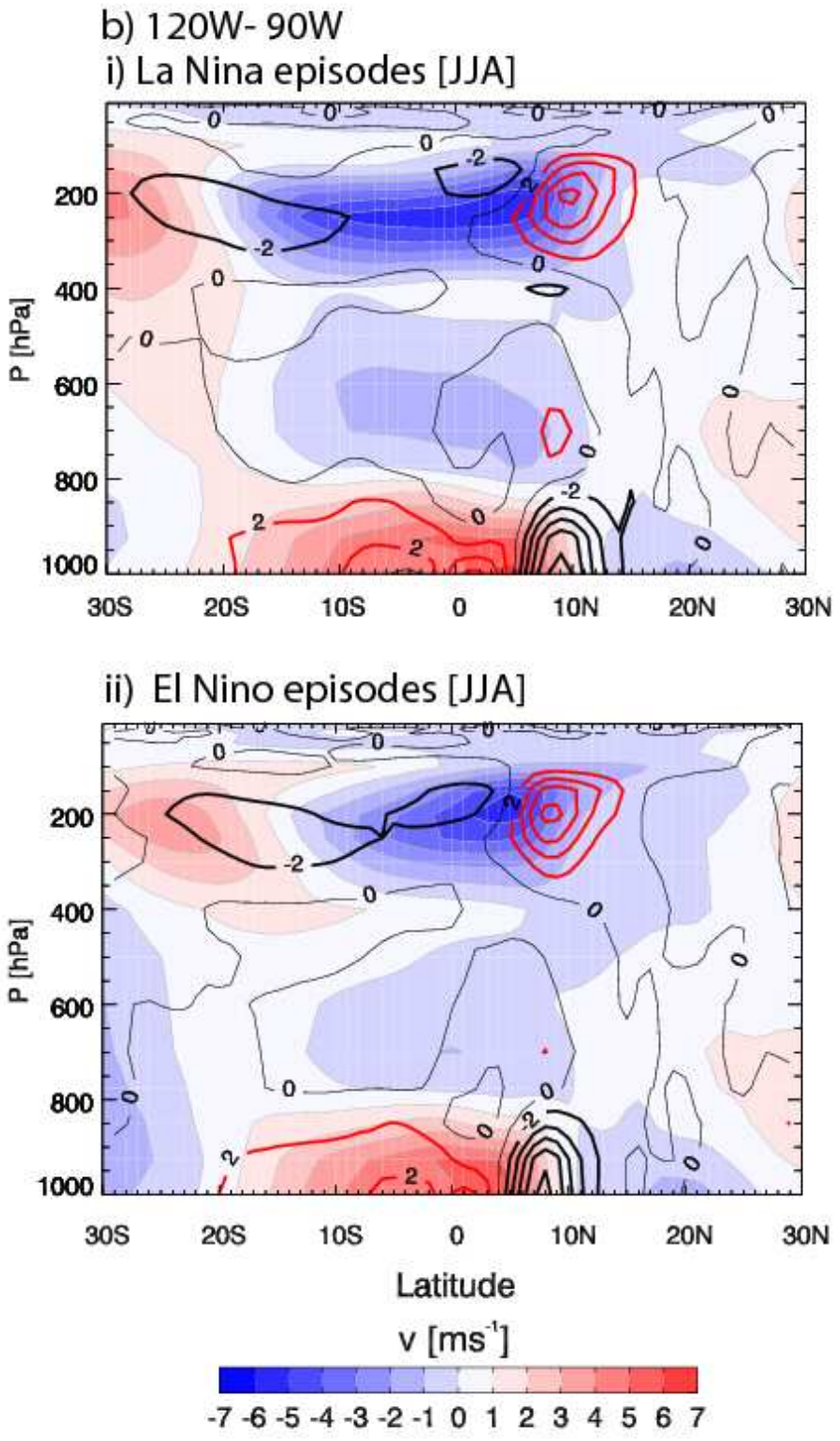

Figure 3.7: (cont)

3.2.2 Synoptic scale variability - Easterly Waves

Viewed on a day-to-day basis, the ITCZ assumes a very different form to the mean state discussed earlier. Figure 3.8 shows daily OLR time series at two locations: [110W°; 10°N] and [170W°; 10°N] for the 10-year period 1991-2000. Considerable high-frequency variability is evident in both sections with OLR alternating over a 200 Wm^{-2} range between convective and less-convective periods. In addition, during boreal summer, much lower values of OLR are observed than during winter.

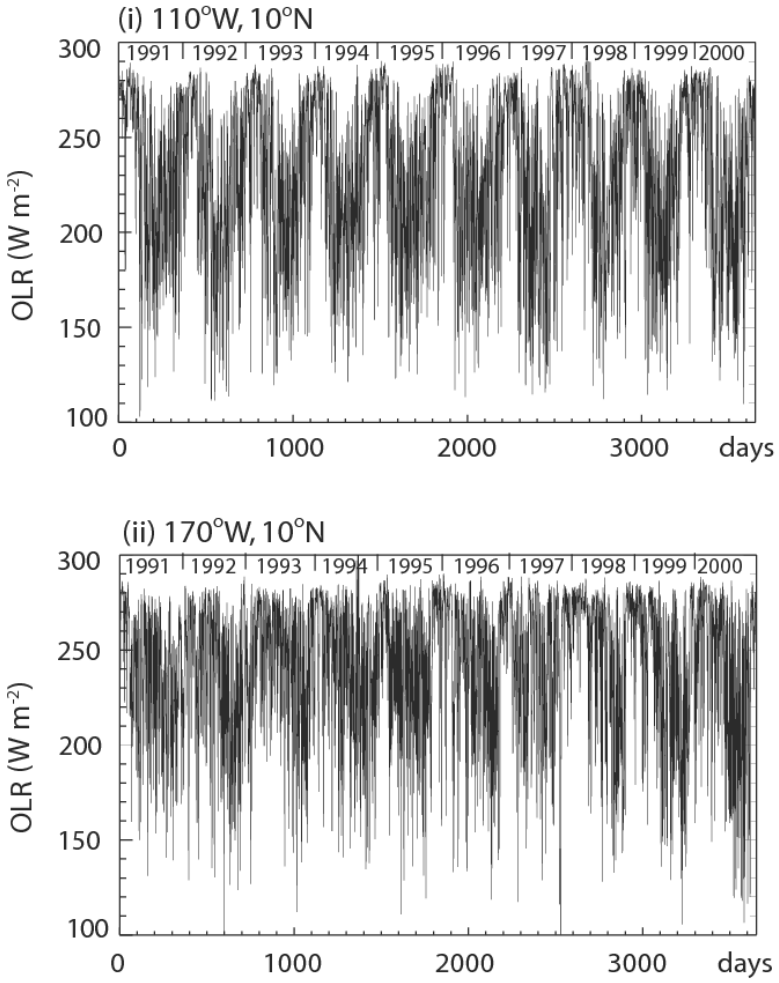

Figure 3.8: OLR time series (units: Wm^{-2}) at two locations in the Pacific Ocean: (i) [110W°; 10°N] and (ii) [170W°; 10°N] for the 1991-2000 time period.

Figure 3.9 shows a Hovmoller diagram of daily OLR values along 10°N during a period in 1996. An oscillation between convective and clear-sky periods, on time scales of 3-6 days, and a general westward propagation are evident. These disturbances known as "easterly waves" were initially described by Riehl (1945), Palmer (1951, 1952), Yanai et al. (1968), Chang (1970) and Holton (1971). More extensive analyses of the Pacific Ocean disturbances have occurred since (e.g., Serra and Houze 2002, Serra et al. 2008). In the Pacific Ocean there are about 6-8 easterly waves per month during summer, similar in number to those found in the North Atlantic (Serra et al. 2008).

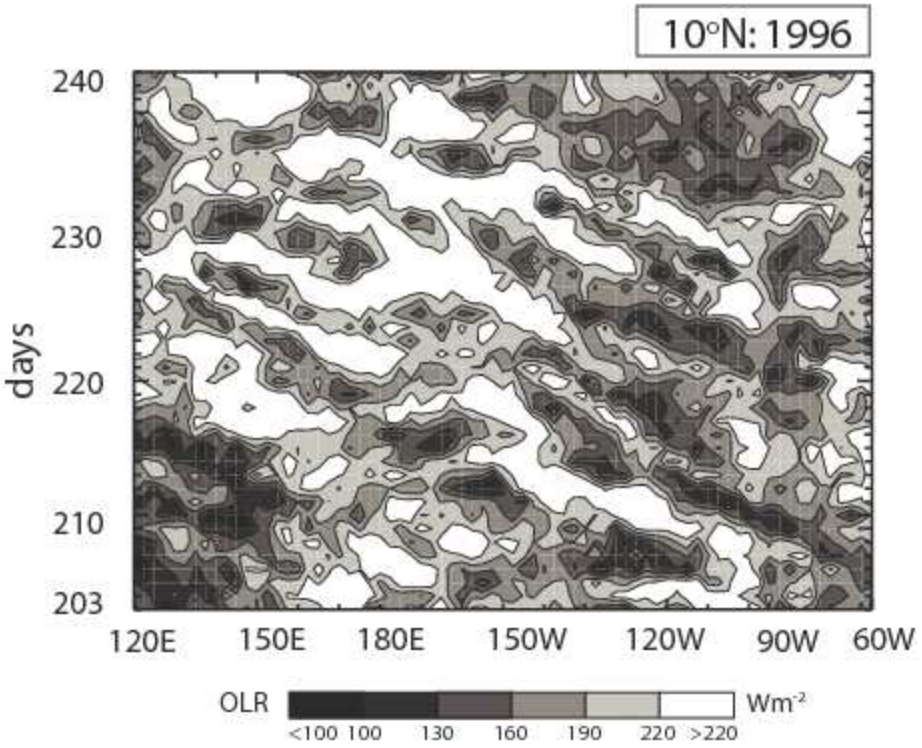

Figure 3.9: Time – longitude section of daily OLR (units: Wm^{-2}) along 10°N, between 120E° and 60°W for days 203-240 of year 1996.

The easterly waves' distinctive signature can be observed, not only in the moisture and cloudiness and precipitation fields, but also in the lower and mid-

tropospheric meridional wind and relative vorticity components. The temporal evolution of unfiltered meridional wind at 850 hPa and 600 hPa levels for the same period as in Figure 3.9, at [110W°; 10°N] and [170W°; 10°N], is presented in Figure 3.10.

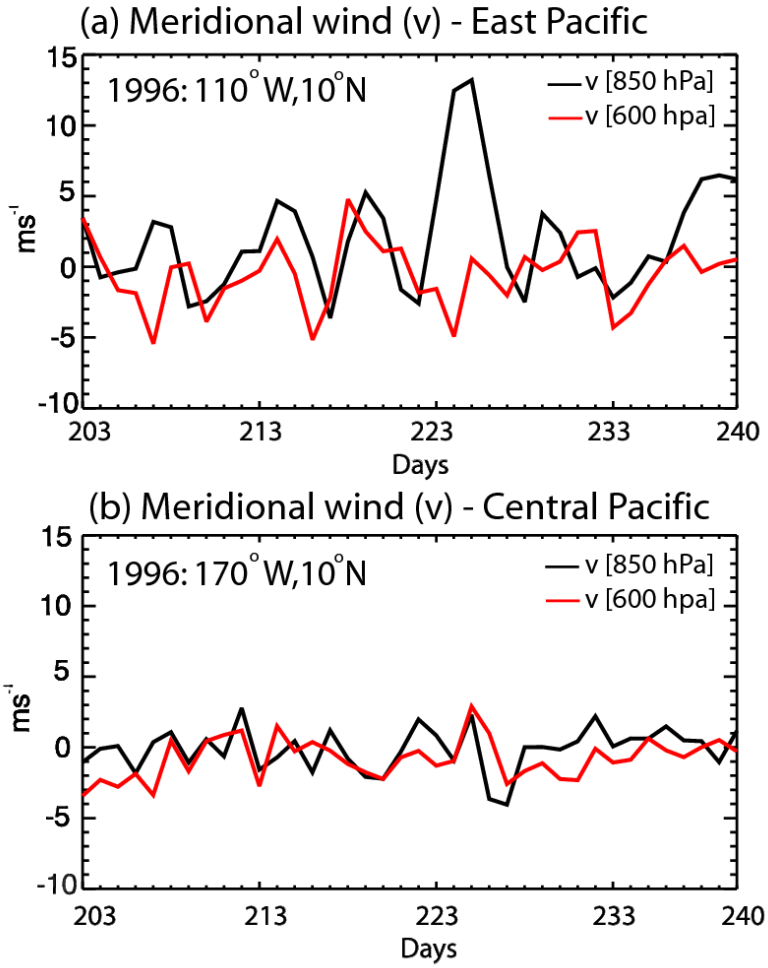

Figure 3.10: Meridional wind time series (units: ms^{-1}) at two locations in the Pacific Ocean: (a) [110W°; 10°N] and (b) [170W°; 10°N] for days 203-240 of year 1996.

The character of the oscillations in the two regions is different. In the eastern Pacific Ocean, distinct high frequency oscillations of meridional wind at both 850 and 600 hPa levels are evident. These oscillations have higher amplitude and there are well defined compared to the central Pacific section. This will be confirmed by Figure 3.11b.

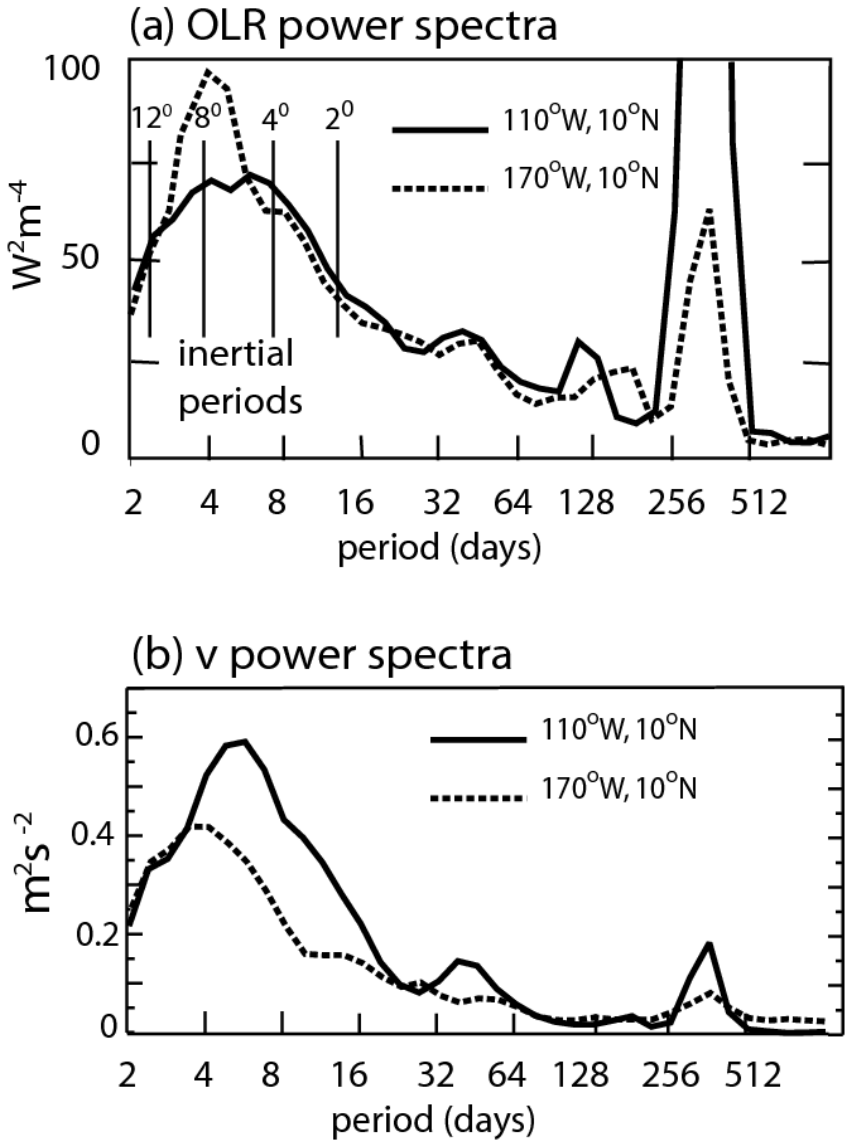

Figure 3.11: Scale-averaged global wavelet power spectrum of (a) OLR and (b) meridional wind (850 hPa) at two locations: [110°W; 10°N] (solid line) and [170°W; 10°N] (dashed line). Wavelet analysis is used in order to represent the scale-averaged global wavelet power spectrum in terms of coefficients of a mother Morlet wavelet (e.g., Torrence and Compo 1998).

Figure 3.11 shows a spectral analysis of the OLR time series and meridional wind at 850 hPa from 1981 to 2000 for the [10°N; 110°W] and [10°N; 170°W] regions. A ten-year time-series of the OLR was shown in Figure 3.8. A high amplitude and broad peak

in the 3-8 day range dominates the high frequency end of the spectra matching the inertial periods of latitude range assumed by $\eta = 0$ noted in Figure 3.3. For later reference, the values of the local inertial period ($\omega_i = \frac{2\pi}{\left[f\left(f+\zeta_g\right)\right]^{1/2}}$) are plotted in Figure 3.11. For relatively small values of ζ_g, these frequencies are 9.6 days at 3° from the equator, 5.7 days at 5°, 4.0 days at 7° and 2.9 at 10°. If inertial instability has something to do with the latitudinal location of the mean ITCZ, then one would expect transients to occur on time scales similar to local inertial frequencies. Furthermore, one would expect the scale of the CEPG to be instrumental in setting the time scale of the destabilization-stabilization process.

It will be shown in section 4.3.1 that the magnitude of CEPG determines the magnitude of cross-equatorial vorticity advection. In turn, convection occurs where convergence is a maximum, just poleward of the $\eta = 0$ contour. The latitudinal location of the ITCZ (defined here in terms of maximum convection) occurs where the advection of anticyclonic vorticity is balanced by the generation of lower tropospheric cyclonic vorticity by vortex tube stretching associated with convection. It is important to note that while the OLR amplitude in the 3-8 day range is larger for the central Pacific region, the meridional wind amplitude is higher in the eastern Pacific region. Figure 3.12 shows the OLR mean amplitude in the 4-8 days band for the entire year as well as for boreal summer and winter. The strongest amplitude variance occurs in the Pacific and Atlantic Oceans, north of the equator. Three distinct areas of maximum disturbance activity can be identified in the western and eastern Pacific, and the Atlantic Ocean, respectively. There is a secondary maximum south of the equator, coinciding with the South Pacific

Convergence Zone. The northwest Pacific location of OLR maximum amplitude matches fairly well the area of western Pacific tropical storms/cyclones formation. The Atlantic Ocean exhibits relatively strong variability as well, especially during boreal summer. The maximum amplitude in the 4-8 days band almost coincides with the areas of maximum mean deep convection for most tropical convective regions. This suggests that synoptic scale disturbances are essential components of the mean ITCZ.

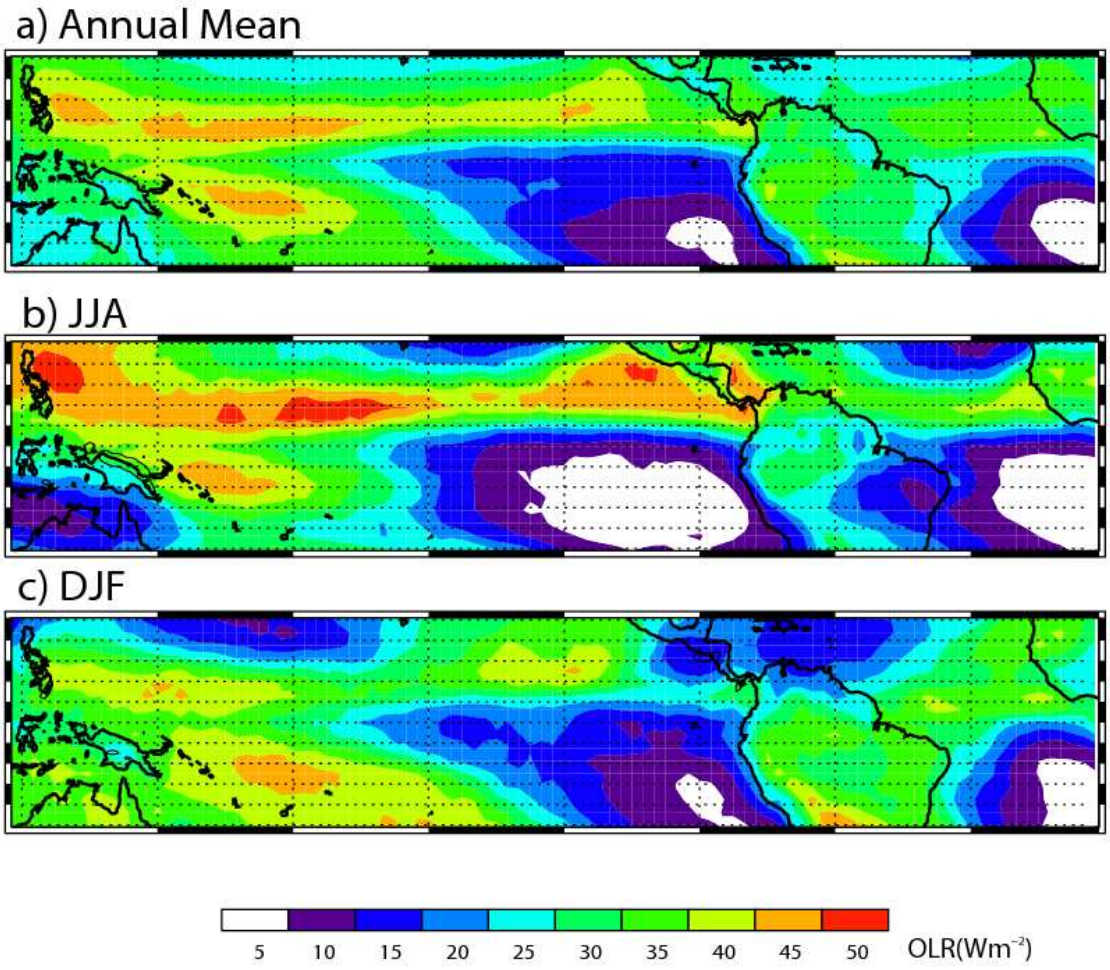

Figure 3.12: Long-term (1981-2000) mean amplitude of the OLR (units: Wm^{-2}) in the 4-8 days band for (a) Annual mean, (b) JJA and (c) DJF. Wavelet analysis is used in order to represent the ORL variability in each grid point in terms of coefficients of a mother Morlet wavelet.

Figure 3.13, similarly to Figure 3.12, shows the amplitude of meridional wind and relative vorticity at 600 hPa in the 4-8 day band for the entire year, the JJA and DJF seasons, respectively. Similar analysis was done for relative vorticity at 850 hPa (not shown) and the results are analogous to the results presented in Figure 3.13. A first examination reveals that the spatial distributions of the maximum amplitude of OLR, v and ζ, respectively do not agree very well. Regional maxima of relative vorticity are found in the northwest Pacific, eastern Pacific and Atlantic Ocean and African coast but not in the central Pacific Ocean. Additionally, the regions of maximum relative vorticity are not collocated with the regions of maximum meridional wind.

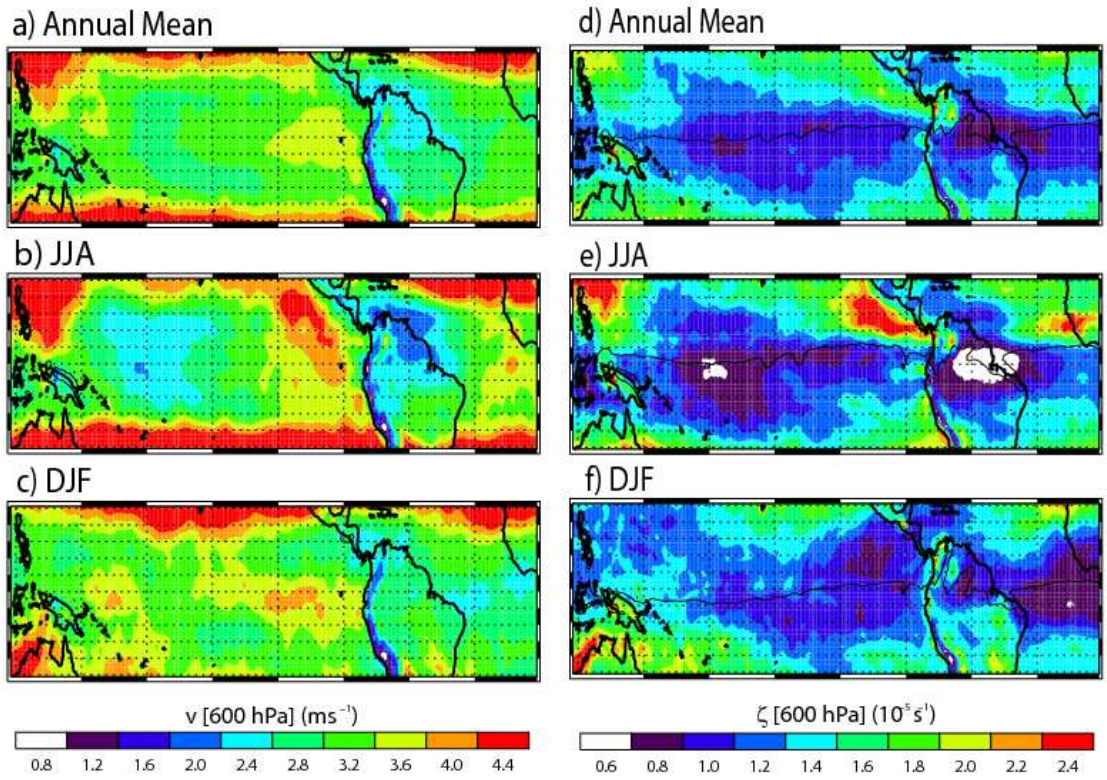

Figure 3.13: Similar to Figure 3.12 except for meridional wind at 600 hPa (units: ms^{-1}): a) to c) and for relative vorticity (ζ) at 600 hPa (units: ms^{-1}): d) to f).

A more careful inspection of Figure 3.13b reveals a meridional elongated and relatively narrow band of the meridional wind disturbances extending from the equator northward. No similar distribution of either mean OLR or mean relative vorticity exists. The relevance of this aspect will be discussed in section 4.

3.3 Summary

The mean vertical - meridional circulation in the eastern Pacific for both summer and winter is composed of a deep cell (with rising motion located between 6-12°N and descent to the south) extending from the lower troposphere to about 200 hPa, and a shallower cell with a return flow in the middle troposphere. Conversely, the meridional circulation in the central Pacific displays different characteristics with regions weak ascent on both sides of the Equator over the areas with the highest SST. The discriminating feature between the regions appears to be the existence of a strong CEPG in the east. On interannual time scales the position of the ITCZ varies with the phase of ENSO. During La Niña the location of deep convection shifts to a more northerly position, while during El Niño deep convection occurs closer to the equator. However, the general characteristics of the MMC are similar in both cases. On shorter time scales, ITCZ exhibits substantial variability on 4 - 8 days period in OLR, lower and mid-tropospheric meridional wind and relative vorticity. Of particular interest is the diagram of 600 hPa meridional wind amplitude in the 4-8 day band (Figure 3.13b). If the eastern Pacific westward propagating disturbances would be the result of large scale dynamics rather than propagating from the Atlantic one would expect the disturbances to occupy a region larger than the convective region. The 600 hPa meridional wind distribution

suggests that the 4-8 days ITCZ oscillations have a cross-equatorial large scale component. In this context, the dynamics and formation of easterly waves will be discussed in the next two sections.

CHAPTER IV

TRANSIENT STATES OF THE ITCZ

The analysis of the general characteristics of the east Pacific convective region (Chapter 3) has suggested the transients are a very important component of the mean ITCZ. To investigate the characteristic features of these transients, a composite analysis centered around days with strong negative OLR anomalies in the 4-8 day band was performed. A formation mechanism is proposed.

4.1 Character of the transients

Figure 4.1a-b shows a latitude-time plot of sections of OLR deviations from the long term JJA mean and the total 925 hPa absolute vorticity (η) averaged between 120°W-110°W and 180°W-170°W, respectively. Both sections show periods of enhanced (negative OLR values: blue) and reduced convection (positive OLR: red) with changes in sign occurring every few days. In the eastern section, convective activity is confined between 5°N and 20°N although there appears to be some evidence of related OLR variability in the southern hemisphere near 20°S. The convection in the western section appears less spatially confined and related to convective events occurring on either side of the equator. There are also distinct differences in the absolute vorticity fields. The eastern section shows that the absolute vorticity is generally anticyclonic south of about 5°N but with large excursions of the zero contour both to the north of 5°N and towards the equator.

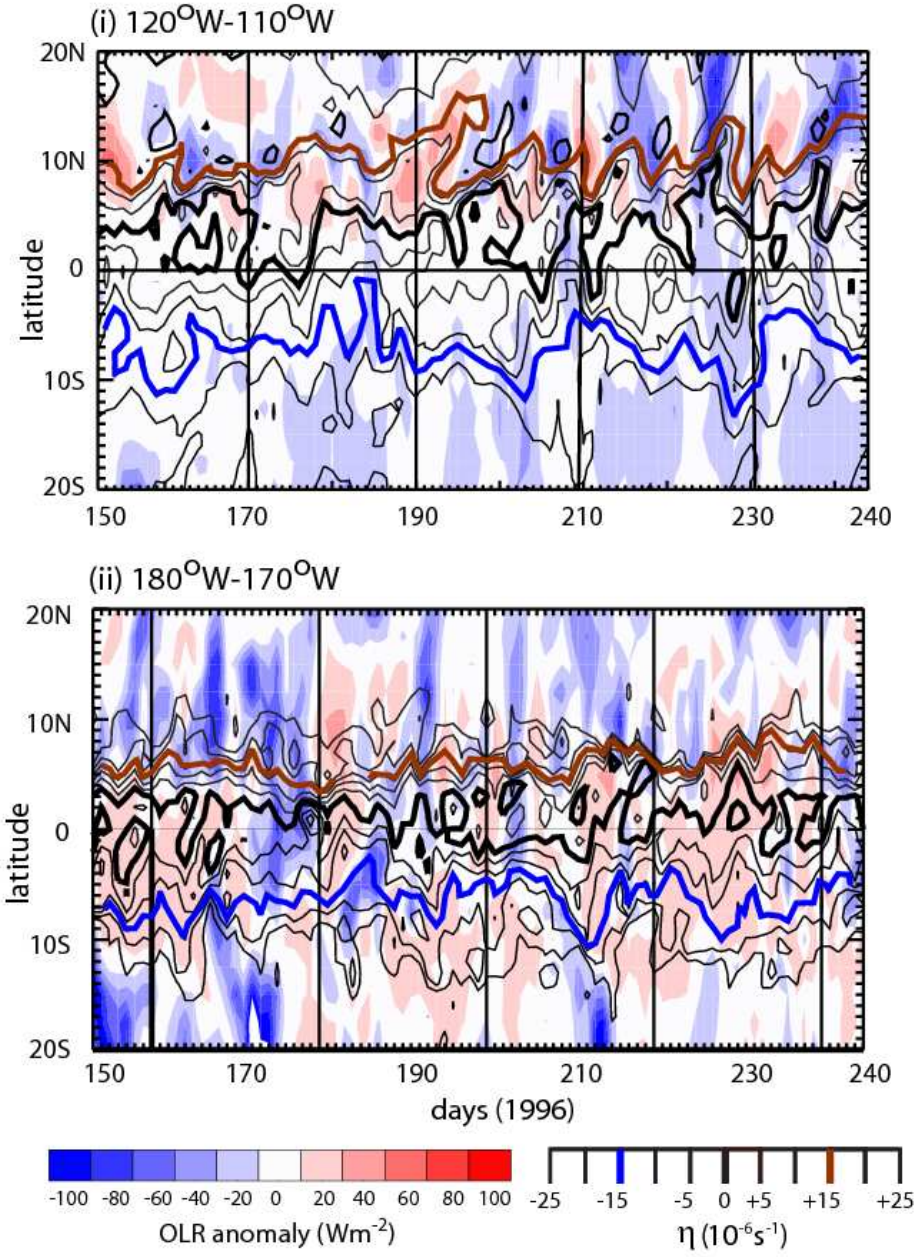

Figure 4.1: Evolution, as a function of latitude, of daily values of anomalous OLR (shaded, bottom scale: Wm^{-2}) and absolute vorticity (η: units 10^{-6} s^{-1}) at 925 hPa in the (i) 120°W-110°W longitude sector and (ii) 180°W-170°W for periods in the northern hemisphere summer of 1996. Commencing and ending dates in the sections are May 29 (day 150) and August 27 (day 240) for 1996. Contours intervals of η are every $5*10^{-6}$ s^{-1} between $\pm 25*10^{-6}$ s^{-1}. Bold contours, relative to bottom scale, show the η=+15, 0 and $-15*10^{-6}$ s^{-1} contours.

In the northern hemisphere, the northward extent of the $+15*10^{-6}$ s^{-1} contour also shows considerable variability. To the west, the variations of η are confined closer to the equator and appear less associated with variations of convective activity. The differences in distributions of the mean η during the summer of 1996 can be seen in Figure 1.3a-b. The "cross-hairs" in the center of the diagrams denote the latitude of the equator and the $\eta = 0$ magnitude. In the eastern section, there is anticyclonic vorticity in the mean extending to at least 5°N, considerably further poleward than in the west.

To examine further the associations between convection and absolute vorticity, we take advantage of the strong high-frequency spectral band apparent in the spectral analysis of OLR (Figure 3.11). Figure 4.2 shows a longitude-time section of OLR, similar to Figure 3.9, except for the 4-8 day period band. The filtered diagram shows strong westward propagation of negative OLR anomalies with magnitudes >-50 Wm^{-2} with wavelengths of approximately 20°-30° longitude or 2000-3000 km and propagation speeds of 8-10 ms^{-1} in the eastern Pacific although somewhat slower in the west) similar to those found in previous studies (e.g., Serra et al. 2008).

Figure 4.2 raises the important question of whether the Pacific disturbances are generated *in situ* or propagate across the Isthmus of Panama from the Atlantic Ocean. Between day 200 and day 220, the waves in the Pacific appear to have no corresponding perturbations to the east of the Isthmus. Between days 220 and 230, waves are evident on the east side of the Isthmus but they appear to arrive 2-3 days earlier than would be necessary to explain Pacific waves as resulting from simple propagation across the Isthmus. It is possible that a phase change occurs across the Isthmus but why that should occur is unknown. After day 230 there is little evidence of waves to the east of the

Isthmus although the region to the west is quite perturbed. Serra et al. (2008) note that some waves propagate from the Atlantic but found that most waves appeared to form in the eastern Pacific Ocean. The results presented here for 1996, are corroborated by similar analyses for other years in the data set (not shown), appear to confirm Serra et al's conclusion.

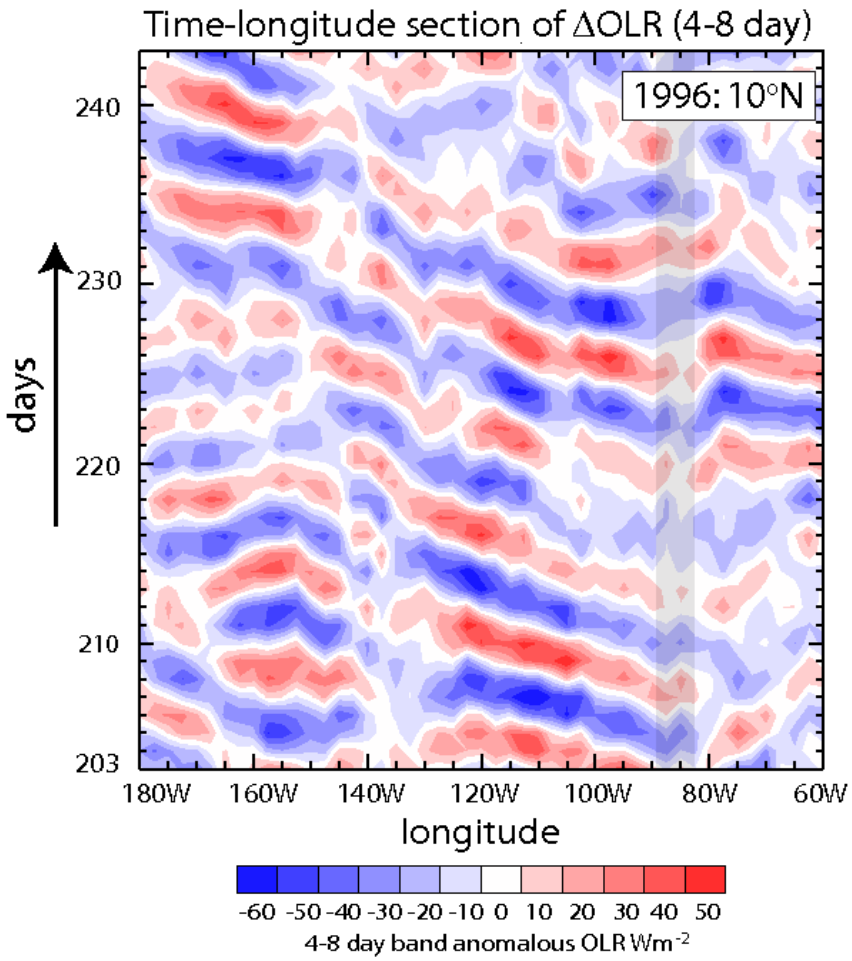

Figure 4.2: Time- longitude diagram of OLR anomalies (Wm^{-2}) in the eastern Pacific Ocean along 10°N between 180°W and 60°W. The 1981-2000 time period dataset has been filtered to emphasize the 4-8 day band period. Only days 203 to 243 of 1996 are presented.

Finally, the analysis shown in Figure 4.1 was repeated but for the 4-8 day period band in the same two longitude belts. The results are presented in Figure 4.3.

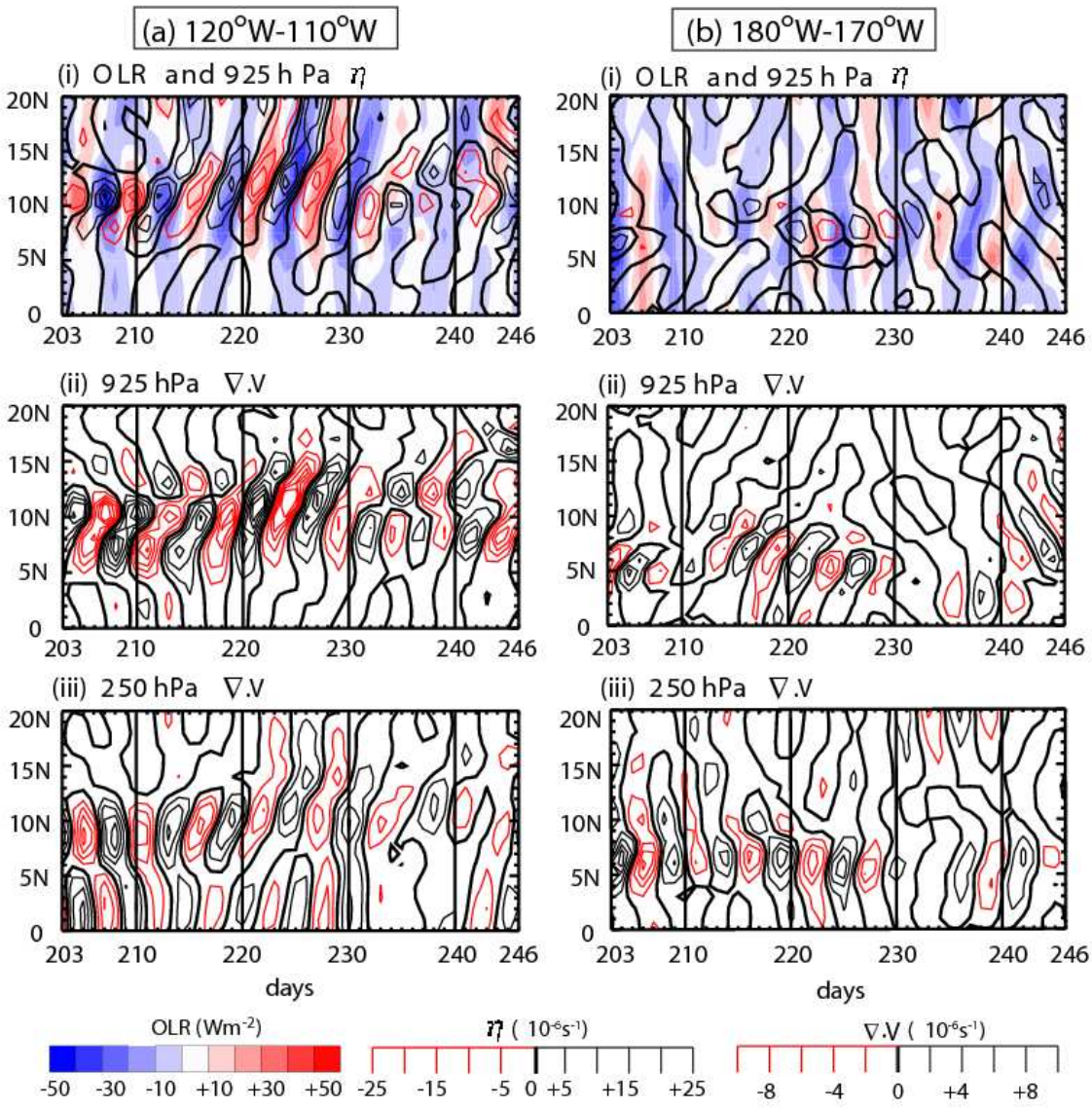

Figure 4.3: Time –latitude diagrams of the 4-8 day filtered data for a period during the 1996 summer between the equator and 20°N for two longitudinal bands (a) 120°W-110°W and (v) 180°W-170°W. Panels (i) show OLR anomalies (units: Wm^{-2}, shading lower scale) and anomalies in the absolute vorticity field ($\Delta\eta$, units: 10^{-6} s^{-1}, contours, lower scale). Bold black contour denotes $\Delta\eta=0$. Panels (ii) and (iii) show horizontal wind divergence at 925 and 250 hPa, respectively, relative to the contour scale at the bottom of figure (units: 10^{-6} s^{-1})

The uppermost panels show the band-passed OLR and 925 hPa η fields while the lower two panels show the band-passed horizontal wind divergence fields at 925 hPa and 250 hPa. In the eastern Pacific section (Figure 4.3a), OLR anomalies are negatively correlated with absolute vorticity and show an evident tendency for northward propagation culminating in convective extrema near 10°N. The low level divergence (panel ii) correlates negatively with convection and is out of phase, in general, with 250 hPa (panel iii). The distributions for the central Pacific section (Figure 4.3b) are dramatically different. The magnitudes of all of the fields are smaller than in the eastern Pacific. Little systematic association appears to occur between OLR and absolute vorticity. The upper and lower level divergence patterns are out of phase but occur nearer the equator and are less systematic than the patterns further to the east.

One could argue that the alternation of convection and vorticity is the result of the propagation of troughs and ridges past a point. But there is a complicating factor in this interpretation. There appears to be a coherent propagation from 5°N to latitudes poleward of 10°N. This will become clearer in Figure 4.4 which is discussed in the next section. Additionally, the modeling experiments presented in Chapter 5 confirm the propagation of these disturbances form the equator poleward.

4.2 Composite of the transients

Figure 4.3 suggests that there are two major extremes in the 4-8 day period band dominated successively by anticyclonic absolute vorticity anomalies ($\Delta\eta < 0$) and shallow convection (ΔOLR >> 0) or cyclonic absolute vorticity ($\Delta\eta > 0$) and deep convection (ΔOLR << 0) in the east Pacific section.

In order to study in detail the differences between these two extremes, a composite analysis is performed. Using this technique, only the most significant features of the disturbances are revealed. We construct the composites relative to a "day 0" defined by ΔOLR values in the 4-8 day band at 7.5°N being < -20 Wm^{-2}. Forty such cases were chosen from the 1981-2000 period defining composite day -3, -2, …+ 2, ,+3 states of the ITCZ between 30°S and 30°N, averaged between 120°W-110°W. In essence, the composite circulations may be thought of as the transient anomalies superimposed upon the long-term circulation shown in Figure 3.3b. Disturbances that attained tropical cyclone intensity were not included.

Figure 4.4 shows the latitude-height structure of the composite anomalies (4-8 day band) for the meridional circulation from day -3 to day +3. The left hand panels show the mass stream function (ψ) and relative humidity (RH %) while the right-hand panels show the meridional wind speed (v ms^{-1}: shaded lower scale) and horizontal wind divergence ($\nabla.V$, 10^{-6} s^{-1}, contours with zero line omitted). All quantities represent variability in the 4-8 day band. The first point to note is that changes in the circulations throughout the composite series occupy the entire latitudinal range between 30°S and 30°N so it reinforces, as suggested above, that the circulations are not merely signatures of waves propagating from the Atlantic Ocean.

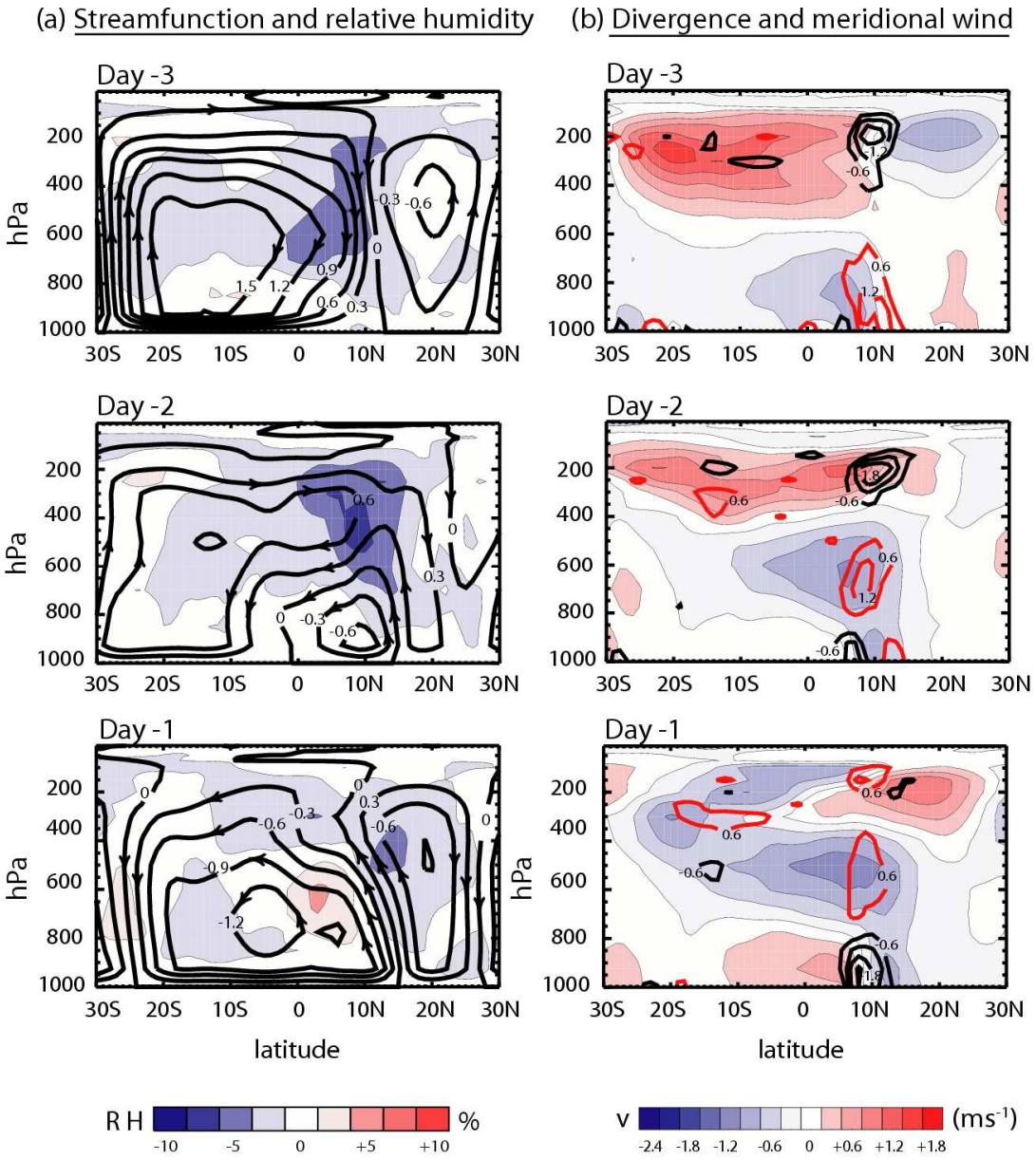

Figure 4.4: Composites of the height-latitude circulation between 30°S and 30°N averaged between 120°W and 110°W for day -3 to + 3 relative to the occurrence of maximum convection at 7°N. All diagrams are constructed from the 4-8 day band-passed fields. Day 0 of the composites are defined as days in which ΔOLR >-20 Wm^{-2} at 7°N in the 4-8 day band. 40 day 0's were so defined in the June-August period from 1981-2000. The figures follow the following format: the right-hand panels (a) showing the mass streamfunction (10^{11} kg s^{-1}) and the relative humidity (% shaded, bottom scale) and the left-hand panels (b) showing the meridional wind component (ms^{-1}, shading, bottom scale) and the horizontal divergence (10^{-6} s^{-1}). The zero divergence contour is omitted for clarity.

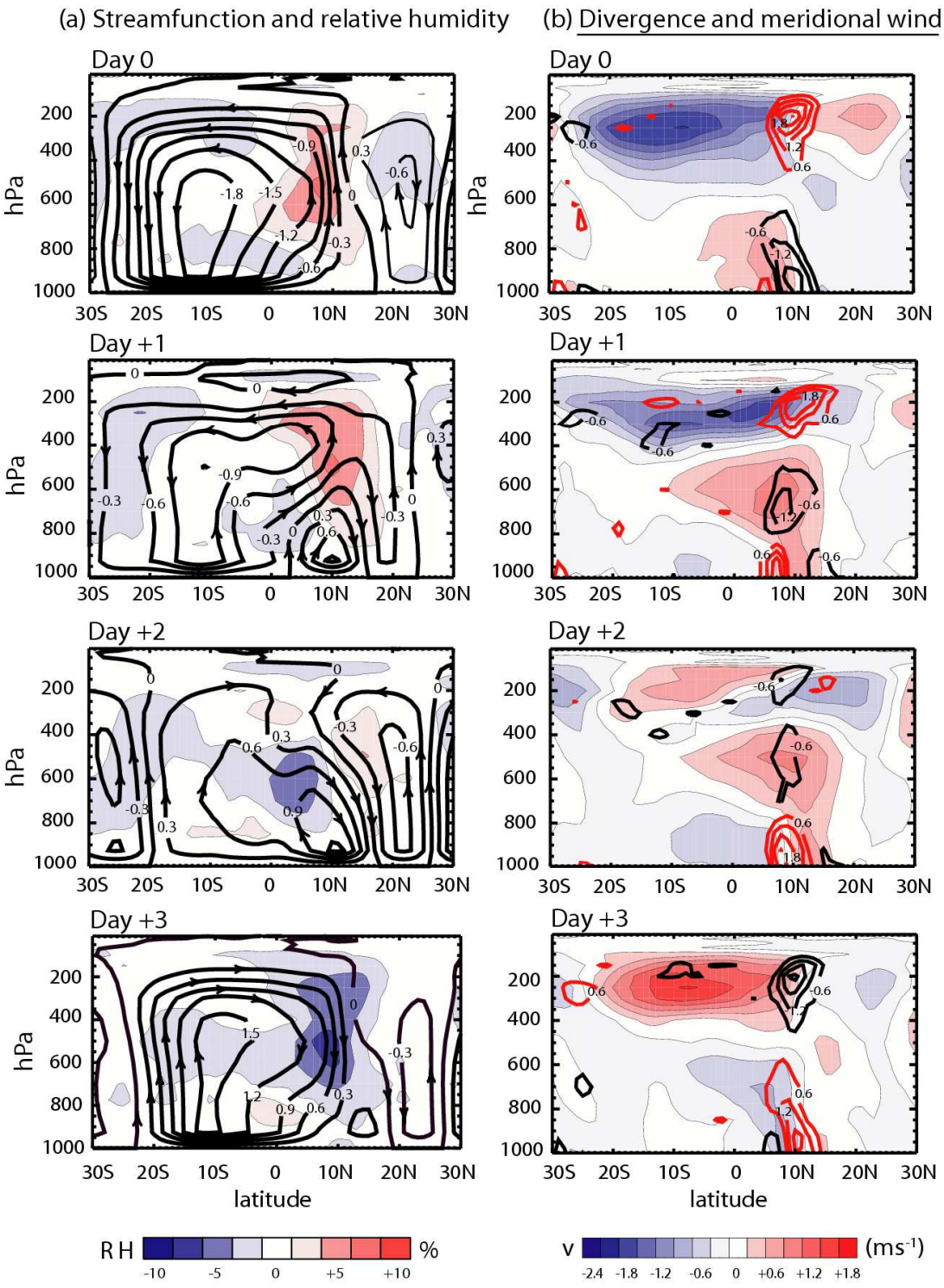

Figure 4.4: (cont)

The sequence may be described as follows:

Day -3: A broad meridional circulation extends from 30°S to 10°N with subsidence from 10°S to 10°N and boundary layer divergence near 10°N. The mid-tropospheric relative humidity north of the equator is negative. Upper tropospheric meridional winds converge near 10°N. Anomalous rising motion is apparent in the southern hemisphere and corresponds to the relatively negative anomalies in OLR (Figure 4.1a).

Day -2: A shallow cell has formed in the region between the equator and 15°N with weak rising motion to the north. Low tropospheric convergence exists to the south of 10°N. Convergence still exists in the upper troposphere but a region of lower-middle tropospheric divergence with a southward flow accompanies the development of the shallow cell.

Day -1: Large-scale changes have occurred between 30°N and 30°S. The shallow cell has extended into the upper troposphere although remnants of the shallow cell still exist with a weakened southerly flow and divergence in the middle troposphere. Relative humidity is increasing in the middle troposphere. Strong northerly cross-equatorial flow has developed producing strong convergence near 10° N. In the upper troposphere, the flow is becoming divergent and cross-equatorial northerly winds have developed.

Day 0: The OLR has reached its most negative and the anomalous absolute vorticity its most positive. The meridional circulation has increased in magnitude by nearly a factor of two and the relative humidity has increased considerably over the near equatorial northern hemisphere. The lower tropospheric shallow circulation has

disappeared entirely and tropospheric column to the north of the equator is dominated by strong low-level convergence and upper level divergence. The southward cross-equatorial upper-tropospheric flow has reached its strongest magnitude. The low level convergence, near 10°N, strongest at day -1, has weakened and a small region of divergence has developed near 6°N.

Day +1: The overall circulation has weakened by almost 50%. A shallow cell has developed accompanied by strong boundary layer divergence near 6°N and convergence near 700 hPa. A two-cell structure similar to Day -2, although reversed in sign, has developed.

Day +2: The shallow circulation has developed vertically and now occupies the entire troposphere producing subsidence and drying over the northern hemisphere tropics.

Day +3: The pattern returns to a similar state to that of Day-2.

The magnitudes of the band-passed filtered anomalies are about a factor of two smaller than the mean circulation mass streamfunction shown in Figure 3.3b. Superimposing the composite circulations on the mean state produces a meridional circulation that oscillates in intensity and produces a convective region that moves northward and southward over the 4-8 day time scale.

Figure 4.5 shows latitude-height distributions of the total circulation (mean plus anomaly) in terms of mass streamfunction and relative humidity (panels (i)) and meridional wind and divergence (panels (ii)) for composite days -2, 0 and +2. The dotted line represents the $\eta = 0$ contour. A similar sequence to the one observed in figure 4.4 is apparent.

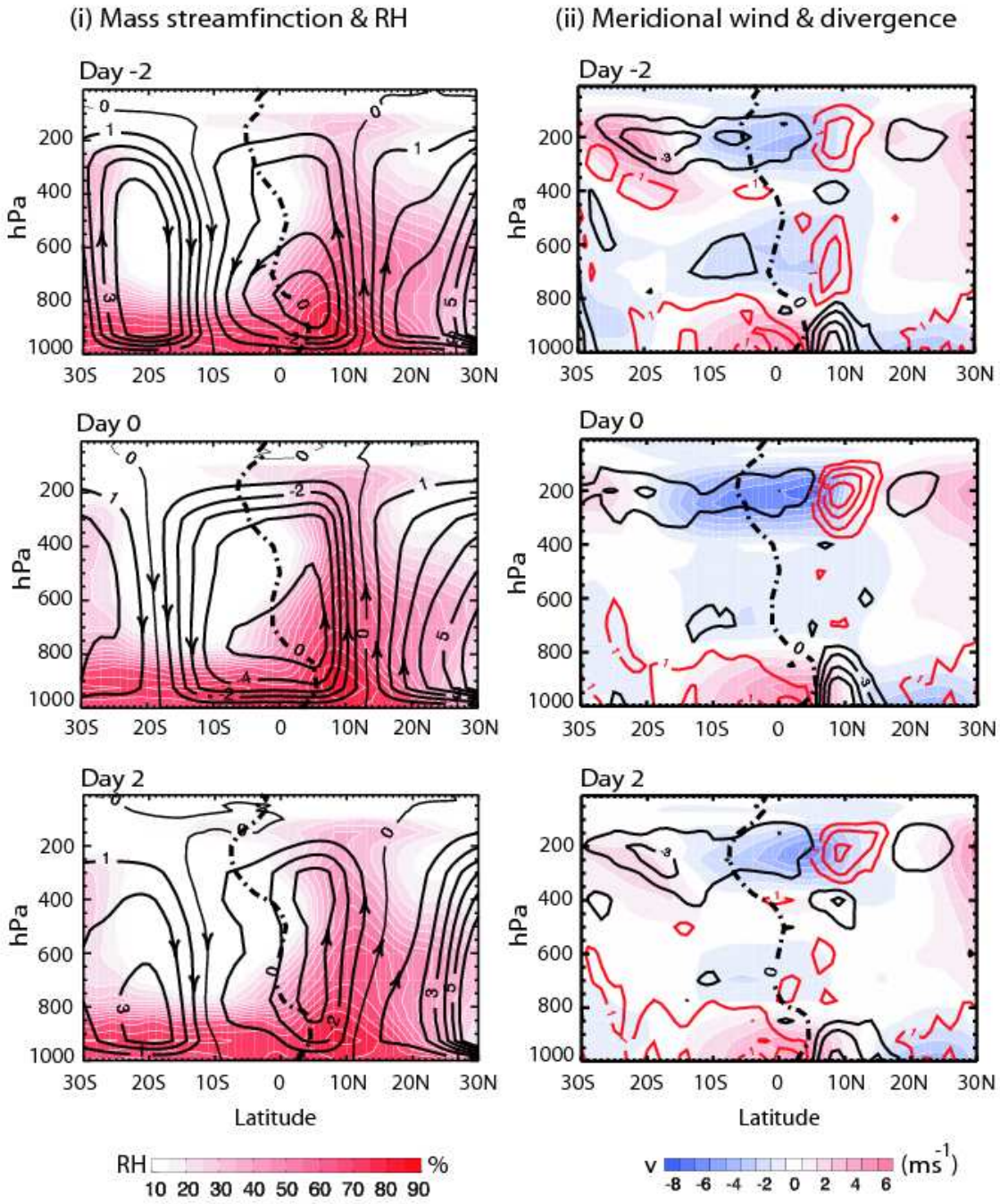

Figure 4.5: Similar format to Figure 4.4 except for the total composite fields. Only days -2, 0 and +2 are presented.

At day -2 the presence of the shallow meridional circulation is noticed, together with southerly return flow and horizontal wind divergence at mid-levels. At day 0, the deep meridional circulation has increased in magnitude compared to day -2, accompanied by strong low convergence and upper level divergence and increased values of mid - tropospheric relative humidity. The shallow cell has almost disappeared. By day +2, the meridional circulation has weakened and the low level convergence has reached its lowest value. Correspondingly, Figure 4.6 shows the latitude - height evolution of total heating rate (the material differential of potential temperature: $\dot{\theta}$) for composite days -2, 0 and +2. There is a significant difference in heating rates across the equator. Two dominant processes emerge: (a) radiative cooling accompanying the subsidence to the south and (b) latent heating due to deep convection at the latitude of mean ITCZ. At all times, the regions to the south of the η=0 contour (Figure 4.5) are drier and strongly subsident leading to efficient radiative cooling in the middle and low troposphere throughout the composite sequence (Figure 4.6). This cooling lies atop boundary layer heating from the ocean. Over the ocean cold tongue, between 4°S and the equator (see Figure 1.2b), there is a narrow band of boundary layer cooling consistent with increased evaporation and cooler SST. To the north of the η=0 contour, the vertical velocity is positive and moisture extends throughout the entire column (Figure 4.5). This is a region of intense latent heating associated with deep convection that oscillates throughout the composite cycle. There are large differences in heating rates from day -2 to day +2. For example, during maximum convective phase (day 0) the latent heating has increased from 6 K/day at day -2 to 12 K/day at day 0 at 500 hPa. The vertical heating structure evolves in a complicated fashion.

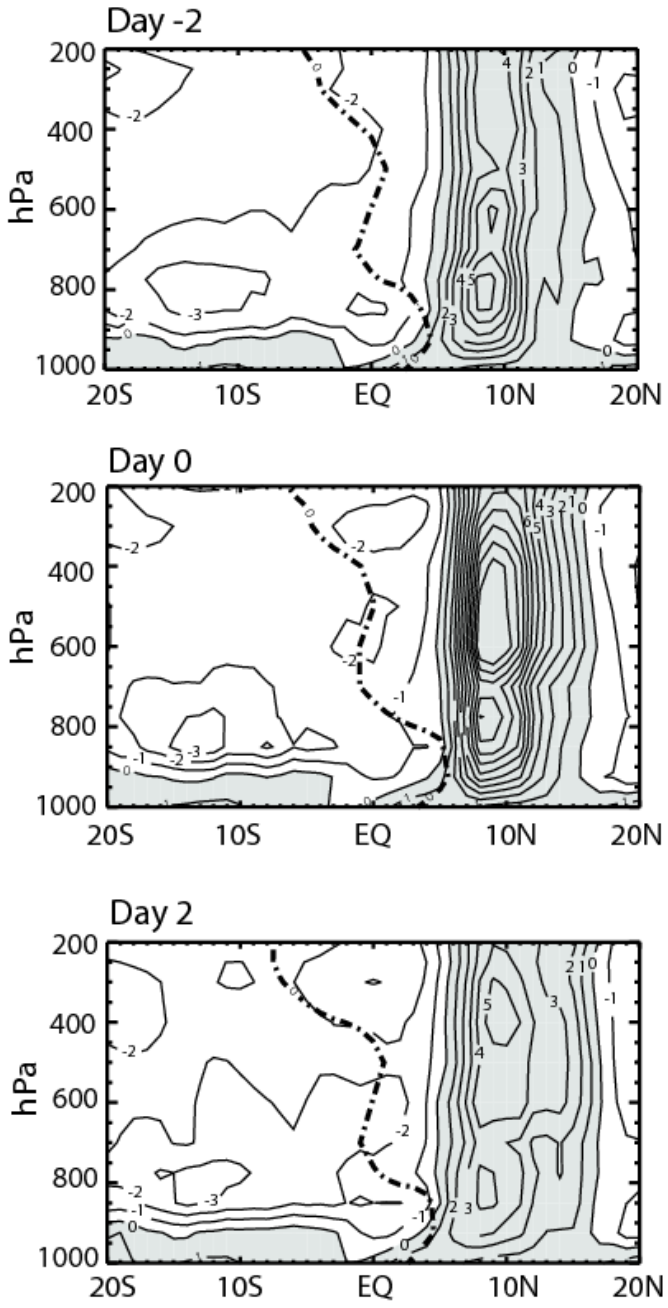

Figure 4.6: Similar to figure 4.5 except for the composite of material tendency of potential temperature $\dot{\theta}$(units: Kday^{-1}, contour interval: 1 KDay^{-1}, gray shading represent positive values). Only days -2, 0 and +2 are presented.

To examine this behavior, composite time-height distributions of total heating are shown in Figure 4.7 for the bands 10°S-8°S and 8°N-10°N for composite days -6 to +6. While

for the southern region (Figure 4.7a) there is no significant difference in the vertical heating profile from the day -6 to day +6, over the convective region (Figure 4.7b), the differences from day -2 (reduced convection) to day 0 (enhanced convection) are substantial. Prior to day 0, the heating is strongest in the lower and middle troposphere. As the convection intensifies, the heating expands upwards forming a new and stronger maximum in the middle upper troposphere. The lower maximum is contained and increases in magnitude but does not reach the size of the more elevated maximum.

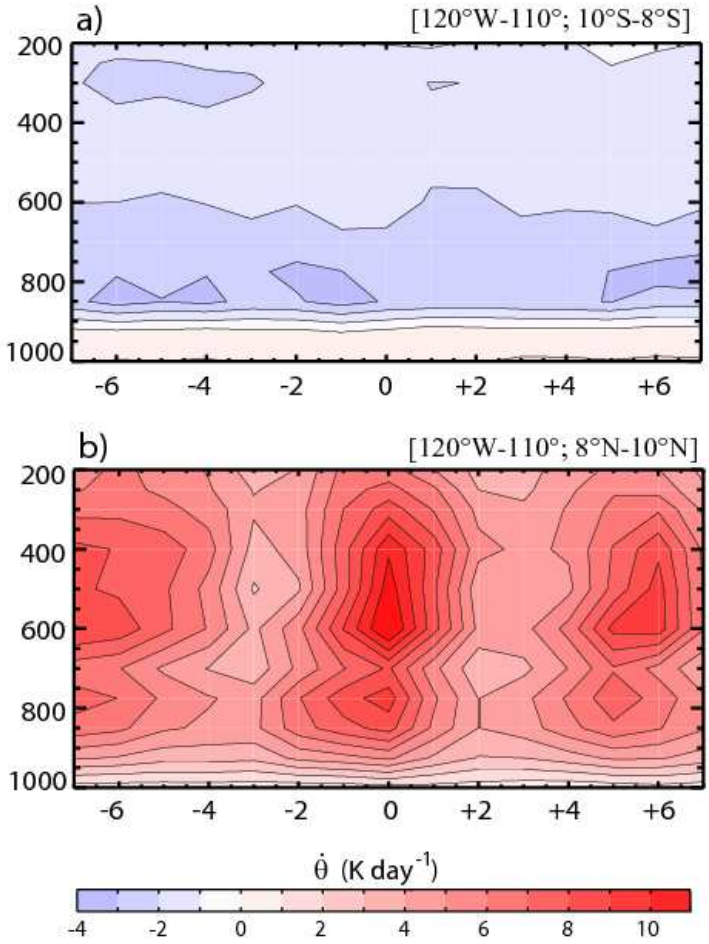

Figure 4.7: Composite day - height sequence of material tendency of the potential temperature $\dot{\theta}$(Kday^{-1}) for two regions [120°W-110°; 10°S-8°S] and [120°W-110°; 8°N-10°N], respectively.

In summary, the ITCZ appears to oscillate between a highly convective state (day 0) and a period of reduced convection (day -3 or +3). The shallow meridional circulation occurring on the transitional days -2 and +2 has many of the characteristics of the ZMB circulation. If this is the case, the double structure of the ZMB in the long-term mean occurs as a statistical artifact of the circulation in transition. This is in agreement with the result presented in figure 3.14b where the 600 hPa meridional wind oscillations in the 4-8 days band were extending from the convective region towards the equator. In the next subchapter an attempt to understand the dynamics of the ITCZ cycle described above is made.

4.3 Mechanism

It has been noted earlier that the magnitude of the CEPG, set up by the slowly varying SST distribution on each side of the equator, is the discriminating feature of the climate system determining the mean structure and the transients within it. The CEPG is a slowly varying quantity because the maximum and minimum SST centers occur poleward of the influence equatorial transients. For a finite and negative CEPG, anticyclonic vorticity is advected across the equator rendering the system inertially unstable (e.g., Stevens 1983, TW). To providing some qualitative understanding to the atmospheric response to the existence of locally anticyclonic absolute vorticity in the in the lower troposphere we will start by examining the linear condition for inertial instability in a purely zonal flow (e.g., Holton 1992, and Knox 2002):

$$f\left(f+\zeta_g\right)<0 \qquad (4.1)$$

where $\zeta_g = -\partial u_g / \partial y$ is the geostrophic relative vorticity and u_g the geostrophic zonal wind component. This condition can be written as:

$$f\left(f - \partial u_g / \partial y\right) < 0 \qquad (4.2)$$

and is exceeded in the northern hemisphere if there is anticyclonic shear ($\partial u_g / \partial y > 0$) and if $f < \partial u_g / \partial y$. From the above equations it is apparent that for zonal flows, inertial instability is expected to occur where the Coriolis parameter is small (i.e. near the equator) and $\partial u_g / \partial y > 0$. If the inertial instability condition $f < \partial u_g / \partial y$ is met, a parcel displaced poleward from its equilibrium position will be moving sub-geotropically (slower than the basic state) and will thus experience an acceleration in the direction of the displacement. In regions where the wind accelerates, divergence should appear, and regions where the wind decelerates should become convergent. The oscillation period of an inertial flow defined as $\frac{2\pi}{\left[f\left(f+\zeta_g\right)\right]^{1/2}}$ is about 4 days at 7°N and about 3 days at 10°N. Figure 4.8 shows the average frequency of daily instability occurrences in the lower troposphere for both boreal winter and boreal simmer. For each day grid points that satisfy the linear criterion for inertial instability (Equation 4.1) are identified. The monthly maps show the percentage of days in each month that satisfy this criterion.

Generally, the highest frequencies appear near the equator in the summer hemisphere with the exception of the Atlantic and Pacific oceans. In these two regions, the largest occurrences of inertial instability frequencies are in the Northern hemisphere thought the year. If inertial instability determines the latitudinal location of the mean ITCZ, then the transients should occur on time scales similar to local inertial frequencies.

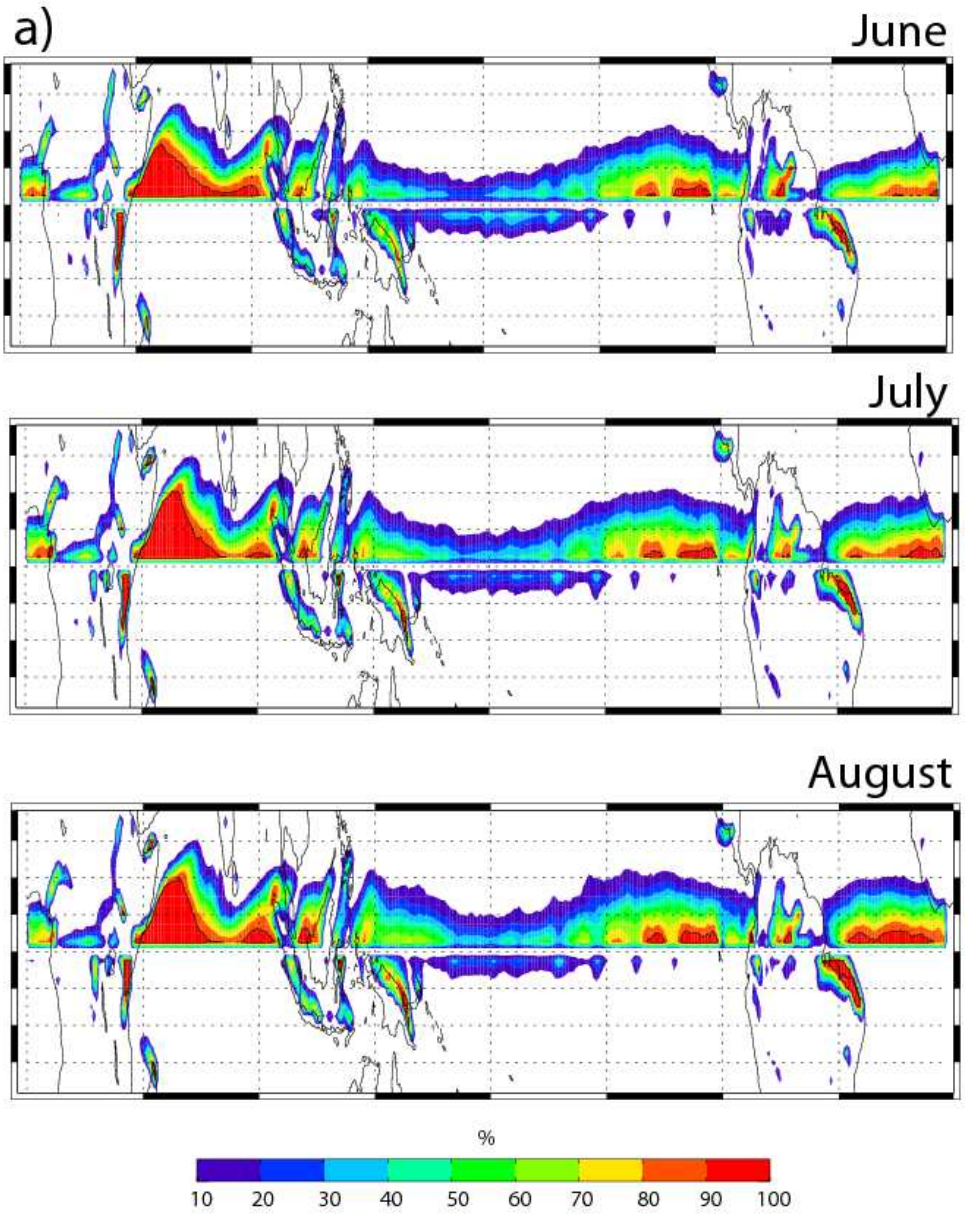

Figure 4.8: Monthly long term averaged frequency of daily inertial instability occurrence at 925 hPa for the 1981-2000 time period, for (a) June to August and (b) December to February. The black line shows the 90 % frequency level.

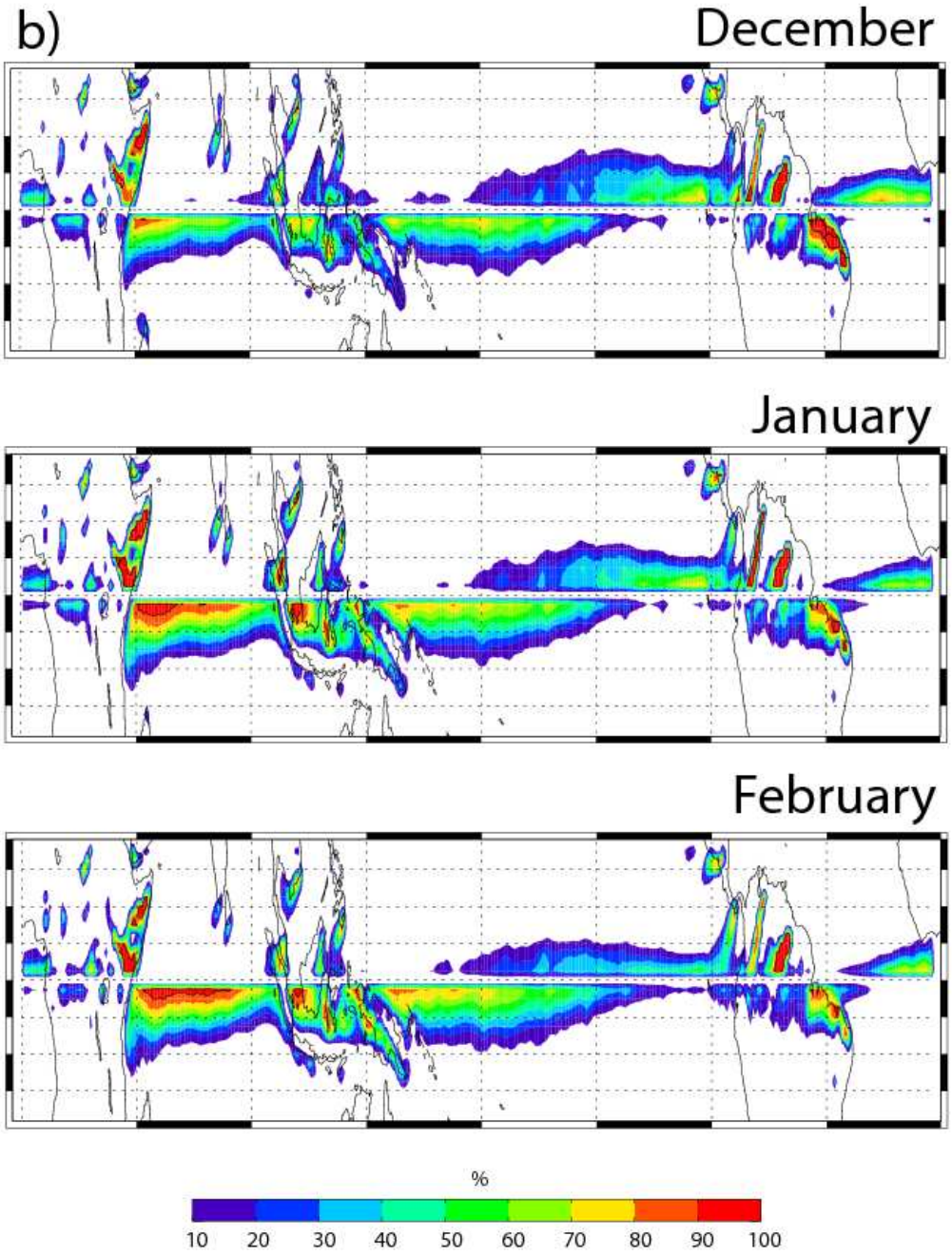

Figure 4.8: (Cont)

Comparing Figure 3.2 to Figure 4.8 it can be noticed that most of the convection in the Eastern Pacific Ocean is located poleward of regions with the highest frequency of inertial instability events. As presented earlier, the east Pacific ITCZ exhibits high

frequency variability that matches the inertial frequencies of the latitude range assumed by $\eta = 0$.

THW noted that, although the circulation signatures appeared to be in agreement with what should be expected in an inertially unstable regime, the linear stability criteria (i.e. an unstable solution for the ageostrophic meridional wind) could only be satisfied in an environment with a cross-equatorial shear far greater than observed. We examine the assumption of THW. In regions where the atmosphere is inertially unstable, the meridional wind accelerates poleward resulting in a divergence-convergence pattern, with divergence equatorward of the zero absolute vorticity line and convergence on the poleward side of η=0 line. However, the effect of the low level horizontal convergence on the vertical motion depends on the static stability of the atmosphere. In coming to their conclusions THW assumed a well-mixed boundary layer model topped by a temperature inversion ($\delta\theta = 3°K$) at an altitude of 1-2 km and concluded that the observed zonal wind shear was several time smaller than the shear required to meet the linear instability criterion. To expand this further, we start with their complete set of model equations linearized about a basic state $\overline{u}$ (described in their section 3):

$$\frac{\partial u'}{dt} + v'\left(\frac{\partial \overline{u}}{dy} - \beta y\right) + \alpha u' = 0 \tag{4.3}$$

$$\frac{\partial v'}{dt} + \beta y u' + \frac{\partial \Phi'}{dy} + \alpha v' = 0 \tag{4.4}$$

$$\frac{\partial \Phi'}{dt} + C_B^2 \frac{\partial v'}{\partial y} = - \in \Phi' \tag{4.5}$$

where u' and v' represent zonal and meridional wind perturbations, $\beta = df/dy$ is the meridional gradient of the Coriolis parameter, α is a linear damping coefficient,

Φ' represent the perturbation geopotential, and ϵ^{-1} is the boundary layer relaxation time. The parameter C_B is given by: $C_B = \left(gH_B \, \delta\theta / \theta_0 \right)^{1/2}$, where g is the gravitational acceleration, H_B the mean boundary layer depth, $\delta\theta$ is potential temperature jump at the top of the boundary layer, and θ_0 is the reference state potential temperature.

If a constant mean shear is assumed (e.g., Dunkerton 1981), then $\bar{u} = \gamma \cdot y$, where γ is a proportionality constant, and eliminating u' and Φ' from equations (4.3) - (4.5) we obtain:

$$\left(\frac{\partial}{dt} + \alpha \right)^2 v' + \left[\beta y (\beta y - \lambda) \right] v' - C_B^2 \frac{\partial^2 v'}{\partial y} = 0 \qquad (4.6)$$

Assuming an exponential form for v': $(v'(y,t) = V(y)e^{i\omega t})$, a solution with the form $V(\nu) = V_0 \exp\left(-\frac{\nu^2}{2} \right)$ has been found, where $\nu = \left(\beta / C_B \right)^{1/2} y'$.

In this case the eigenvalue is given by:

$$(\omega - i\alpha)^2 + \frac{\gamma^2}{4} = \beta C_B \qquad (4.7)$$

Equation 4.7 shows that instability (i.e. ω is imaginary) occurs only if the linear shear of the zonal wind (γ) is greater than a critical value: $\gamma^2 > 4 \cdot \beta \cdot C_B$. They calculated that for H_B ~1 km and a potential temperature jump $(\delta\theta)$ of 3°K, for instability to occur, the flow speed must increase by more than 30 ms^{-1} over 10° latitude. However, for much smaller values of potential temperature jump $(\delta\theta)$ (i.e. no cap at the top of the boundary layer) instability can occur for much smaller shear (γ) of the zonal wind. This is the case for

the eastern Pacific Ocean. Figure 4.9 shows the vertical profile of potential temperature and equivalent potential temperature using atmospheric soundings from the NOAA Research Ship *Ron Brown* cruise (thick line). Analyses at 1800 UTC (or very close to actual flight time) are presented for 1°S, 2°N, 5°N, and 8°N. The character of the atmospheric boundary layer changes from equator to the north, with very distinct profiles of potential temperature. While at 1°S and 2°N there is an apparent cap at the top of the atmospheric boundary layer ($\delta\theta = 3° - 6°K$), at 5°N and 8°N the atmosphere seems to be unstable (neutral) stratified and no cap at the top of the boundary layer is apparent.

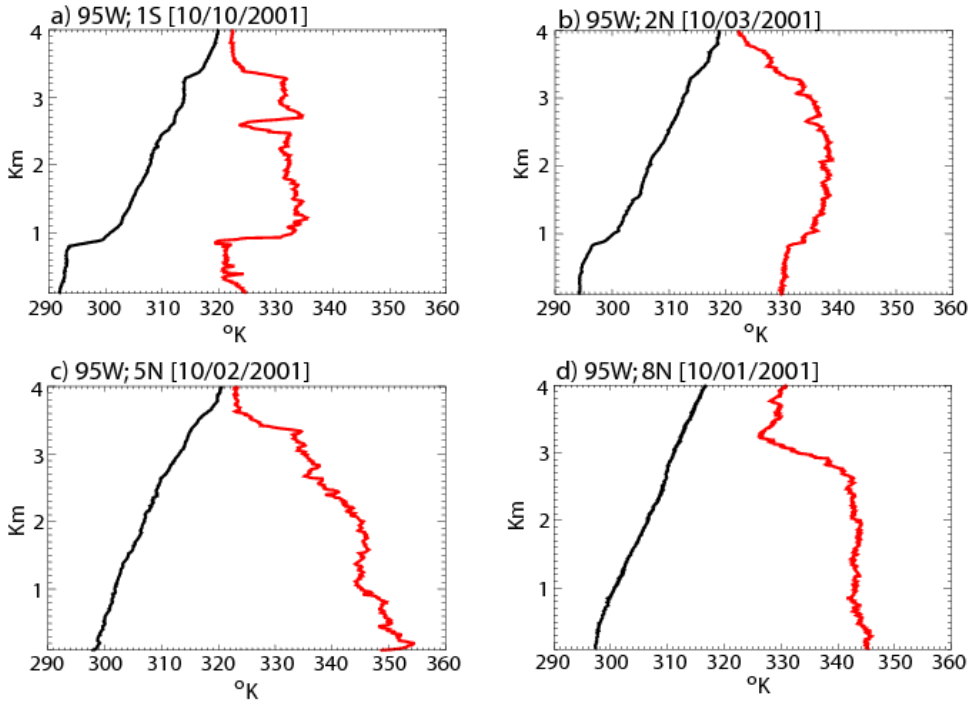

Figure 4.9: Magnitude –height profile of potential temperature (black) and equivalent potential temperature (red) for the eastern Pacific ITCZ during 1-3 October 2001 period using atmospheric soundings from the EPIC field campaign.

Moreover, when moisture is considered, it is apparent from both Figure 4.9c and d that the atmosphere in the convective region is conditionally unstable. Our results are in agreement with deSzoeke et al. (2005) findings (their results are averaged for the much

longer period of the EPIC campaign). Thus, contrary to THW findings, for observed values of $\delta\theta$, the linear criterion for inertial instability is met. If the CEPG is slowly varying, maintained by the large scale SST gradient, it may be expected that the convection under the action of a CEPG will be in a state of continual transience as an unstable state develops, relaxes and reestablishes once again. The manner in which this cycling takes place has been shown in Figure 4.4. An important question is, within this cycling, at what latitude will maximum convection occur. This latitude will define the position of the long-term mean ITCZ seen in Figure 3.2b.

4.3.1 Limits of the mean ITCZ

In Figure 1.3 it was noted that in the presence of a strong CEPG, the location of mean convection was to the equatorward side of the minimum MSLP or maximum SST. This may seem counterintuitive. For example, under just the action of the CEPG, one would expect convection to advance poleward until it coincided with the warmest SST and the minimum MSLP where convection would develop. Clearly, this is not the case and could be related to the local inertially unstable regime that accompanies a non-zero CEPG and the cross-equatorial advection of anticyclonic vorticity. Clearly, there must be a stabilization process that offsets the destabilizing advection. TW and THW argued that stabilization is produced by the generation of cyclonic vorticity through vortex tube stretching with the establishment of a secondary meridional circulation and the subsequent development of cyclonic vorticity in the lower troposphere. Given that the atmosphere is conditionally unstable, the meridional circulation extends rapidly through the troposphere with deep penetrative convection as seen between day -3 to day 0 in

Figure 4.4. With the generation of sufficient cyclonic vorticity, the region of absolute anticyclonic vorticity is diminished and the zero absolute vorticity line contour retreats towards the equator and convection weakens (days 1 to 3, Figure 4.4). However, still under the action of the slowly varying and large-scale CEPG, anticyclonic advection recommences and the cycle starts over again.

Starting with the absolute vorticity equation, we can determine the latitude of the northward extent of convection (the latitude of the mean ITCZ) under the action of a CEPG:

$$\partial \eta / \partial t = -V \cdot \nabla \eta - \eta \nabla \cdot V - \alpha \zeta \qquad (4.8)$$

where the local tendency of absolute vorticity is determined by a combination of absolute vorticity advection, vortex tube stretching and dissipation. The parameter α is a frictional dissipation coefficient. From (4.8), and starting with a state that is initially inertially stable ($\eta > 0$ to the north of the equator, $\eta < 0$ to the south) it is clear why cross-equatorial advection of absolute vorticity leads to regions of negative absolute vorticity (and inertial instability) to the north of the equator. The first two terms on the right-hand side of (4.8) are capable of making negative contributions. However, in the absence of cross-equatorial advection of absolute vorticity, they can only contribute to the generation of cyclonic vorticity in the northern hemisphere. The advection term can only redistribute cyclonic absolute vorticity and the vortex term contributes to a negative tendency if there were divergence.

When the advection term is non-zero, and the $\eta = 0$ contour resides to the north of the equator, it can be seen that strong divergence lies to the equatorward side of the $\eta = 0$ contour and convergence is located on the poleward side. Straddling the zero absolute

vorticity contour is the maximum meridional wind. These features were pointed out with reference to Figure 3.3b. There are two roles for this largely divergent meridional wind flowing down the large scale pressure gradient. On one hand, it is responsible for creating the conditions leading to inertial instability through the advection of anticyclonic vorticity across the equator. On the other hand, the acceleration of the meridional wind and the creation of the divergence-convergence pattern are instrumental in mitigating the effect of the instability. That is, to the north of the zero absolute vorticity contour, $\eta > 0$ and $\nabla \cdot V < 0$ so that the tendency is positive, generating cyclonic vorticity. On the equatorward side of $\eta = 0$, $\eta < 0$ and $\nabla \cdot V > 0$ so that cyclonic vorticity is also produced. Also, the generation of cyclonic vorticity is conducive to deep penetrative convection which forms on the poleward side of the $\eta = 0$. A manifestation of the generation of cyclonic vorticity is the withdrawal of the zero contour back towards the equator.

The northward limit of the $\eta = 0$, and subsequently the location of convection, can be estimated from the steady state form of the absolute vorticity:

$$-V \cdot \nabla \eta = \eta \nabla \cdot V + \alpha \zeta \tag{4.9}$$

where α is a frictional dissipation coefficient and the velocity V is determined by the pressure gradient force so that the stronger the CEPG, the greater the advection across the equator. However, as latitude increases, the advection term becomes dominated by the advection of planetary vorticity. i.e., with increasing latitude:

$$-V \cdot \nabla \eta \rightarrow -\beta v \tag{4.10}$$

where, $\beta = df / dy$ and v is meridional component of velocity forced by the CEPG where we note that $\beta \propto \cos\varphi$. As latitude increases, for a given divergence, the first term on the right-hand side of (4.9) also approaches an asymptotic limit:

$$\eta \nabla \cdot V \rightarrow f \nabla \cdot V \tag{4.11}$$

where we note that that $f \propto \sin\varphi$. Thus the first term on the right increases in efficiency as latitude increases whereas the term on the left-hand side decreases in efficiency. In broad terms, the limits of the unstable regime (and thus the near-equatorial convection) will occur where the generation of anticyclonic vorticity by advection is balanced by the production of cyclonic vorticity by divergence. Using (4.10) and (4.11) in (4.9) away from the equator, and ignoring dissipation we can search for the latitude, φ_e, where the two terms are equal. That is:

$$-\beta v = f \nabla \cdot V \tag{4.12}$$

Each term varies with latitude, the left-hand-side as $\cos\varphi$ and the right-hand-side as $\sin\varphi$. Given these opposite tendencies with latitude, there is only one latitude that will satisfy the equality (4.12) for a given meridional wind (and hence CEPG) and divergence. Essentially, by controlling the magnitude of the cross-equatorial divergent wind field, the CEPG will determine the latitude of ITCZ convection. Using (4.12) to solve for φ_e, the latitude of equilibrium, and noting that for small φ_e, $\tan\varphi_e \rightarrow \varphi_e$ we obtain:

$$\varphi_e \approx v / a \nabla \cdot V \tag{4.13}$$

where the divergent meridional wind is given by:

$$v = \frac{1}{\alpha}\left(\frac{1}{\rho}\frac{\partial p}{\partial y} - fu\right) \tag{4.14}$$

and $\partial p / \rho \partial y = \text{CEPG}$. Figure 4.10 shows the equilibrium latitudes as a function of divergent wind speed and divergence. Observed values of divergence and CEPG place the region of equilibrium between 8-10° from the equator in the eastern Pacific Ocean matching the location of maximum convection and the climatological ITCZ quite well.

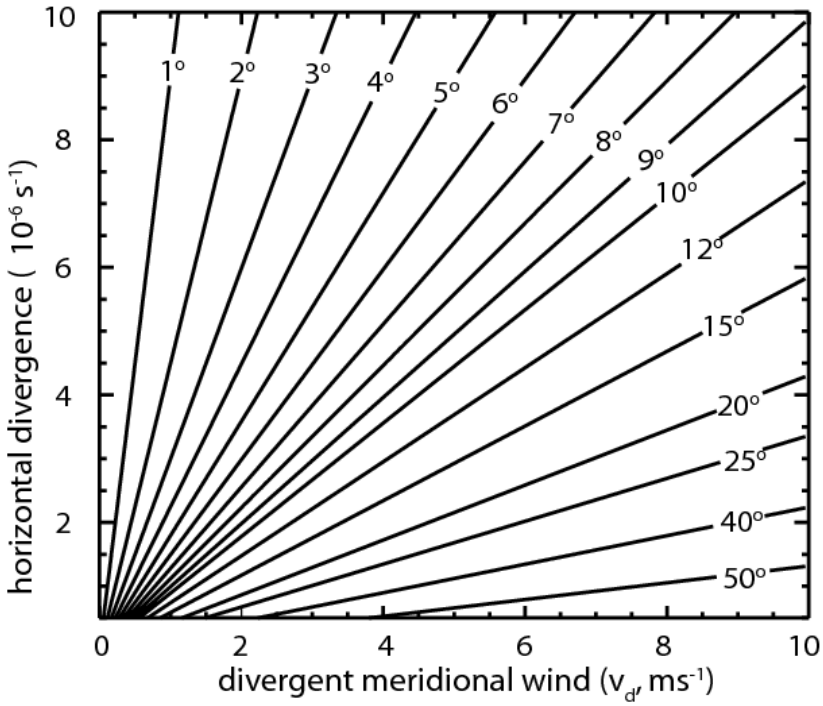

Figure 4.10: Isopleths of latitudes, where the advection of negative absolute vorticity equals the generation of cyclonic vorticity by vortex tube stretching. These latitudes are shown as a function of divergent meridional wind (v_d) or CEPG and divergence according to equation 4.13

THW used a nonlinear model to perform experiments to see if the observed structures could be simulated in a variety of CEPG environments. They found that the model reached a steady state in which there is a region of local anticyclonic absolute vorticity on the low-pressure side of the equator together with a divergence-convergence doublet. These simulations have the character observed by TW and which are evident in Figure 3.3b. THW also considered weak CEPG regimes such as occur in the central Pacific Ocean examined here in Figure 3.3a (Table 1.1). Lack of an ability to simulate the observed structure suggested that the boundary layer processes and instability arguments cannot determine the location of convection in regions of weak CEPG.

4.3.2 ITCZ transients

Figures 3.11, 4.1, 4.2, and 4.3 show that convection in the ITCZ region is highly transient. We now examine the dynamical balances that accompany these transitions relative to the terms of Equation 4.8). Figure 4.11 shows two transient cycles from Day -6 to Day +6 as a function of latitude from 5°S -20°N averaged between 120°W-110°W, calculated from the composites described earlier. All diagrams (except Figure 4.11a) show the 4-8 day composite anomalies. The evolution of the OLR (Wm^{-2}) and the 925 hPa absolute vorticity (10^{-6} s^{-1}) is shown in Figure 4.11a. The OLR oscillates between deep and shallower convection with the former occurring when the absolute vorticity is more cyclonic. This is seen more easily in Figure 4.11b where OLR and absolute vorticity in the 4-8 day band is plotted. The association is the same between OLR and vorticity as in Figure 4.11a except that there is clear poleward propagation from the equator. The 925 hPa meridional wind is shown in Figure 4.11c. The meridional wind anomalies also shows a cross-equatorial flux at least a day ahead of the OLR minimum anomalies near 10°N. The agent for the generation of convergence and divergence can be seen in Figure 4.11d with areas of growing convergence in regions of deepening convection. Finally, Figure 4.11e shows the evolution of the two terms of the vortex and divergence terms of the absolute vorticity Equation 4.8. In the region of maximum convection on Day 0, the two terms almost completely balance.

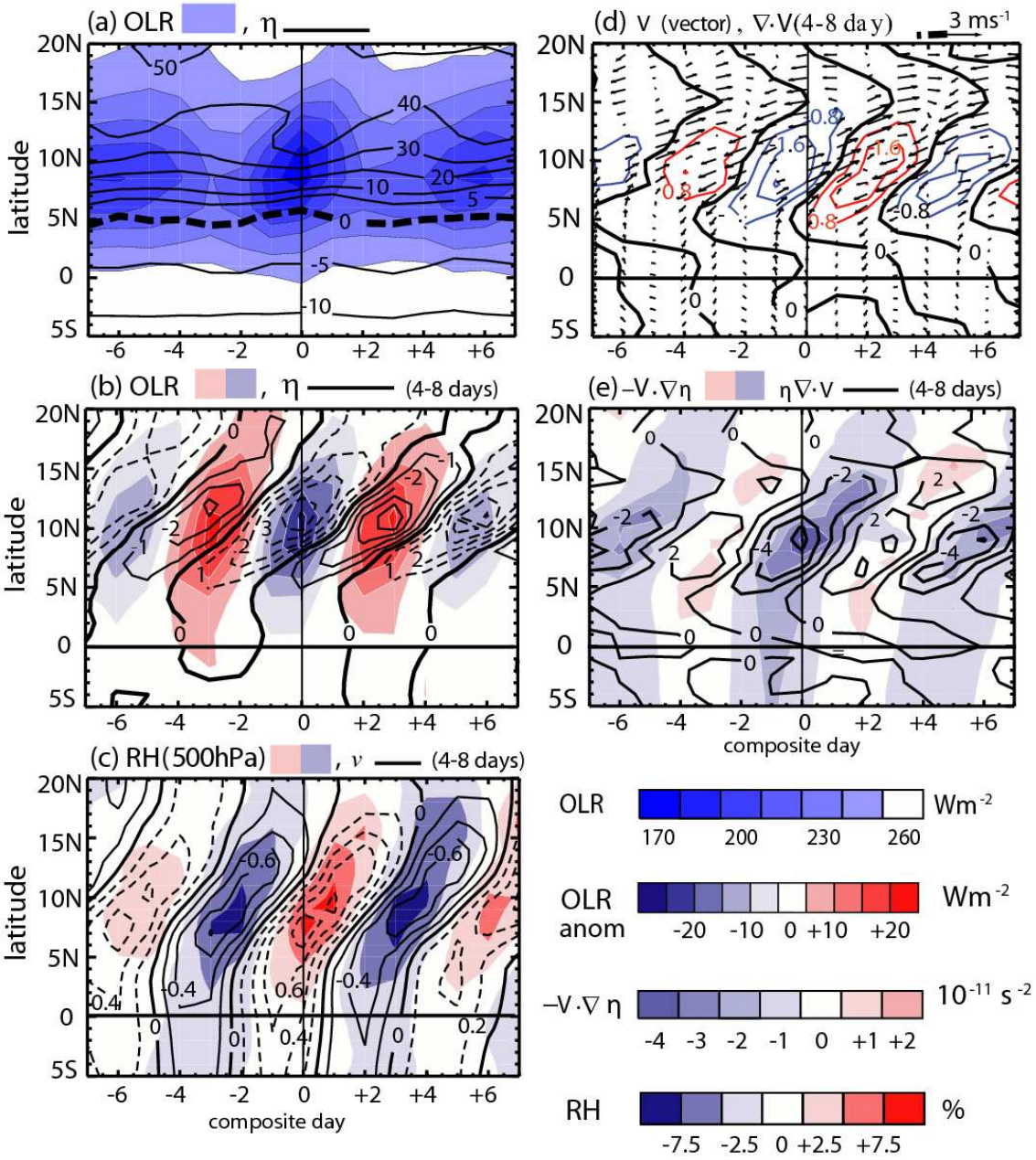

Figure 4.11: Dynamic balances between the transitions of the ITCZ oscillation between composite days -6 to +6: (a) Time-latitude sequence of the OLR (shaded, scale below: W m^{-2}) and the total absolute vorticity at 925 hPa ($\eta = \varsigma + f$: contours 10^{-6} s^{-1}): (b) The 925 hPa band-passed absolute vorticity and band-passed OLR (as in panel a); (c) The band-passed meridional wind v (contours ms^{-1}) and 500 hPa relative humidity (shaded, bar scale below); (d) The band-passed horizontal velocity vector V at 925 hPa (ms^{-1}, vectors) and 925hPa divergence ($\nabla.\tilde{V}$: contours: units 10^{-6} s^{-1}); and (d) Absolute vorticity advection ($-\tilde{V}.\nabla\eta$, shading, scale below, 10^{-11} s^{-2}) and vortex stretching term ($\eta\nabla.\tilde{V}$, contours, units 10^{-11} s^{-2}) from equation 4.8.

It has been shown that convection in the ITCZ region is highly transient. Composites of the disturbances were computed to describe the temporal evolution of the ITCZ. The composites showed that, in response to cross-equatorial advection of anticyclonic vorticity, buildup of low level convergence and generation of the cyclonic vorticity at the latitude of the mean ITCZ occurs. As cyclonic vorticity is generated, the η=0 contour moves back towards the equator. This process develops over a period of 3-6 days and it is accompanied by oscillations of the vertical heating in the ITCZ region between 6 $Kday^{-1}$ and 12 $Kday^{-1}$. The inertial frequency at the latitude of the mean ITCZ seems to determine the frequency of the oscillating latent heating. This "inertial oscillator" appears to be the result of a state of continued instability sustained by the CEPG. Additionally, the ZMB shallow circulation (Figure 3.3b) appears to be the result of averaging through the transition phases (i.e. day -2 and day -1 in Figure 4.4) before deep convection and it is representative of the growth of the stabilizing secondary circulation.

CHAPTER V

NUMERICAL EXPERIMENTS

The diagnostic studies presented in Chapter 4 have suggested that easterly waves are generated *in situ* in the eastern Pacific Ocean by an "inertial oscillator" of heating resulting from the existence of a finite CEPG. Some theoretical justification was given to this hypothesis. However, it is important that certain other possibilities for the existence of waves in the eastern Pacific Ocean be eliminated before the hypothesis can be substantiated. For example:

1. Are the easterly waves observed in the eastern Pacific Ocean the result of waves propagating across Central America from the Atlantic Ocean?
2. Does the elevated terrain of Central and South American promote the generation of easterly waves in the eastern Pacific Ocean?

To accomplish the consideration of these other hypotheses, we have designed a series of numerical experiments.

5.1 Model description

The Weather Research and Forecasting (WRF: version 2.2, Skamarock et al. 2005) regional model is used for the numerical experiments. The WRF is fully-compressible and uses high-order advection schemes on an Arakawa-C grid, with terrain-following hydrostatic-pressure vertical coordinate σ defined as: $\sigma = \left(p_h - p_{ht}\right)/\mu$, where $\mu = p_{hs} - p_{ht}$ and p_h is the hydrostatic component of the pressure, and p_t and p_s

represent the values at the top and surface values, respectively (Laprise 1992). The time integration scheme is the third-order Runge-Kutta described by Wicker and Skamarock (2002).

A spatial resolution of 56 km is used across the domain shown in Figure 5.1, with the southern boundary at 40°S, northern boundary at 40°N, western boundary at 155°W and eastern boundary 65°W. There are 28 vertical levels in the model with pressure p(top) at 50hPa. The WRF-Single-Moment class 5 micro-physics scheme (Hong et al. 2004) is chosen in addition to the long - wave radiation parameterization the Rapid Radiative Transfer Model scheme of Mlawer et al. (1997). The Dudhia (1989) short-wave radiation scheme is used. For the surface flux calculation the Monin-Obukhov scheme was used. The boundary layer scheme is the YSU scheme (Noh et al. 2003).

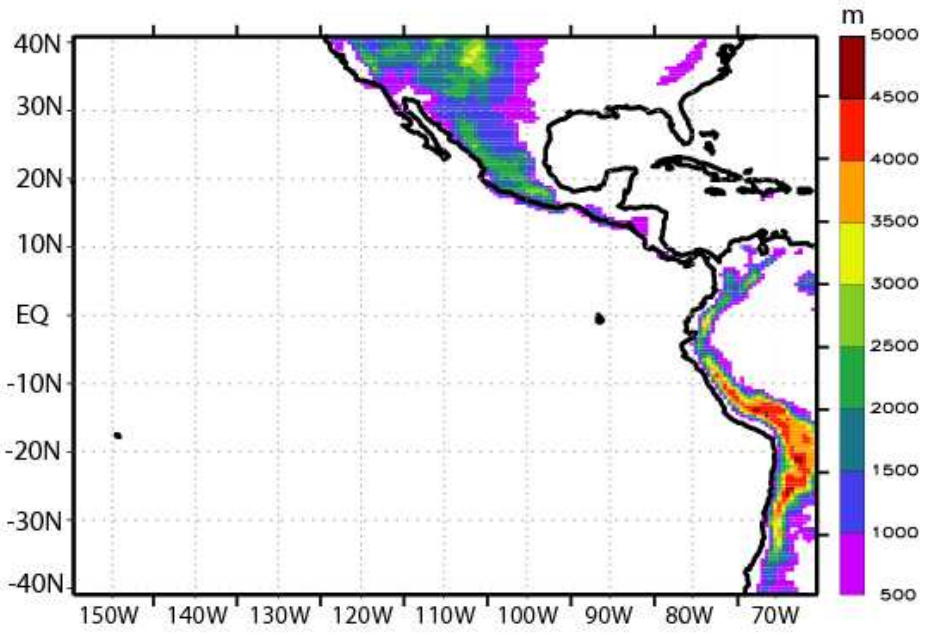

Figure 5.1: Physical domain and terrain height used in the control numerical simulations. Contour interval: 500 m.

For cumulus parameterization, the Kain-Fritsch (Kain and Fritsch 1993) and the Betts-Miller-Janjic (Betts and Miller 1993; Janjic 1994) schemes are used for different experiments. A detailed comparison of the simulations using the two cumulus schemes is presented next.

5.2 Experiments description and results

Several experiments were conducted. Initial data and boundary conditions in all simulations were obtained from the ECMWF (ERA40: Uppalla et al. 2005) dataset. The lateral boundary conditions were updated every 6 hours. A brief overview of the major differences between the experiments is presented in Table 5.1.

Table 5.1 Description of the differences between the lateral boundary conditions, SST forcing and cumulus parameterizations schemes used for the five cases.

	Initial Conditions and Lateral Boundary Conditions	Sea Surface Temperature	Cumulus Parameterization
Case 1	ERA 40 Reanalysis Updates every 6 hours	ERA 40 Reanalysis Updates every 6 hours	Kain-Fritsch
Case 2	ERA 40 Reanalysis Updates every 6 hours	ERA 40 Reanalysis Updates every 6 hours	Betts-Miller-Janjic
Case 3	10 day moving average of ERA 40 Reanalysis	Fixed to 12Z /01/06/2001	Betts-Miller-Janjic
Case 4	Monthly Mean of ERA 40 Reanalysis	Monthly Mean ERA 40 Reanalysis	Betts-Miller-Janjic
Case 5 **[Modified topography]**	Monthly Mean of ERA 40 Reanalysis	Monthly Mean ERA 40 Reanalysis	Betts-Miller-Janjic

It is important to emphasize that for all cases, the model is run in "free-mode" without updating with observations and, except for the SST forcing, the initial and lateral boundary condition, all meteorological fields are internally calculated within the model.

In all simulations the vertical motion was damped to prevent the model from becoming unstable with locally large vertical velocity. It was observed that, without the damping, too many strong convective cores were present. However, the comparison of the runs with and without damping (not shown) demonstrated that only strong updraft cores were affected, and the results were the same otherwise. All simulations were run for 121 days. The first 30 days are discarded for model spin-up purposes.

5.2.1 Control simulations

The first step in this study was to evaluate whether the proposed model set-up is suitable for our experiments. Since one of the objectives of this study is to examine the relationship between the cross-equatorial lower tropospheric flow in the Eastern Pacific and the easterly waves activity, the model simulated basic state needs to be compared with the observations. Two experiments were conducted for this purpose (Case 1 and 2 described in Table 5.1), both initialized at 12Z on June 1st 2001, with lateral boundary conditions and initial conditions for geopotential height, winds, temperature, moisture and sea level pressure updated every 6 hours. It is important to emphasize that the SST fields in the ECMWF ERA40 dataset are obtained from externally produced analysis of SST from United Kingdom Meteorological Office (Rayner et al. 2003) and NCEP NOAA/NCEP (Reynolds et al. 2002) with weekly temporal resolution that is linearly interpolated to 6 hourly values.

Two types of cumulus convection parameterization appeared as suitable candidates for the study: the Kain-Fritsch (KF) and Betts-Miller-Janjic (BMJ). A comparison of the results using the two schemes is presented next.

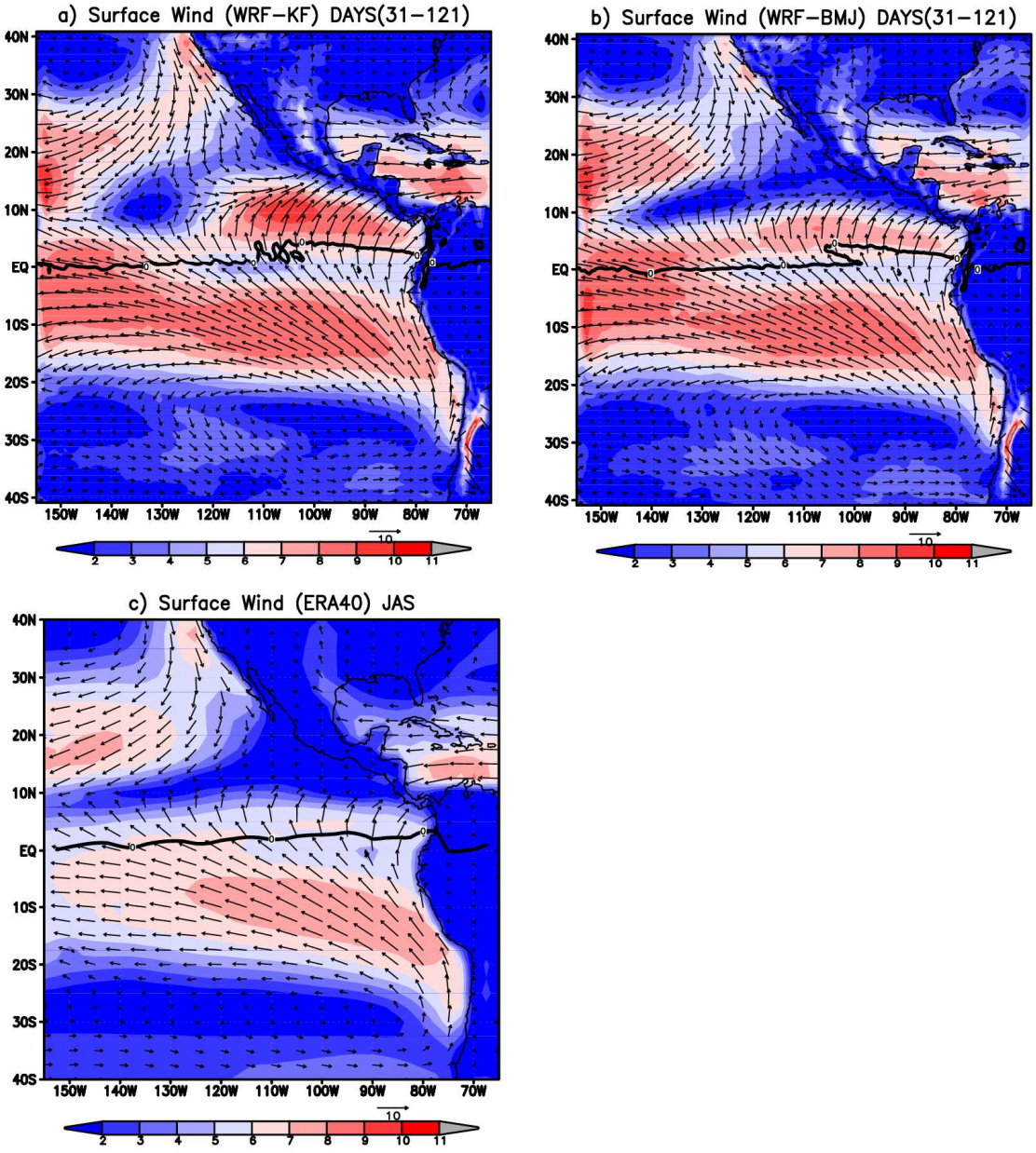

Figure 5.2: Mean distribution for days 31-121 of the 10 m wind direction and speed (units: ms^{-1}), for (a) Case 1, (b) Case 2 simulations and for (c) the long-term JAS ERA40 reanalysis mean (1981-2000). The thick black line represents the mean η=0 line at 10 meters.

Figure 5.2 shows the distribution of 10 m wind magnitude and direction for the model simulations (averaged for days 31 to 121), using KF cumulus parameterizations

scheme (Case 1) and BMJ scheme (Case 2) which can be compared to the long term mean (July-September) fields obtained from ERA40 (bottom panel). The thick black line represents the 10 m zero absolute vorticity isopleth. Although the overall surface cross-equatorial flow pattern is well reproduced in both model runs, the magnitude of the winds is generally stronger in the simulations compared to the climatology. One explanation for this could be the much longer averaging period for the reanalysis data set compared to our experiments averaging period. The model fields were averaged over one 90-days period compared to the multi-year long term average of the ERA-40. For a more thorough evaluation, an ensemble average of several simulations should have been computed and then compared with the long term ERA40 climatology. A distinct difference between Case 1 and the observations is apparent northward of the $\eta=0$ line between 120°W and 80°W. Here, the magnitude of the modeled wind field is much stronger that the climatology. The KF scheme seemed to produce a higher number of strong tropical cyclones than observed. The BMJ scheme, on the other hand, generates a more accurate description of the East Pacific surface winds. The $\eta=0$ line is situated north of the equator in both cases with maximum northward displacement located at about 100°W.

Figure 5.3 shows the distribution of precipitation for Cases 1 and 2, and long term mean July-September GPCP precipitation. The BMJ scheme appears to generate a more accurate description of observed spatial pattern of ITCZ rainfall then does the KF scheme. The GPCP JAS long term mean (1981-2000) monthly rate of precipitation was used to depict the observed fields. Maximum ITCZ convective activity for both WRF simulations and for observations is located approximately at 10-15°N although in Case 1

maximum convection is more aligned with the Central American continent than in Case 2 and in the observed fields. The smoother observed patterns, compared to the simulations probably comes from the differences in average period discussed earlier, and patterns probably arise from the differences in the spatial resolution: a 2.5° grid for GPCP versus 0.5° grid for the WRF simulations.

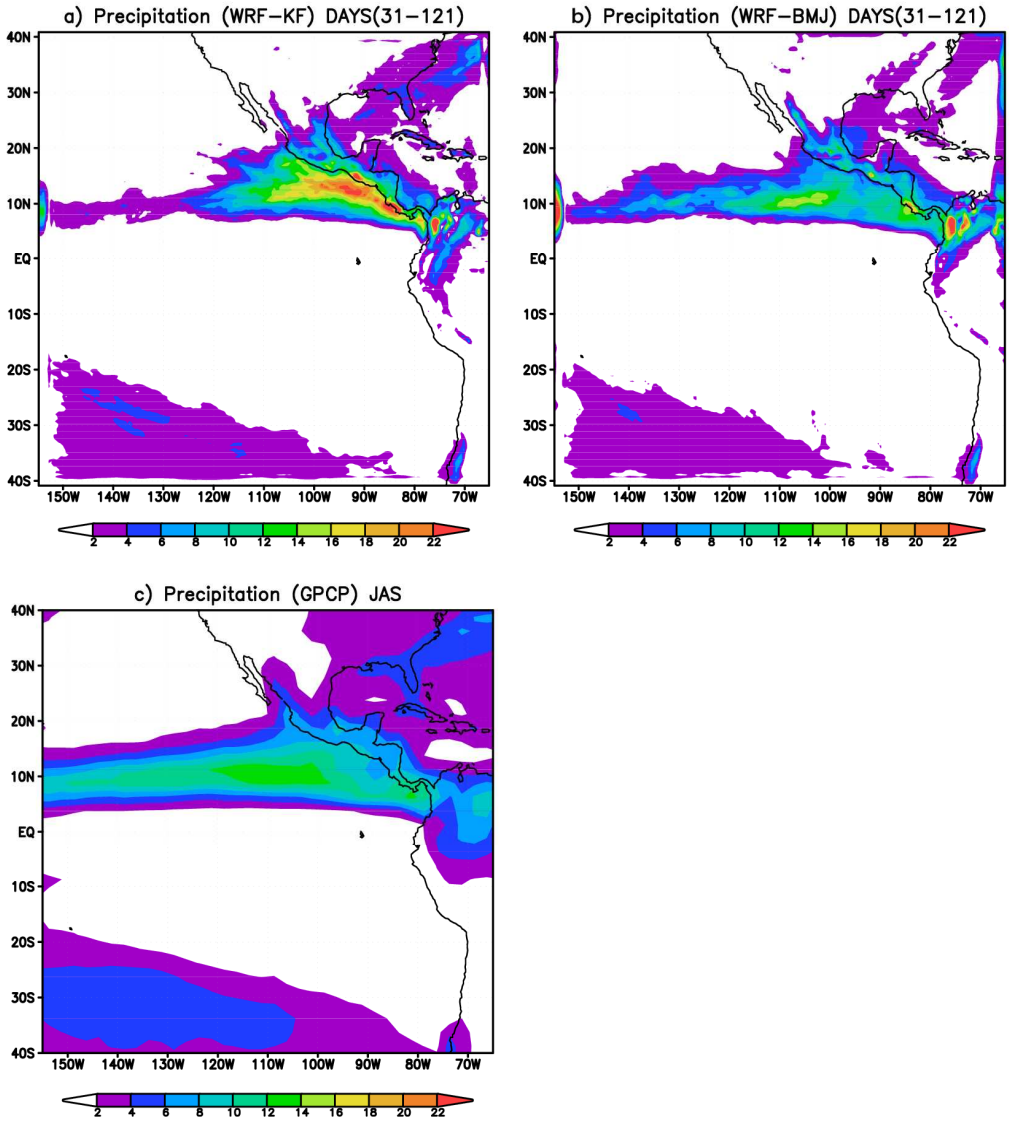

Figure 5.3: Mean distribution (days 31 to 121) of precipitation rates (units: mm day^{-1}) for (a) Case 1 WRF–KF, (b) Case 2 WRF-BMJ simulations, and for (c) JAS GPCP precipitation rate (units: mm day^{-1}) averaged for the 1981-2000 period.

The major characteristics of the mean meridional circulation as reproduced by Cases 1 and 2 are presented in Figure 5.4. At the surface, southerly winds > 6 ms^{-1}, with a maximum ~ 8 ms^{-1} occurring at 5°N in Case 1 is observed. The upper level return flow at 250hPa has speeds exceeding 12 ms^{-1} for Case 1 (Figure 5.4a) and 10 ms^{-1} for Case 2 (Figure 5.4b). Both experiments produce a mean meridional circulation pattern similar to observed east Pacific MMC (e.g., Figure 3.3b). In addition, similarly to the observations, a weaker secondary cross-equatorial northerly flow (with maximum of 2 ms^{-1} for Case 1, and 4 ms^{-1} for Case 2) occurs between 500 and 800 hPa. The zero absolute vorticity line ($\eta = 0$) in Figure 5.4 intersects the meridional wind maximum in the lower troposphere, and the boundary layer divergence-convergence doublet centered on the ($\eta = 0$) contour apparent in Figure 3.3b is well replicated.

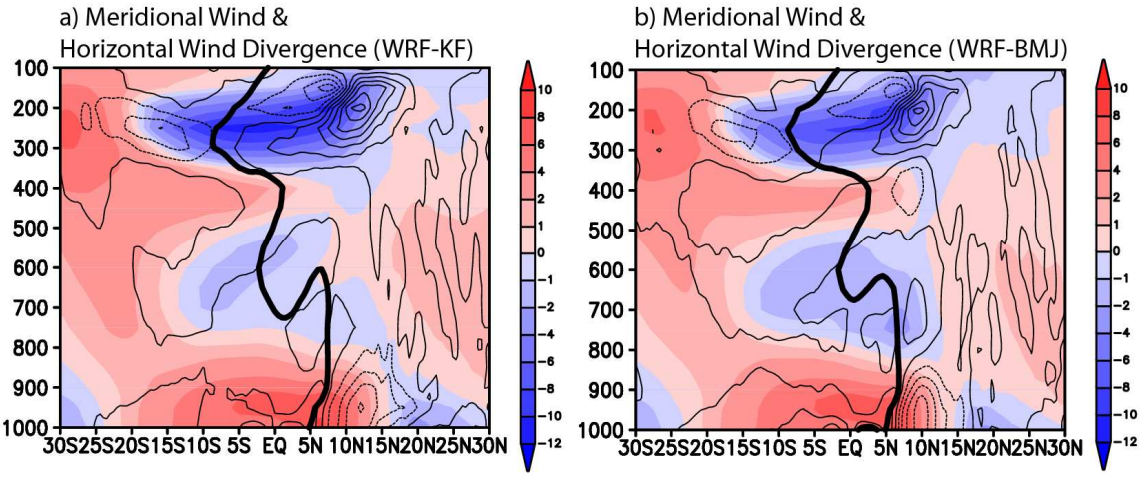

Figure 5.4: Characteristics of the simulated mean (days 31 to 121) meridional circulation in the east Pacific Ocean averaged for 120°W - 90°W. Panel (a) shows the meridional wind (shading relative to the bar on the right, units: ms^{-1}), horizontal wind divergence (contour interval: $3*10^{-6}$ s^{-1}, dotted lines represent negative values), the η=0 contour (thick black line) for Case 1 (KF simulation). Panel (b): same as (a) but for Case 2 (BMJ simulation).

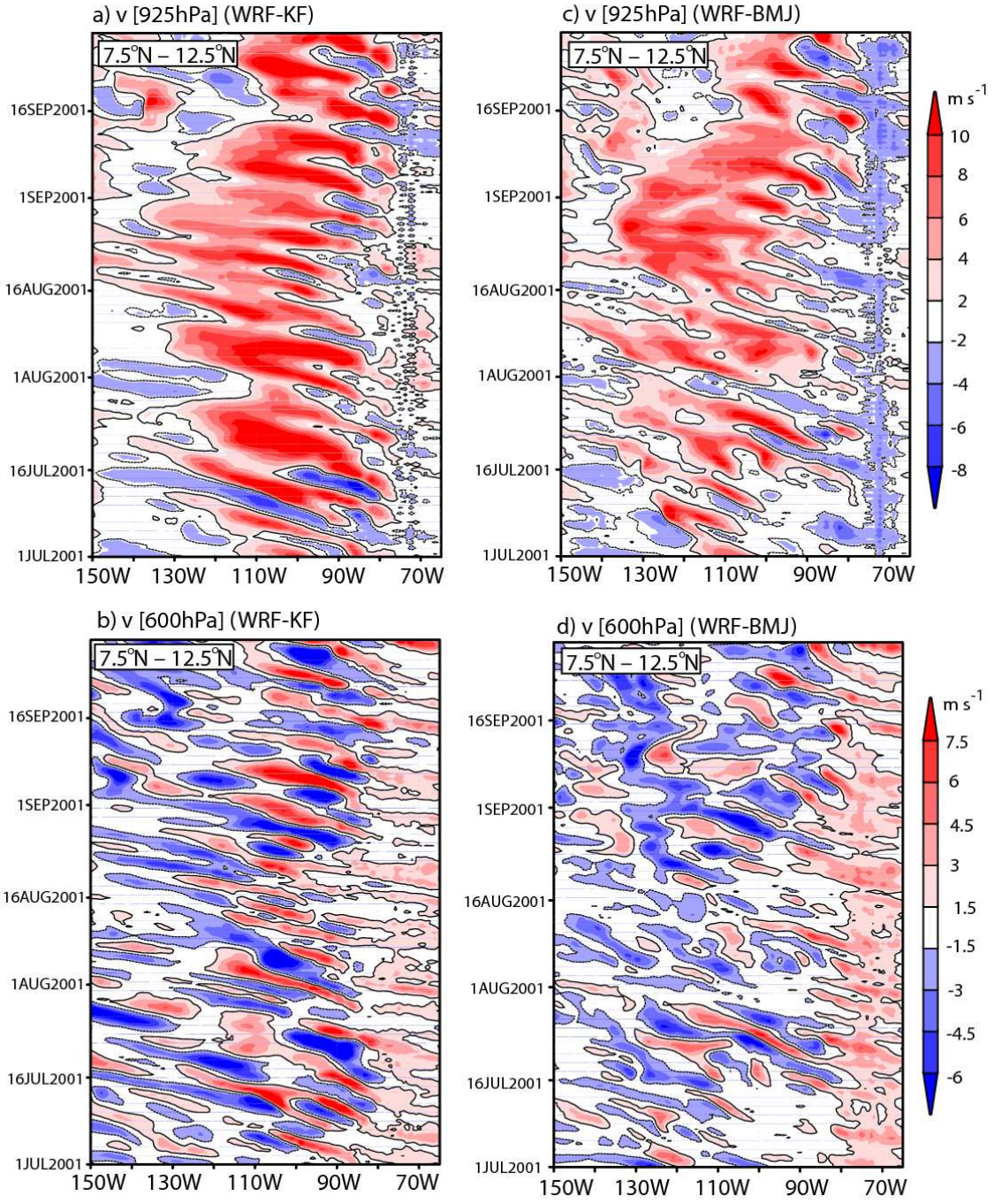

Figure 5.5: Time-longitude diagrams of meridional wind (shading relative to the bar on the right, units: ms^{-1}) at 925 hPa and 600 hPa for days 31 to 121 for Cases 1 and 2, between 150°W and 65°W averaged for the 7.5°N – 12.5°N band; (a) 925 hPa level - Case 1 KF, (b) 600 hPa level - Case 1 KF, (c) same as (a) but for Case 2 BMJ, and (d) same as (b) but for Case 2 BMJ.

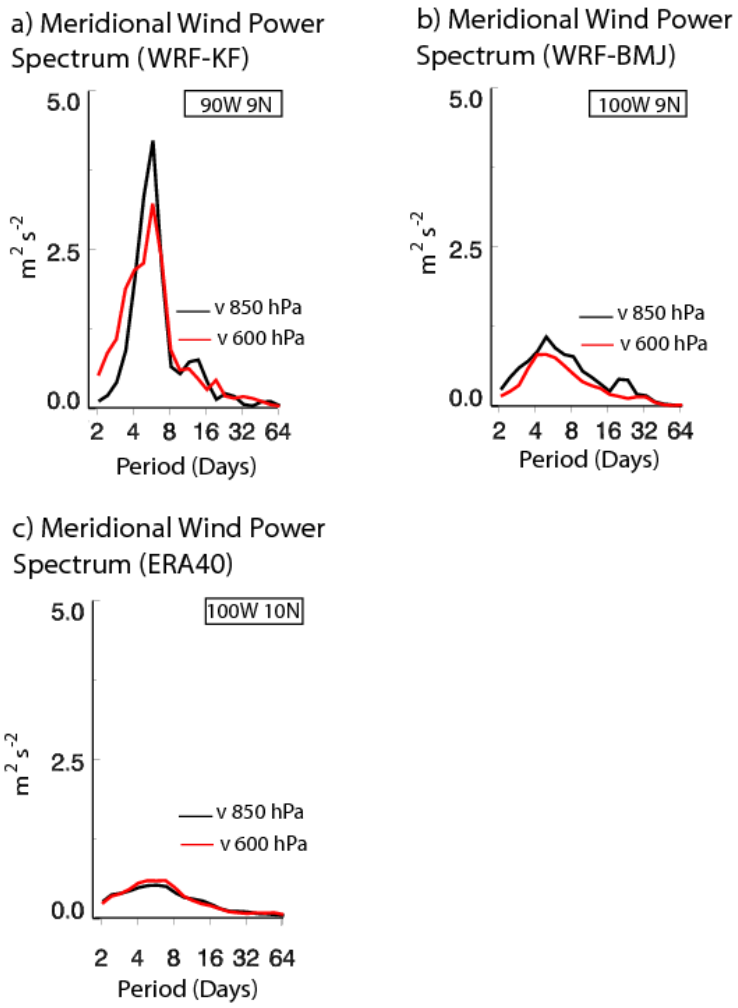

Figure 5.6: Global wavelet power spectra of meridional wind at two pressure levels: 850 and 600 hPa. Panel (a): Case 1 at 90°W; 9°N, panel (b): Case 2 at 100°W and 9°N and panel (c) ERA 40 Reanalysis at 100°W and 10°N.

Figure 5.5 shows the time – longitude evolution of unfiltered meridional wind (v) averaged between 7.5°N and 12.5°N at 925 hPa and 600 hPa levels over the domain for days 31-121 of Cases 1 and 2. The diagrams show westward propagating disturbances characterized by high frequency oscillations of meridional wind at both 925 hPa and 600 hPa levels. The wavelengths of these disturbances are approximately 2200-2500 km, with propagation speeds of 6-7 ms^{-1} and a period of 3-5 days. Figure 5.6 shows the power

spectra of meridional wind time series (days 31-121) for the 850 hPa and 600 hPa, for Cases 1 and 2 and the corresponding power spectrum of the observations for July-September 1981-2000. In both experiments a large peak in the 4-8 day band is apparent, although the amplitude in Case 2 is closer to the amplitude observed in the ERA40 dataset.

Since the BMJ cumulus parameterization scheme generates a more accurate description of the observed spatial pattern of ITCZ rainfall and the observed surface winds, only the results using the this scheme will be presented.

5.2.2 Experiments

To investigate whether easterly waves are produced in-situ in the east Pacific Ocean rather than being the remnants of waves propagating from the Atlantic Ocean, we filter out all disturbances entering the domain from the eastern boundary. Two additional experiments, labeled as Case 3 and 4 (see Table 5.1) are carried out for this purpose. The main differences between these experiment and the control runs are (a) the form of the lateral boundary conditions and (b) the SST forcing.

Figure 5.7 shows the difference between the zonal and meridional winds used as lateral boundary conditions for the control Case 2 (described in the previous subchapter) and the new Cases 3 and 4, respectively. For the control case, unfiltered data from the ERA 40 reanalysis data set were used for both initial and lateral boundary conditions. Case 3 uses smoothed initial conditions and lateral boundary conditions, obtained applying a 10-day moving average for each grid point. Subsequently, the resultant fields are linearly interpolated to produce 6-hourly values. By using this technique, all high

frequency transients were eliminated from the ERA-40 fields. To reduce the degrees of freedom in Case 3, the SST distribution was kept constant for the duration of the experiment. In Case 4, the lateral boundary conditions and the SST fields are obtained from a linear interpolation of monthly means values of the ERA-40. In this manner, only the influence of the seasonal cycle at the boundaries is present, and all other higher frequencies are eliminated. In all cases, the smoothing was conducted at all levels for all variables throughout the domain.

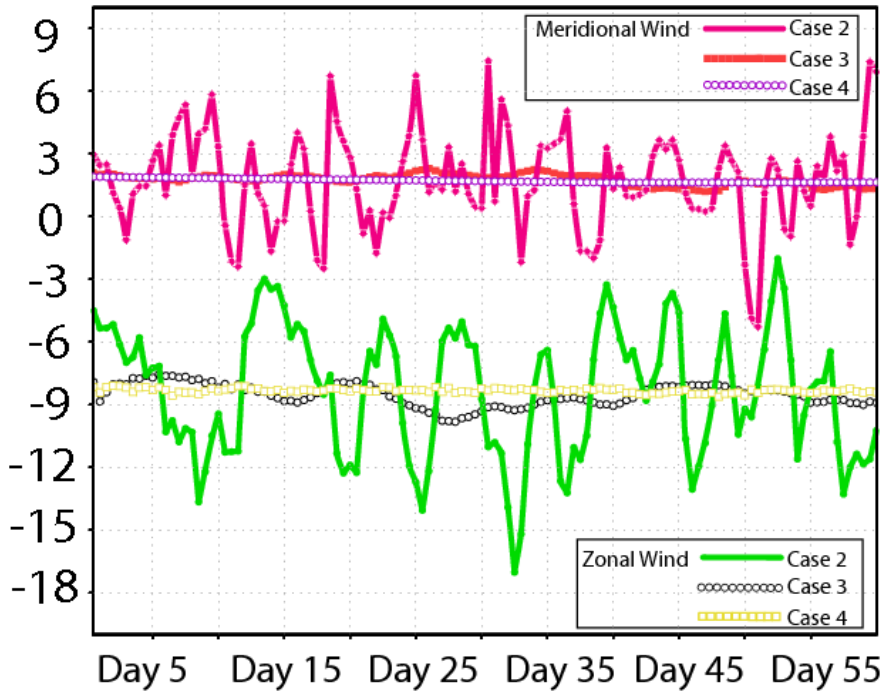

Figure 5.7: Comparison of the temporal evolution of boundary conditions for Cases 2, 3 and 4. The diagram shows examples of meridional wind (units: ms^{-1}), zonal wind (units: ms^{-1}) at 700 hPa at [65°W; 15°N] for each case. The first 60 days of the experiments are presented.

We now address the hypothesis that the mountains in Mexico and Central America produce easterly waves in the eastern Pacific. For this purpose, the topography within the gray rectangle in Figure 5.8 was modified by setting any terrain elevation

greater than 40 m to 40 m, removing, in essence, the influence of the orography. The lateral boundary conditions and SST distribution are identical to the ones used in Case 4.

In the same manner as the control case (Case 1), the model was run for 121 days starting June 1st, 2001.

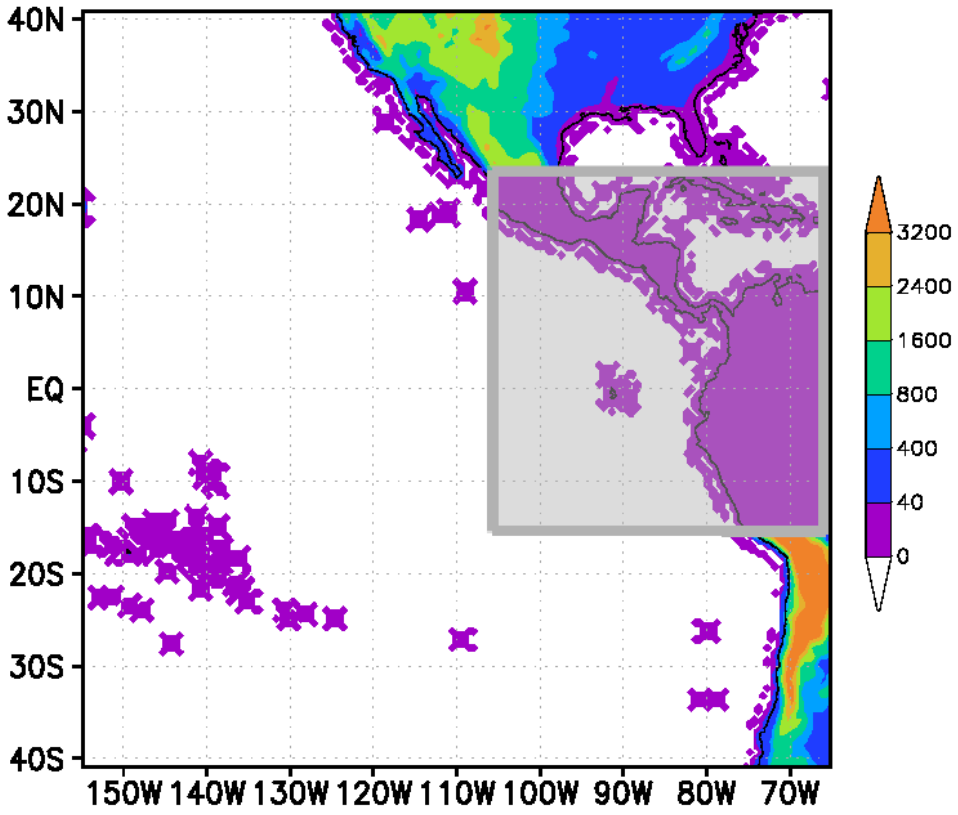

Figure 5.8: Description of topography for Case 5. Terrain elevation was set to 40 m for the region delimited by the gray rectangle.

Figure 5.9 depicts the latitudinal distributions of SST, MSLP and the 925 hPa level absolute vorticity (η) for the 100°W - 85°W longitudinal band for Cases 3 to 5. As noted previously, the SST patterns display different characteristics. Since for Case 3 the SST distribution was kept constant at June 2001 values, the presence of warmer waters south of the equator and relatively colder waters to the north is evident.

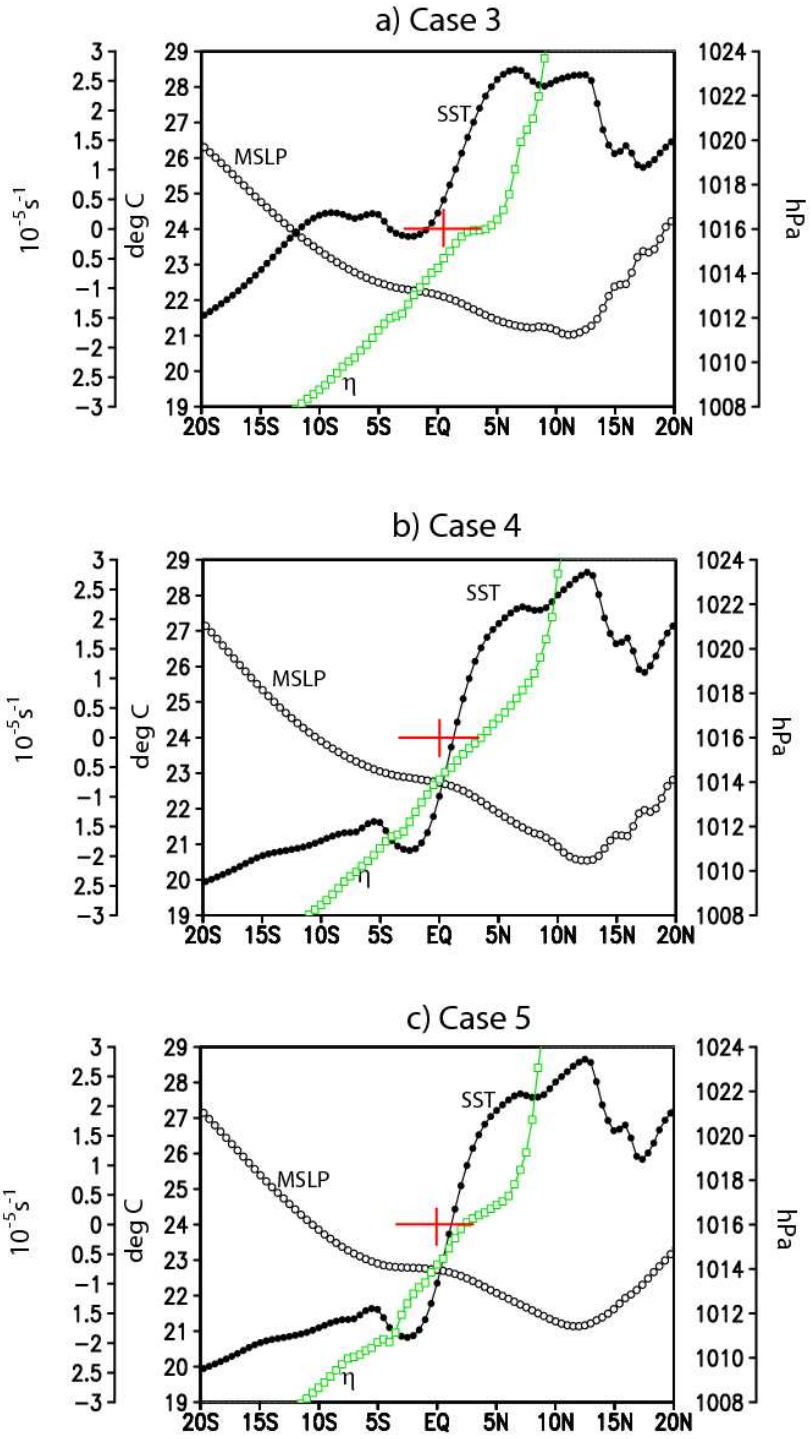

Figure 5.9: Cross-sections of SST (units: °C), MSLP (units: hPa) and absolute vorticity at 925 hPa (units: 10^{-5} s^{-1}) for the 100°W-85°W longitudinal band for Cases 3, 4 and 5. The cross-hairs show location of the equator and zero absolute vorticity.

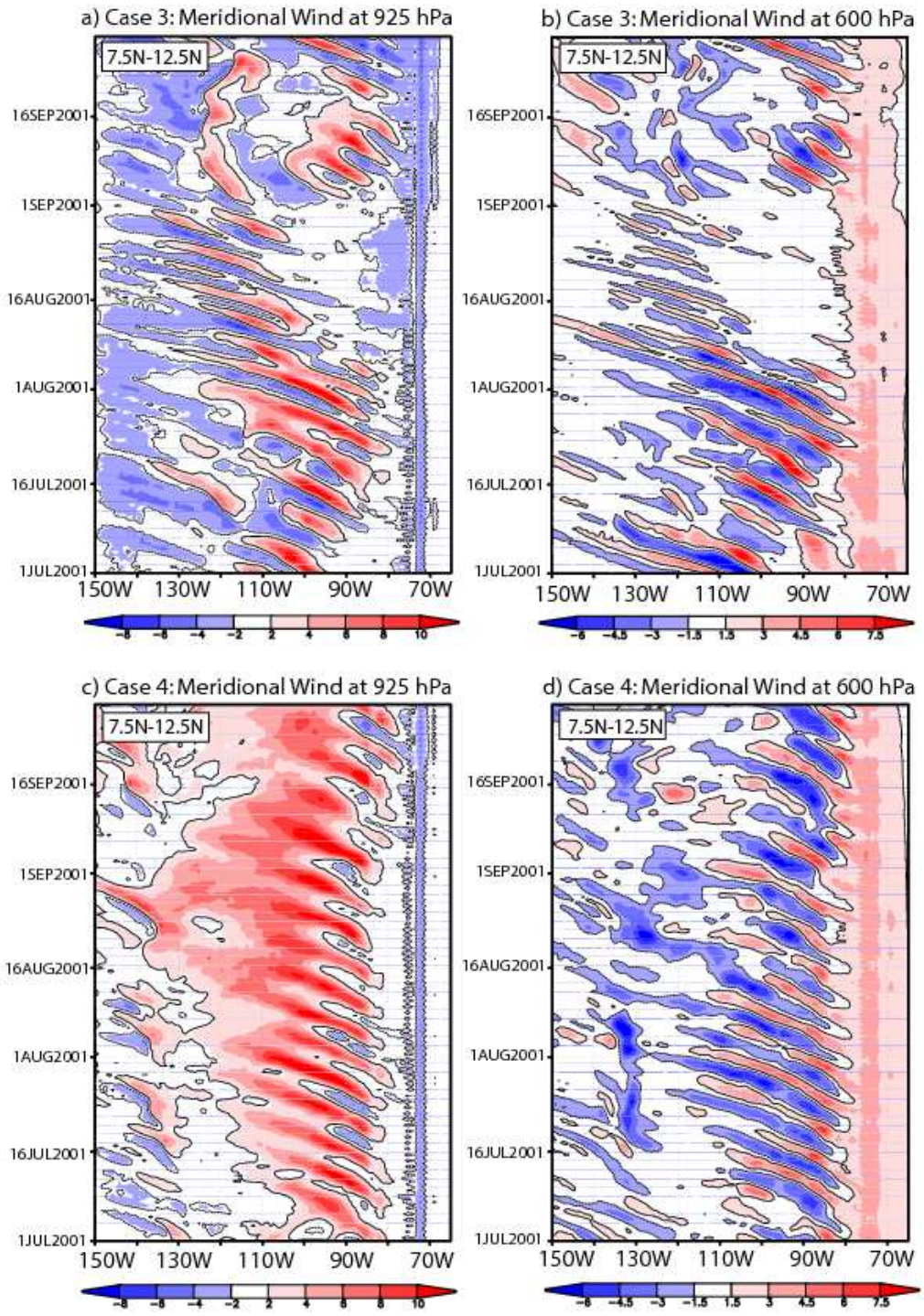

Figure 5.10: Time-longitude diagrams of meridional wind (shading relative to the bar below figure, units: ms^{-1}) at 925 hPa and 600 hPa for days 31 - 121 of Cases 3, 4 and 5, between 150°W and 65°W averaged for the 7.5°N – 12.5°N band. Panels (a) and (b) - Case 3 at 925 hPa and 600 hPa, respectively; panels (c) and (d) - Case 4 at 925 hPa and 600 hPa, respectively; panels (e) and (f) Case 5 at 925 hPa and 600 hPa, respectively.

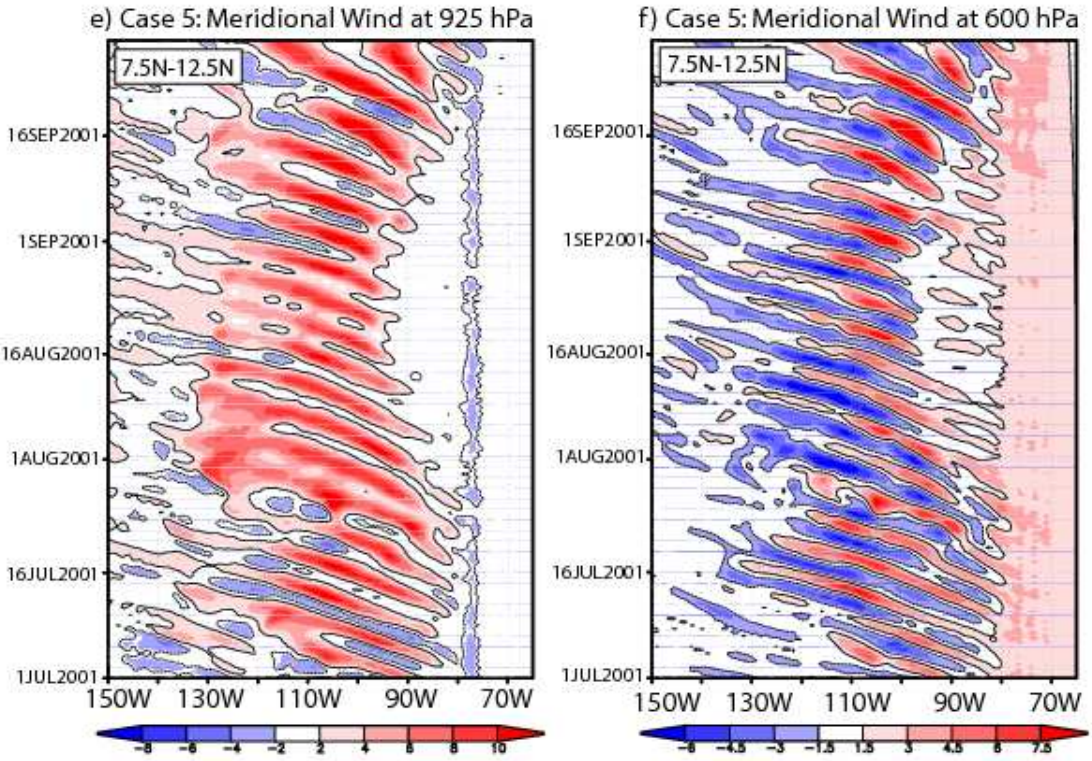

Figure 5.10: (cont)

This leads to a smaller north - south gradient compared to Cases 4 and 5, where SST was obtained as a July-September average. For example, there is a 3.5°C SST difference between 10°N to 10°S in Case 3, versus a 7°C SST difference observed in Cases 4 and 5. Consequently, the 10°S to 10°N MSLP gradient is of 3.5 hPa for Case 3 versus 4.7 hPa difference for Case 4. For Case 5, in which the topography was essentially eliminated, the MSLP gradient of ~ 4 hPa is smaller than in Case 4. As expected, there is a larger northward displacement of $\eta=0$ location in Case 4, versus Cases 3 and 5. The weaker magnitude of southerly wind observed in Case 3 is most likely due the smaller CEPG differences illustrated in Figure 5.9: the larger the magnitude of CEPG, the larger the magnitude of northward wind.

Figure 5.10 shows the time - longitude evolution of unfiltered meridional wind (v) averaged between 7.5°N and 12.5°N at 925 hPa and 600 hPa over the domain for days 31-121, for Cases 3 to 5. The first aspect to be highlighted is the presence of easterly waves in all three instances with small differences from case to case. In addition, for Cases 3 and 5, the disturbance genesis region for period 08/02 to 09/01 appears to be shifted westward compared to the genesis region for period 07/01 to 08/01. The reason for this shift is unclear. Similar characteristics of the easterly weaves were observed in the specific humidity and relative vorticity fields (not shown).

The power spectra of meridional wind (at 850 hPa and 600 hPa levels) at 90°W, 9°N is presented in Figure 5.11. A broad high frequency peak is present in all instances. In agreement with the observations, the same periodicity is present at both 850 hPa and 600 hPa levels.

Figure 5.12 shows the latitude - time evolution of lower tropospheric meridional wind, relatively vorticity and horizontal wind divergence. In all three cases the $\eta = 0$ contour (the thick black line) oscillates between 4°N to 8°N. The meridional wind maximum intersects the $\eta = 0$ line. North of η=0, v oscillates between positive and negative values analogous to the observation presented in Figure 4.11c (Chapter 4). Correspondingly, the relative vorticity and divergence fields oscillate with changes in sign. Cyclonic disturbances form at 8-10°N and propagate northward with time.

It is important to note that, similar to the observations (e.g., Figure 4.11), the convective oscillations appear to have a component on a much larger scale than the 8-15°N area. There is a 3-5 day oscillation period of meridional wind strengthening (weakening) extending from 4°S to 8°N. Moreover, in Case 4 where the CEPG is larger,

a more coherent oscillation of the northward meridional wind is noticed. In addition, the magnitude of both low level convergence (dotted contours) and relative vorticity (shading) is larger in this experiment.

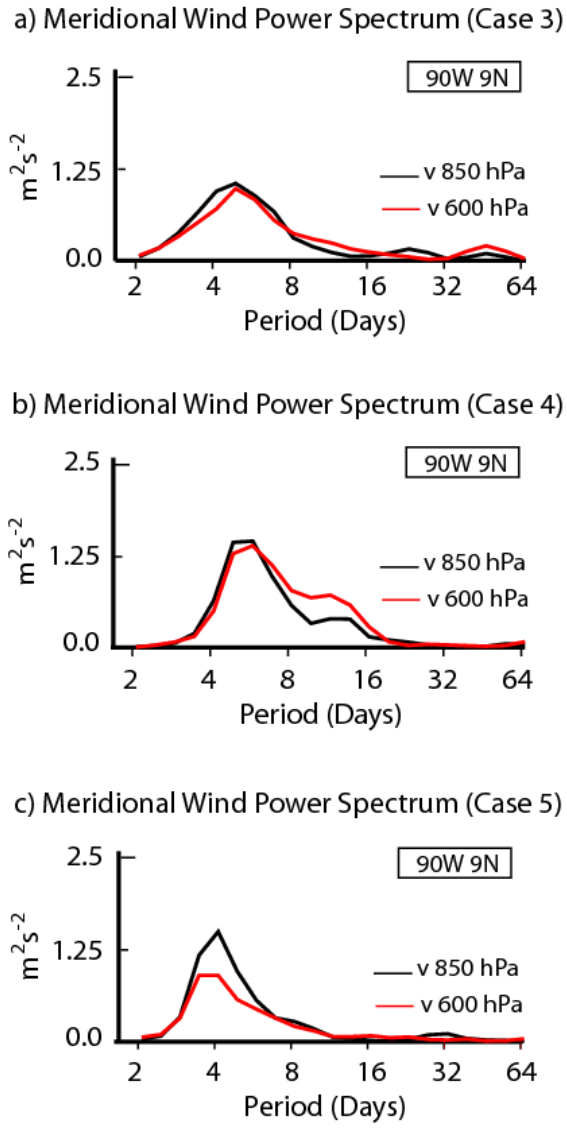

Figure 5.11: Global wavelet power spectra (units: m^2s^{-2}) of meridional wind at two pressure levels: 850 and 600 hPa. Panel (a): Case 3 at [90°W; 9°N], panel (b): Case 4 at [90°W; 9°N] and panel (c) Case 5 at [90°W; 9°N].

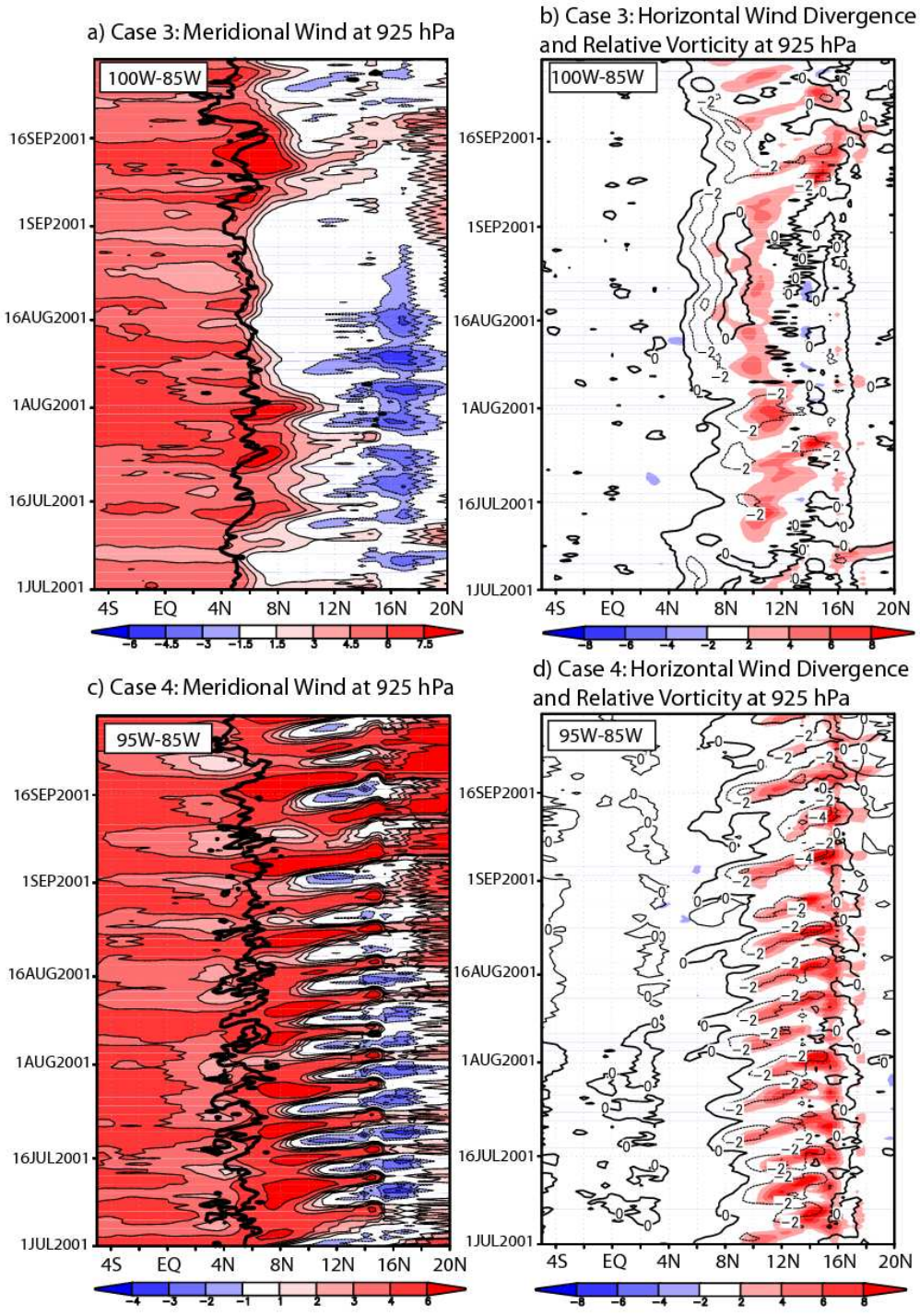

Figure 5.12: a), c), e) Time-latitude diagrams of meridional wind at 925 hPa (shading relative to the bar below, units: ms^{-1}) for Cases 3, 4 and 5, respectively. b), d) and f) horizontal wind divergence at 925 hPa (contour interval $2*10^{-5}s^{-1}$, dotted line: negative values) and relative vorticity at 925 hPa (shading relative to the bar below, units: $10^{-5}s^{-1}$) for Cases 3, 4 and 5, respectively.

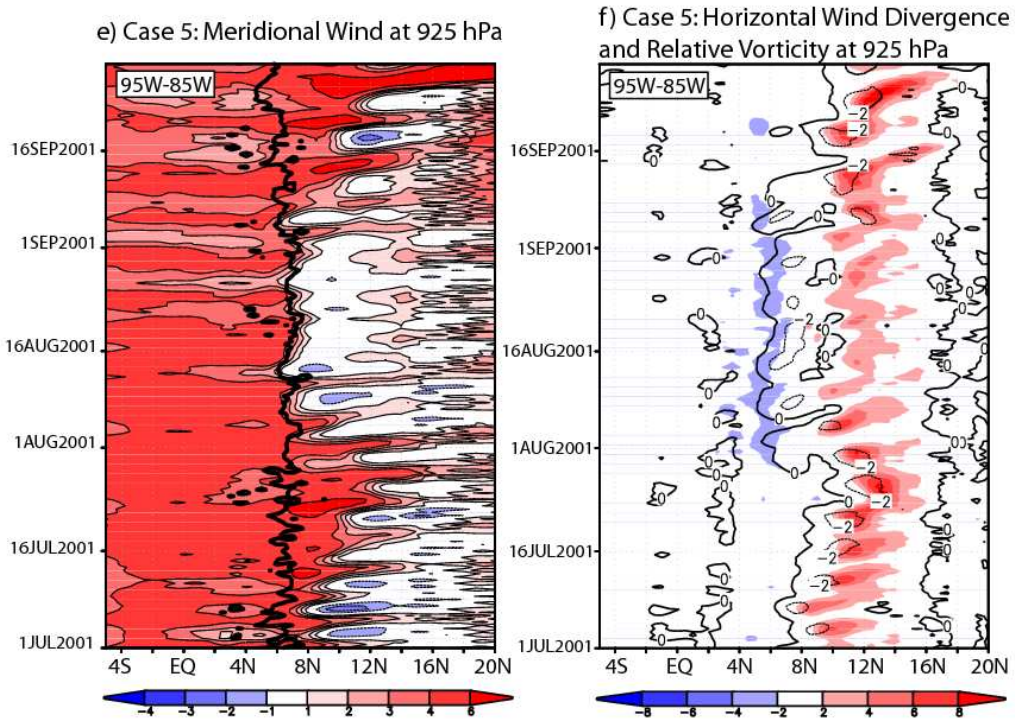

Figure 5.12: cont.

The latitude- height structure of the mean meridional circulation for Cases 3 to 5 is presented in Figure 5.13. The results do not differ significantly from either the observations (Figure 3.3b) or the control cases (Figure 5.4). The typical low level cross-equatorial flow is evident in all three cases. For Case 4, both the upper level and the shallow northerly return flow are stronger than for Cases 3 and 5. In all three instances the η=0 line from surface to about 500 hPa stays north of the equator, rendering an inertialy unstable regime.

To summarize, easterly waves were formed in three separate instances:

(a) When propagating disturbances from the Atlantic Ocean were included in the eastern boundary conditions.

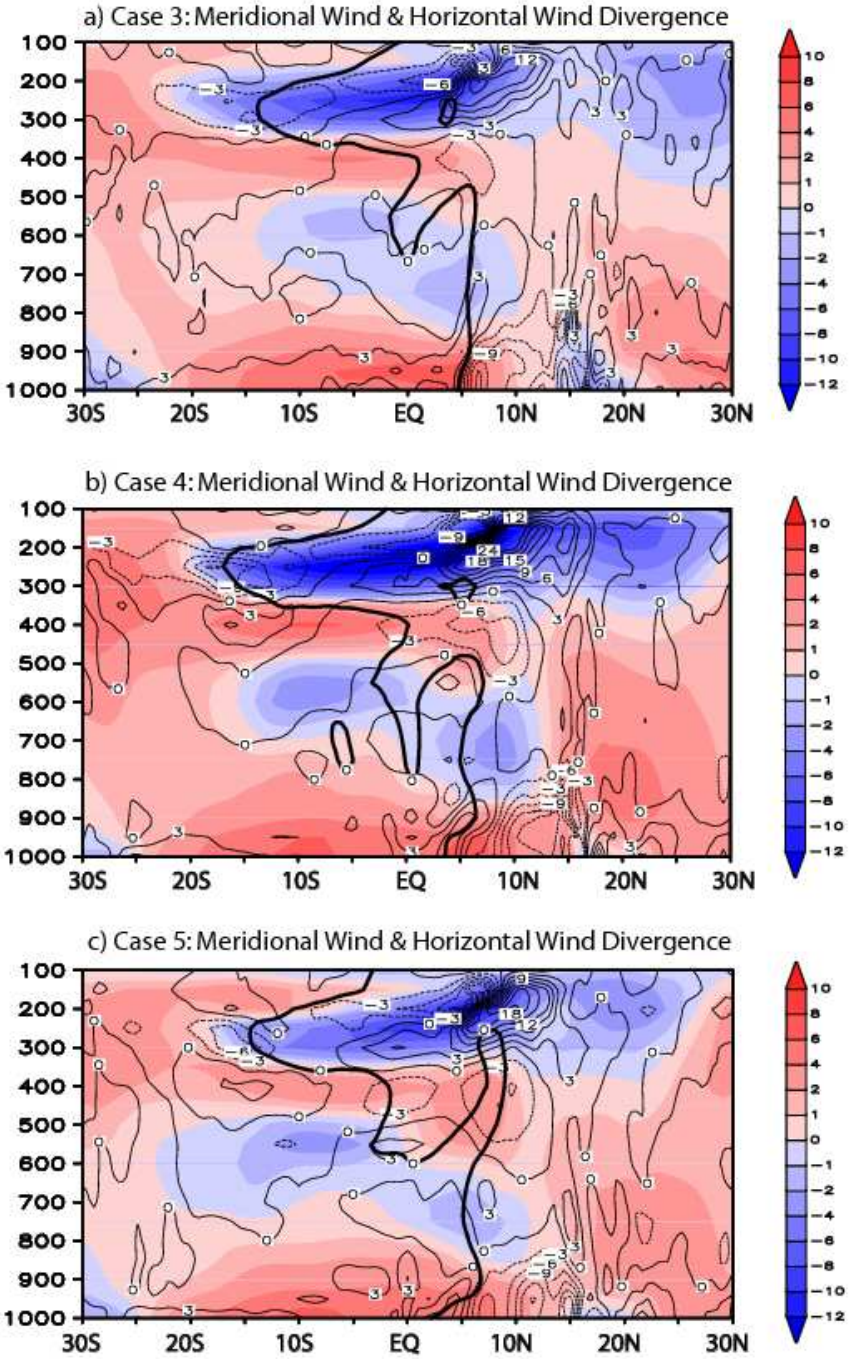

Figure 5.13: Characteristics of the mean (days 31-121) simulated meridional circulation in the eastern Pacific Ocean for Cases 3, 4 and 5. Panel (a) shows the meridional wind (shading relative to the bar on the right, units: ms^{-1}), horizontal wind divergence (contour interval: $3*10^{-6}$ s^{-1}, dotted lines represent negative values), averaged for 100°W-85°W. Panel (b) same as (a) but for Case 4, averaged for 95°W-85°W. Panel (c) same as (a) but for Case 5, averaged for 95°W-85°W. The heavy black line represents the η=0 contour.

(b) When the Atlantic Ocean propagating disturbances were eliminated by running a 10-day filter through the boundary conditions and by using monthly averages as boundary conditions.

(c) When the Central and South America continent orographic influence was eliminated by smoothing the terrain and with smoothed boundary conditions.

The numerical experiments are strongly suggestive that easterly waves form *in situ* in regions of strong CEPG.

CHAPTER VI

CONCLUSION AND CLOSING REMARKS

We have applied a variety of diagnostic methods, numerical modeling techniques and the application of some relatively simple dynamic to study the physical nature of the ITCZ in the eastern Pacific Ocean. The summer and winter average structure of the mean meridional circulation was examined in the ERA-40 reanalysis data set spanning a 20 year time period.

The diagnostic studies reveal a number of interesting results. In regions of strong CEPG, the mean zero absolute vorticity contour (η=0) is displaced northward of the equator. In such regimes, the SST maximum and MSLP minimum are located poleward of the region of strongest convection. This contour bisects a doublet in the divergence field, with divergence on the equatorward side of the contour and convergence on the poleward side. The convergence is collocated with strongest convection. In regions of weak CEPG (e.g., central Pacific Ocean), the MSLP minimum, SST maximum and convection are collocated.

We find that the ITCZ is highly variable with strong westward propagating disturbances with 3-5 day periods. It was noted that the disturbances have the same period as the inertial period at the location of the mean convection. Second, it was noted that there is a maximum of variance in this period range in the region of strong CEPG in the eastern Pacific Ocean. Although it appeared that the waves were generated locally in the region of strong CEPG, the diagnostic study did not rule out the possibility of at least some propagation from the Atlantic Ocean. A composite analysis was undertaken to

examine in detail the horizontal and vertical structure of the transients. One of the major findings was that the transients occupied the same latitudinal domain as the mean meridional circulation. However, in regions of small CEPG, there was not the same latitudinal extent.

We also performed numerical simulations using the WRF mesoscale model to investigate the *in situ* formation of high frequency waves in the East Pacific Ocean.

We now return to the questions posed at the beginning of this study:

(i) Fundamental processes: The basic structures of the mean ITCZ appear determined by the response of the atmosphere to a CEPG and the resultant instabilities associated with the cross-equatorial advection of anticyclonic vorticity. The CEPG is set up by the large scale and slowly varying boundary forcing associated with the SST distribution. The magnitude of the CEPG determines the strength of the divergent wind field and, therefore, the magnitude of the cross-equatorial vorticity advection. In turn, the latitudinal limit of the instability occurs where vortex and divergence terms of the absolute vorticity equation balance. Deep convection occurs in the region of maximum generation of cyclonic vorticity.

The character of the dynamical fields at low latitudes fits well with those expected in an inertially unstable regime (Stevens 1983, TW). However, THW noted that although the system had the appearance of inertial instability, the required basic state would have to be far stronger than observed and the linear stability criterion was not met. To come to this conclusion, THW made an assumption of a stable layer topping the boundary layer that was far stronger than observed in the eastern Pacific. However we argue that the linear stability criterion is indeed met with the use of more realistic values.

(ii) Changes in character of the ITCZ along the equator: The principal reason for the differences in the form of the circulations of the ITCZ and the depth of convection is the magnitude of the CEPG (Figure 1.2c and Table 1.1). In regions of strong CEPG, maximum convection appears equatorward of the SST maxima and MSLP minima. In regions of small or zero CEPG, the convection is collocated with extrema of SST and MSLP (Figure 1.2). In the same figure it can be seen that the OLR is much smaller in the eastern Pacific than in the west indicating much deeper convection. This appears to be a result of the strength of the vortex tube stretching through the generation of the secondary circulation. Thus, convection in the eastern Pacific has an extra forcing factor than in the central Pacific where convection occurs principally by propagation from the east (e.g., Figure 4.2).

The increase of the intensity of convection in a strong CEPG is corroborated by Lindzen and Hou (1988). The study found that when the location of imposed heating in a zonally symmetric model was moved from the equator to an off-equator location, the circulation became more vigorous in magnitude even if the magnitude of the heating function was not changed. Lindzen and Hou offered no explanation for the increase in magnitude except to say that it matched observations. Furthermore, there is no reference to a CEPG that would have been consistent with the off-equator location of the ITCZ. However, close examination of the circulation patterns produced by Lindzen and Hou indicates that when the heating was placed off the equator, the $\eta = 0$ contour was also located away from the equator. Thus, the Lindzen and Hou may represent an unstable regime and the increase of response may be due to the stabilizing generation of cyclonic vorticity.

(iii) Transients and the ITCZ: As the CEPG remains almost constant in magnitude throughout the summer, there is a constant flux of anticyclonic vorticity across the equator. Against this background CEPG, the system undergoes a series of build-ups of the unstable state and relaxations when sufficient cyclonic vorticity has been generated to offset the advection of anticyclonic vorticity across the equator. The relaxation of the instability occurs with the generation of deep convection at a latitude determined by magnitude of the CEPG (Equation 4.6 and Figure 4.9) where the advection is balanced by the vortex stretching term. The vertically integrated heating in the ITCZ region oscillates between 6 K/day and 12 K/day at the inertial frequency of the location of convection. This latitude is important, as the inertial frequency of this latitude will determine the frequency of the latent heating oscillation. This "inertial oscillator" is the result of a state of continued instability sustained by a slowly varying CEPG. Figure 3.11 shows that the inertial frequency for 4°N is 8 days and for 8°N it is 4 days.

There are other similar geophysical examples of perpetual instability. During a day of strong insolation, the near-surface layer over land is super-adiabatic and therefore convectively unstable. The column adjusts to a neutral adiabatic profile by the shedding turbulent eddies and subsequent vertical mixing. Yet, the destabilization is only temporary as the radiational heating is constant and at the surface eddies are continuously produced. During the winter, baroclinic disturbances develop on the unstable temperature gradient between the equator and the pole forced by the radiational heating gradient. The disturbances render the system regionally stable by latitudinal mixing but as the temperature gradient rebuilds under the action of the radiational heating gradient, the system becomes unstable and new baroclinic waves develop.

(iv) The shallow meridional circulation: The shallow circulation, apparent in Figure 3.3b, comes about as a statistical artifact of the averaging through the transitions that are documented in Figure 4.4. The shallow circulation develops on Day -2 to Day -1 before growing in magnitude and extending vertically. The ZMB circulation, as seen in Figure 3.3, is representative of the growth of the stabilizing secondary circulation.

(v) In situ formation of easterly waves: Perhaps the most basic question is whether easterly waves are the result of a local instability mechanism as described above and, thus, developing *in situ* in regions of strong CEPG, or the result of waves generated elsewhere and propagating through the eastern Pacific. To test the hypothesis that at least a large percentage of waves develop *in situ,* we have presented the results of several numerical experiments. The initial and boundary conditions we set both to include westward propagating disturbances from the Atlantic Ocean, in the first instance, and then with them eliminated in the second instance. Both results, with and without disturbances at the eastern boundary, show *in situ* formation of waves in the region of strong CEPG of the eastern equatorial Pacific Ocean. An additional experiment shows that the mountains of Central America and Mexico also appear not necessary for the formation of waves in the eastern Pacific Ocean.

There is a further question that requires discussion. TW noted that there were a number of other regions where the CEPG was appreciable such as the eastern Atlantic Ocean, the northern Indian Ocean in the northern summer and the southern Indian Ocean during the southern summer. In these regions there were ITCZ structures similar to the eastern Pacific Ocean. Are these regions also source regions of waves resulting from inertial instability? Of particular interest is the eastern Atlantic Ocean where, for many

years, the Burpee (1971) instability theory has been the accepted theory for the generation of easterly waves. Is an inertial oscillator in the eastern Atlantic also an important source of wave activity?

REFERENCES

Adler, R.F., G.J. Huffman, A. Chang, R. Ferraro, P. Xie, J. Janowiak, B. Rudolf, U. Schneider, S. Curtis, D. Bolvin, A. Gruber, J. Susskind, P. Arkin, 2003: The Version 2 Global Precipitation Climatology Project (GPCP) Monthly Precipitation Analysis (1979-Present). *J. Hydrometeor*., 4, 1147-1167.

Avila, L.A., and G.B. Clark, 1989: Atlantic Tropical Systems of 1988. *Mon. Wea. Rev*., 117, 2260–2265.

Avila, L. A., and R. J. Pasch, 1992: Atlantic tropical systems of 1991: *Mon.Wea. Rev*., 120, 2688–2696.

Barlow, M., and D. Salstein 2006: Summertime influence of the Madden-Julian Oscillation on daily rainfall over Mexico and Central America, *Geophys. Res. Lett.*, 33 (21).

Bates J. R., 1970: Dynamics of disturbances on the Intertropical convergence Zone. *Quart. J. Roy. Meteor. Soc.*, 96, 677–701.

Bates, J. J., X. Wu, and D. L. Jackson, 1996: Interannual variability of upper troposphere water vapor band brightness temperature. *J. Clim.*, 9, 427–438.

Betts, A. K. and M. J. Miller,1993: The Betts–Miller scheme. The Representation of Cumulus Convection in Numerical Models*, Meteor. Monogr.,* No. 46, Amer. Meteor. Soc., 107–121.

Biasutti, M., D. S. Battisti and E. S. Sarachik, 2003: The annual cycle over the tropical Atlantic, South America, and Africa. *J. Clim.*, 16(15): 2491-2508.

Bjerknes, J. 1969: Atmospheric teleconnections from the equatorial Pacific. *Mon. Wea. Rev.*, 97, 163-172.

Burpee, R. W., 1972: The origin and structure of easterly waves in the lower troposphere of North America. *J. Atmos. Sci.*, 29, 77–90.

Chang, C. P., 1970: Westward propagating cloud patterns in the tropical Pacific as seen from time-composite satellite photos. *J. Atmos. Sci.,* 27, 133-138.

Chang C. P., 1973: A dynamical model of the intertropical convergence zone. *J. Atmos. Sci*., 30, 190–212.

Charney, J. G., 1971: Tropical cyclogenesis and the formation of the intertropical convergence zone. *Mathematical Problems of Geophysical Fluid Dynamics,* W. H. Reid, Ed., *Lectures in Applied Mathematics,* Vol. 13, Amer. Math. Soc., 355–368.

Curry, J. A. and Webster, P. J, 1999: Thermodynamics of Atmospheres and Oceans, *Academic Press*.

deSzoeke SP, Bretherton CS, Bond NA, Cronin MF,Morley BM, 2005: EPIC 95°W Observations of the Eastern Pacific Atmospheric Boundary Layer from the Cold Tongue to the ITCZ. J. *Atmos. Sci.* 62(2): 426.

Duchon, C. E., 1979: "Lanczos filtering in one and two dimensions," *J. Applied Meteor*. 18, 1016-1022.

Dudia, J., 1989: Numerical study of convection observed during the winter monsoon experiment using a mesoscale two-dimensional model. *J. Atmos. Sci*., 46, 3077-3107.

Farfan, L. M., and J. A. Zehnder, 1997: Orographic influence on the synoptic-scale circulations associated with the genesis of Hurricane Guillermo (1991). *Mon. Wea. Rev.,* **125,** 2683–2698.

Frank, N. L., 1970: Atlantic tropical systems of 1969. *Mon. Wea. Rev.*, 98, 307–314.Grist, J. P**.**, and S. E. Nicholson, 2001: A study of the dynamic factors influencing the rainfall variability in the West African Sahel. *J. Clim.,* 14, 1337-1359.

Grist J. P., and S. E. Nicholson, 2001: A study of the dynamic factors influencing the interannual variability of rainfall in the West African Sahel. *J. Clim.*, 14, 1337–1359.

Hack, J. J., W. H. Schubert, D. E. Stevens, and H. Kuo, 1989: Response of the Hadley circulation to convective forcing in the ITCZ. *J. Atmos. Sci.,* 46, 2957–2973.

Hadley G., 1735: Concerning the cause of the general trade-winds. *Phil. Trans.*, 29, 58–62.

Halley, Edmond, An Historical Account of the Trade Winds, and Monsoons, Observable in the Seas Between and Near the Tropicks; With an Attempt to Assign the Phisical Cause of Said Winds, *Philosophical Transactions, Vol* 183, 1686 p. 153-168.

Hartmann, D. L., 1994: Global Physical Climatology, *Academic Press*.

Hastenrath, S. and P.J. Lamb, 1977a: Climate Atlas of the tropical Atlantic and eastern Pacific oceans. *University of Wisconsin Press*, 112 pp.

Hastenrath, S. and P.J. Lamb, 1977b: Some aspects of circulation and climate over the eastern Atlantic. *Mon. Wea. Rev.,* 106, 1280-1287.

Held, I. M., and Hou, A. Y., 1980: Nonlinear axially symmetric circulations in a nearly inviscid atmosphere. *J. Atmos. Sci.* **37**, 515-533.

Hess, P.G., D.S. Battisti and P. Rasch, 1993: "Maintenance of the Intertropical Convergence Zones and the Large-Scale Tropical Circulation on a Water Covered Earth." *J. Atmos. Sci*., **50**, 691-713.

Holton, J. R., J. M. Wallace, and J. A. Young, 1971: On boundary layer dynamics and the ITCZ. *J. Atmos. Sci.*, 28, 275–180.

Hoyos, C. and P. J. Webster, 2007: The role of intraseasonal oscillation on the nature of monsoon precipitation. *J. Clim.*, 20 (17), 4402-4424.

Hong, S-.Y., J. Dudhia, S.-H. Chen, 2004: A revised approach to ice-microphysical processes for the bulk parameterization of cloud and precipitation., *Mon. Wea. Rev*., 132, 103-120.

Hou, A.Y. and R.S. Lindzen, 1992: The influence of concentrated heating on the Hadley circulation. *J. Atmos. Sci.*, 49, 1233-1241.

Janjic, Z. I., 1994: The step-mountain Eta coordinate model: Further developments of the convection, viscous sublayer, and turbulence closure schemes. *Mon. Wea. Rev*., 122, 927–945.

Kain, J. S., and J. M. Fritsch, 1993: Convective parameterization for mesoscale models: The Kain-Fritcsh scheme. The representation of cumulus convection in numerical models, K. A. Emanuel and D.J. Raymond, Eds., *Amer. Meteor. Soc*., 246.

Knox, J.A., 2002: Inertial Instability, *Encyclopedia of Atmospheric Sciences*, 1004-1012.

Laprise, R., 1992: The Euler equations of motion with hydrostatic pressure as an independent variable. *Mon. Wea. Rev*., 120, 197–207.

Lawrence, D, and P. J. Webster, 2001: Interannual variability of intraseasonal convection and the Asian monsoon. *J. Clim*., 14(3), 2910-2922.

Liebmann B. and C.A. Smith, 1996: Description of a Complete (Interpolated) Outgoing Longwave Radiation Dataset. *Bull. Amer. Met. Soc.*, 77, 1275-1277.

Lindzen, R. S., and Hou A. Y., 1988: Hadley circulations for zonally averaged heating centered off the equator. *J. Atmos. Sci.* 45, 2416-2427.

Lindzen, R. S., and Nigam, S 1987: On the role of sea surface temperature gradients in forcing low level winds and convergence in the tropics. *J. Atmos. Sci.*, 44, 2418-2436.

Madden, R. A., and P. R. Julian, 1971: Detection of a 40–50 day oscillation in the zonal wind in the tropical Pacific. *J. Atmos. Sci.,* 28**,** 702–708.

Mak, M. K., 1969: Laterally driven stochastic motions in the tropics. *J. Atmos. Sci.*, 26, 41–64.

Maloney, E. D. and D. L. Hartmann, 2000: Modulation of Eastern North Pacific Hurricanes by the Madden-Julian Oscillation. *J. Clim.*, 13, 1451-1460.

Manabe S., 1969: Climate and the ocean circulation. 1. The atmospheric circulation and the hydrology of the earth's surface. *Mon. Wea. Rev*., 97, 739–774.

Manabe, S., Hahn, D. G. and Holloway, Jr., J. L. 1974. The seasonal variation of the tropical circulation assimulated by a global model of the atmosphere. *J.Atmos. Sci*. 31, 43-83.

McPhaden, M J., A. J. Busalacchi, R. Cheney, J-R. Donguy, K. S. Gage, D. Halpern, M. Ji, P. Julian, G. Meyers, G. Mitchum, P. P. Niiler, J. Picaut, R. W. Reynolds, N. Smith, et K. Takeuchi. The Tropical Ocean Global Atmosphere (TOGA) observing system: A decade of progress. J. Geophys. Res., 103, 14169-14240.

Mitchell, T. P. and J. M. Wallace, 1992: The annual cycle in equatorial convection and sea surface temperature. *J. Clim.*, **5**, 1140-115.

Mlawer EJ, Taubman SJ, Brown PD, Iacono MJ, Clough SA, 1997: Radiative transfer for inhomogeneous atmospheres: RRTM, a validated correlated-k model for the longwave. *J. Geophys. Res*;102:16,663–82.

Molinari, J., D. Knight, M. J. Dickinson, D. Vollaro, and S. Skubis, 1997: Potential vorticity, easterly waves, and eastern Pacific tropical cyclogenesys. *Mon. Wea. Rev*., 125, 2699-2708.

Nitta, T., Y. Nakagomi, Y. Suzuki, N. Hasegawa, and A. Kadokura, 1985: Global analysis of the lower-tropospheric disturbances in the tropics during the northern summer of the FGGE year. Part I: Global features of the disturbances. *J. Met. Soc. Japan,* 63**,** 1–19.

Oort A. H., and J. J. Yienger, 1996: Observed interannual variability in the Hadley circulation and its connection to ENSO. *J. Clim.*, 9, 2751–2767.

Noh, Y., W. G. Cheon, and S. Y. Hong, 2003: Improvement of the K-profile model for the planetary boundary layer based on large eddy simulation data. *Bound.-Layer Met.*, 107, 401-427.

Numaguti, A., 1993: Dynamics and Energy Balance of the Hadley Circulation and the Tropical Precipitation Zones: Significance of the Distribution of Evaporation. *J Atmos. Sci***.,** 50**,** 1874-1887.

Palmer, C.E., 1951: Tropical Meteorology. *Compendium of Met.*, *Amer. Met. Soc*., 859-880.

Palmer, C. E., 1952: Tropical meteorology. *Quart. J. Roy. Met. Soc*., 78, 126–164.

Philander, S. G. H., D. Gu, D. Halpern, G. Lambert, N.-C. Lau, T. Li, and R. C. Pacanowski, 1996: The role of low-level stratus clouds in keeping the ITCZ mostly north of the equator. *J. Clim.,* **9,** 2958–2972.

Pike, A.C., 1971: Intertropical convergence zone studied with an interacting atmosphere and ocean model. *Mon. Wea. Rev*., 99, 469-477.

Press, W. H., B. P. Flannery, S. A. Teukolsky, and W. T. Vetterling, 1989: Numerical Recipes in Pascal. *Cambridge University Press*.

Ramage, CS, 1974: Structure of an oceanic near-equatorial trough deduced from research aircraft traverses. *Mon. Wea. Rev.,* 102, 754–759.

Raymond, D. J., C. Lopez-Carrillo, and L. Lopez Cavazos, 1998: Case-studies of developing east Pacific easterly waves. *Quart. J. Roy. Met. Soc*., 124, 2005-2034.

Raymond, D. J., Esbensen, S. K., Paulson, C., Gregg, M., Bretherton, C. S., Petersen, W. A., Cifelli, R., Shay, L. K., Ohlmann, C., Zuidema, P., 2004, EPIC2001 and the coupled ocean-atmosphere system of the tropical east Pacific. *Bull. Amer. Met. Soc*., 85(9), 1341-1354.

Raymond, D. J., C. S. Bretherton, and J. Molinari, 2006: Dynamics of the intertropical convergence zone of the East Pacific. *J. Atmos. Sci*., 63, 582-597.

Rayner, N.A., D.E. Parker, E.B. Horton, C.K. Folland, L.V. Alexander, D.P. Rowell, E.C. Kent, and A. Kaplan, Global analysis of sea surface temperature, sea ice, and night marine air temperature since the late nineteenth century, *J. Geophys. Res*., 108.

Reynolds, R. W., Rayner, N. A., Smith, T. M., Stokes, D. C., Wang, W. Q., 2002: An improved in situ and satellite SST analysis for climate. *J. Clim.,* 15, 1609-1625.

Riehl, H., 1945: Waves in the easterlies and the polar front in the tropics. Misc. Rept. No. 17, *Dept. of Met., University of Chicago*.

Riehl, H., and J. S. Malkus, 1958: On the heat balance in the equatorial trough zone. *Geophysica,* ***6*****,** 503–537.

Riehl, and J. (Malkus) Simpson, 1979: The heat balance in the equatorial trough zone, revisited. *Contrib. Atmos. Phys.,* 52**,** 287– 305.

Rowntree, P.R. 1971: The influence of tropical east Pacific Ocean temperatures on the atmosphere. *Quart. J. Roy. Met. Soc.,* 421- 575.

Sadler, JC, 1975: The monsoon circulation and cloudiness over the GATE area. *Mon. Wea. Rev.,* 103, 369–387.

Sanson Sansom, HW, 1965: The structure and behavior of the ITCZ. *The World Meteorological Organization* Technical Note, No. 69, Geneva, 91-108

Schubert W. H., P. E., Ciesielski, D. E. Stevens, and H. C. Kuo, 1991: Potential vorticity modeling of the ITCZ and the Hadley circulation. *J. Atmos. Sci***.,** 48**,** 1493–1509.

Serra, Y.L. and R.A. Houze, Jr., 2002: Observations of Variability on Synoptic Time scales in the East Pacific ITCZ. *J. Atmos. Sci.*, 59, 1723-1743.

Serra, Y. L., G. N. Kiladis, and M. F. Cronin. Horizontal and vertical structure of easterly waves in the Pacific ITCZ. *J. Atmos. Sci.*, 65, 1266-1284, 2008.

Shapiro, L. J., 1986: The three-dimensional structure of synoptic-scale disturbances over the tropical Atlantic. *Mon. Wea. Rev.,* 114, 1876–1891.

Smith, T.M., R.W. Reynolds, T. C. Peterson, and J. Lawrimore 2007: Improvements to NOAA's Historical Merged Land-Ocean Surface Temperature Analysis (1880-2006). In press. *J. Clim.*

Soden, B. J., and R. Fu, 1995: A satellite analysis of deep convection, upper-tropospheric humidity, and the greenhouse effect. *J. Clim.,* 8, 2333-2351.

Stevens, D., 1983: On symmetric stability and instability of zonal mean flows near the equator. *J. Atmos. Sci.*, 40, 882–893.

Takahashi, K, and D. S. Battisti, 2007: Processes Controlling the Mean Tropical Pacific Precipitation Pattern. Part I: The Andes and the Eastern Pacific ITCZ, *J. Climate* 20, 23, 5696-5706.

Thorncroft, C. D. and B. J. Hoskins, 1994: An idealized study of African easterly waves. I: A linear view. *Quart. J. Roy. Met. Soc*., 120, 953.

Thorncroft, C. D. and B. J. Hoskins, 1994: An idealized study of African easterly waves. II: A nonlinear view. *Quart. J. Roy. Met. Soc*., 120, 985.

Tian, B., and V. Ramanathan, 2002: Role of Tropical Clouds in Surface and Atmospheric Energy Budget*., J. Clim*., **15**, 296–305.

Tomas, R. and P. J. Webster, 1997: On the location of the Intertropical Convergence zone and near-equatorial convection: The role of inertial instability. *Quar. J. Roy. Met. Soc*., 123, 1445-1482.

Tomas, R. A., J. R. Holton, and P. J. Webster, 1999: The influence of cross-equatorial pressure gradients on the location of near-equatorial convection. *Quart. J. Roy. Met. Soc.,* 125, 1107-1127.

Torrence, C. and G. P. Compo, 1998: A practical guide to wavelet analysis. *Bull. Amer. Met. Soc.*, 79 (1), 61-78.

Trenberth, K.E., 1976: Spatial and temporal variations of the Southern Oscillation. *Quart. J. Roy. Met. Soc*., **102**, 639-653.

Trenberth, K.E. 1997: The definition of El Niño. *Bull. Amer. Met. Soc*., 78, 2771–2777.

Trenberth, K.E., and J.M. Caron, 2001: Estimates of Meridional Atmosphere and Ocean Heat Transports. *J. Clim.*, 14, 3433–3443.

Uppala, S. M., P.W. Kållberg, A.J. Simmons, U. Andrae, V. da Costa Bechtold, M. Fiorino, J.K Gibson, J. Haseler, A. Hernandez, G.A. Kelly, and 35 coauthors: 2005: The ERA-40 reanalysis. *Quart. J. Roy. Met. Soc.*, 131, 2961-3012.

Vincent, D., 1994: The South Pacific convergence zone (SPCZ): A review. *Mon. Wea. Rev.*, 122, 1949-1970.

Waliser, D. E., and R. C. J. Somerville, 1994: Preferred latitudes of the Intertropical Convergence Zone. *J. Atmos. Sci.*, 51, 1619-1639.

Wallace J. M. and C. P Chang, 1969: Spectrum analysis of large-scale wave disturbances in the tropical lower troposphere. *J. Atmos. Sci.* 26,1010-1025.

Webster, P. J., and R. Lukas, 1992: TOGA-COARE: The Coupled Ocean-Atmosphere Response Experiment. *Bull. Amer. Met. Soc.*, 73, 1377-1416.

Webster, P. J., T. Palmer, M. Yanai, R. Tomas, V. Magana, J. Shukla and A. Yasunari, 1998: Monsoons: Processes, Predictability and the prospects for prediction. *J. Geophys. Res*., 103 (TOGA special issue), 14451-14510.

Wicker, L. J., and W. C. Skamarock, 2002: Time split-ting methods for elastic models using forward time schemes. *Mon. Wea. Rev*., 130, 2088-2097.

Yanai, M. T. Maruyama, T. Nitta,Y. Hayashi, 1968: Power spectra of large scale disturbances over the tropical pacific. *J. Met. Soc. Japan*, 46, 308-323.

Zehnder, J. A, and R. L. Gall, 1991: Alternative mechanisms of tropical cyclone formation in the Eastern North Pacific. *Atmosfera*, 4, 37-51.

Zhang, C., M. McGauley and N.A. Bond, 2004: Shallow meridional circulation in the tropical eastern Pacific *J. Clim.*, 17, 133-139.

Zhang, C., D. S. Nolan, C. D. Thorncroft, and Nguyen, H., 2008: Shallow meridional circulations in the tropical atmosphere. *J. Clim.*, in press.

Zipser, E. J., 2003: Some views On "Hot Towers" after 50 years of tropical field programs and two years of TRMM data. *Meteorological Monographs*: Vol. **29**, No. 51, 49-58.

Xie, S.-P. and S.G.H. Philander, 1994: A coupled ocean-atmosphere model of relevance to the ITCZ in the eastern Pacific. *Tellus*, 46A, 340-350.

Yuter, S. E., and R. A. Houze, Jr., 2000: The 1997 Pan American Climate Studies Tropical Eastern Pacific Process Study. Part I: ITCZ region. *Bull. Amer. Meteor. Soc*., 81, 451-481.

Yuter, S. E., Y. L. Serra, and R. A. Houze, Jr., 2000: The 1997 Pan American Climate Studies Tropical Eastern Pacific Process Study. Part II: Stratocumulus region. *Bull. Amer. Meteor. Soc*., 81, 483-490.